UNIVERSITY OF CALIFORNIA, SAN DIEGO

Reducing Uncertainty in Estimates of Environmental Parameters From Ambient Noise Using Statistical Array Processing

A dissertation submitted in partial satisfaction of the
requirements for the degree
Doctor of Philosophy

in

Electrical Engineering
(Applied Ocean Sciences)

by

Ravishankar Menon

Committee in charge:

Professor William S. Hodgkiss, Chair
Professor Peter Gerstoft, Co-Chair
Professor Michael Buckingham
Professor William Coles
Professor Nuno Vasconcelos

2013

The dissertation of Ravishankar Menon is approved, and it is acceptable in quality and form for publication on microfilm and electronically:

_____

_____

_____

_____
Co-Chair

_____
Chair

University of California, San Diego

2013

DEDICATION

To family, friends, and pets...

TABLE OF CONTENTS

LIST OF FIGURES

LIST OF TABLES

ACKNOWLEDGEMENTS

I would like to thank my advisors Peter Gerstoft and Bill Hodgkiss for their constant support and guidance over the past five years. Both of them, in their unique ways, have helped me tremendously in honing my skills and steering me in my journey towards being an independent researcher.

I would also like to thank my committee members for their time and valuable comments, and the professors at SIO, especially Bill Kuperman, Mike Buckingham, Glenn Ierley, and Clint Winant, with whom I've had many good discussions and have learnt a great deal. Thanks also go to the staff at MPL — (late) Evelyn Doudera, Diana Stockdale, Irina Tsimring, Anne Footer, BethAnn Clausen and folks at the Point Loma office — who have been very helpful and efficient with the administrative side of things, to the point of making it nearly invisible to me.

I would also like to express my gratitude to Prof. Iain Johnstone at Stanford, who despite being ambushed by me at a parking lot in UC Berkeley, graciously took the time to discuss my research problems. His help and encouragement came at a crucial period during my research and helped clear some conceptual road blocks.

Finally, I would also like to thank my friends and office mates for all the support and good times over the years, and my family and girlfriend Paula for their love and support.

This work was supported by a Graduate Traineeship Award from the Office of Naval Research.

Chapter 2, in full, is a reprint of the material that is in preparation for submission to the Journal of Geophysical Research. The dissertation author was the primary researcher and author of this paper.

Chapter 3, in full, is a reprint of the material as it appears in R. Menon, P. Gerstoft and W. S. Hodgkiss, "Asymptotic Eigenvalue Density of Noise Covariance Matrices", IEEE Trans. Signal Proc., **60**, 3415-3424 (2012) . The dissertation author was the primary researcher and author of this paper.

Chapter 4, in full, is a reprint of the material as it appears in R. Menon, P. Gerstoft and W. S. Hodgkiss, "Effect of Medium Attenuation on the Asymptotic Eigen-

values of Noise Covariance Matrices", IEEE Signal Proc. Lett., **20**, 435-438 (2013). The dissertation author was the primary researcher and author of this paper.

Chapter 5, in full, is a reprint of the material as it appears in P. Gerstoft, R. Menon, W. S. Hodgkiss and C. F. Meckelenbräuker, "Eigenvalues of the sample covariance matrix for a towed array", J. Acoust. Soc. Am., **132** (4), 2388-2396 (2012). This paper is based on Chapter 3 and the dissertation author contributed significantly to the research and material that forms the basis of this chapter.

Chapter 6, in full, is a reprint of the material as it appears in R. Menon, P. Gerstoft and W. S. Hodgkiss, "Cross-correlations of diffuse noise in an ocean environment using eigenvalue based statistical inference", J. Acoust. Soc. Am. **132** (5), 3213-3224 (2012). The dissertation author was the primary researcher and author of this paper.

VITA

2008	B. Tech. and M. Tech. in Naval Architecture and Ocean Engineering, Indian Institute of Technology Madras
2010	M. S. in Oceanography (Applied Ocean Sciences), University of California San Diego
2013	Ph. D. in Electrical Engineering (Applied Ocean Sciences), University of California San Diego

PUBLICATIONS

R. Menon, P. Gerstoft and W. S. Hodgkiss, "Asymptotic Eigenvalue Density of Noise Covariance Matrices", *IEEE Trans. Signal Proc.*, **60**, pp. 3415–3424, 2012.

P. Gerstoft, R. Menon, W. S. Hodgkiss and C. F. Meckelenbräuker, "Eigenvalues of the sample covariance matrix for a towed array", *J. Acoust. Soc. Am.*, **132** (4), pp. 2388–2396, 2012.

R. Menon, P. Gerstoft, and W. S. Hodgkiss, "Passive acousting monitoring using random matrix theory," *IEEE Stat. Signal Proc. Workshop (Ann Arbor, Michigan,)*, pp. 808–811, 2012.

R. Menon, P. Gerstoft and W. S. Hodgkiss, "Cross-correlations of diffuse noise in an ocean environment using eigenvalue based statistical inference", *J. Acoust. Soc. Am.* **132** (5), pp. 3213–3224, 2012.

R. Menon, P. Gerstoft and W. S. Hodgkiss, "Effect of Medium Attenuation on the Asymptotic Eigenvalues of Noise Covariance Matrices", *IEEE Signal Proc. Lett.*, **20**, pp. 435–438, 2013.

R. Menon, P. Gerstoft and W. S. Hodgkiss, "On the Factors Influencing the Estimation of Spatial Coherence From Seismic Arrays", *J. Geophys. Res.*, (to be submitted, 2013).

ABSTRACT OF THE DISSERTATION

Reducing Uncertainty in Estimates of Environmental Parameters From Ambient Noise Using Statistical Array Processing

by

Ravishankar Menon

Doctor of Philosophy in Electrical Engineering
(Applied Ocean Sciences)

University of California, San Diego, 2013

Professor William S. Hodgkiss, Chair
Professor Peter Gerstoft, Co-Chair

In recent years, extracting environmental information from diffuse ambient noise has become an increasingly viable alternative to traditional active source methods. Due to uncontrollable factors such as noise field directionality, presence of spatially compact sources and unknown medium properties, results from ambient noise processing are often biased and need careful interpretation. Thus it is important to develop robust approaches that can perform well in the presence of such detriments.

The first part of the dissertation focuses on interpreting the coherence and attenuation estimates from seismic arrays. Adaptive array processing using stations from

the Southern California Seismic Network is used to identify the presence of multiple seismic waves, namely the fundamental and first mode Rayleigh wave, and body waves. The spatial coherence function (SCF) is modeled as a linear superposition of these waves, with the proportions estimated from data. The SCF shows beating and phase cancellation effects due to the interactions between wavenumbers, which could be misinterpreted as attenuation. The array geometry is also shown to limit the ranges at which the coherence can be estimated well.

The second part of the dissertation focuses on developing statistical techniques to mitigate the effects of spatially compact sources on the noise processing. Analytical expressions are derived for the asymptotic eigenvalues of the true spatial covariance matrix (CM) for a uniform line array in three and two dimensional isotropic noise fields with and without attenuation. Using random matrix theory, the asymptotic probability density of the eigenvalues of the sample covariance matrix (SCM) also is derived in each of these scenarios. These analytical results provide upperbounds for the noise eigenvalues of the SCM.

In the third part of the dissertation, the analytical results are combined with a sequential hypothesis testing framework. This then is used to identify the outliers (which correspond to strong and spatially compact sources) in shallow water ocean acoustic data. The cross-correlation results after rejecting these outliers are shown to be unbiased and converge faster with a higher signal-to-noise ratio. The performance of the eigenvalue rejection technique under different noise model assumptions also is investigated.

1

INTRODUCTION

Exploring an ocean or seismic environment traditionally has been performed using active sources, which transmit known signals into the environment which are then recorded by a set of receivers after being modified by the environment. Sources of opportunity such as earthquakes also have been used to in tomographic applications to image the Earth's interior. Despite their widespread use, the use of active sources is not without its drawbacks. For instance, active sources realistically can only be deployed in regions that readily are accessible. The logistics involved in successfully carrying out an active source experiment in remote locations and the costs involved make this a highly unattractive option. Earthquakes, which are free active sources, primarily occur only at the plate boundaries which limits the profiling resolution in seismically inactive regions.

In recent years, it has been demonstrated both theoretically and experimentally [1–5], that temporal cross-correlations of a diffuse noise field recorded on a pair of receivers yielded the Green's function (impulse response) between those two points, shaped by the spectrum of the noise field. This is in fact the very quantity that is recovered in active source profiling experiments. Since ambient noise is ubiquitous, this result has generated significant interest in retrieving information from the diffuse background noise. This technique has diverse applications such as ocean acoustic in-

terferometry [6,7], passive fathometer [8,9], imaging the interior of the earth [10–12], etc.

1.1 Challenges in Ambient Noise Processing

While the utility of using ambient noise for extracting environmental information has been established in the literature, there remain practical challenges in the processing of ambient noise data and the interpretation of the results. For instance, theory [1,2] has shown that cross-correlations of noise recorded on two sensors in a diffuse noise field yields a set of peaks whose locations correspond to the travel-time for various propagation paths. However, such perfectly diffuse noise fields are seldom realized outside of controlled laboratory experiments.

In shallow waters, the ambient ocean acoustic noise field also contains contributions from strong and spatially compact sources such as ships or other anthropogenic sources. These discrete noise sources often are persistent and overwhelm the cross-correlation results, thus introducing a bias in the travel time estimate [7]. This typically is worked around by either discarding the data that is contaminated by detrimental sources or increasing the averaging time so that their effect is minimized. However, neither of these approaches are appealing if ambient noise processing is to eventually replace traditional active source techniques and be used in real time monitoring systems.

In seismology, although it is easy to remove the transient spatially compact sources (earthquakes) by time-gating, similar biases exist in the travel time estimates due to the directionality of the noise field (e.g. increased microseismic noise near the coasts) [13]. The noise directionality also influences the spatial coherence between two sensors and must be accounted for before interpreting the results [14]. In these cases, increased averaging time does not help reduce the bias since the directionality is characteristic of the environment.

These challenges form the backdrop for the contributions of this dissertation:

1. In order to interpret the information contained in the estimated spatial coherence from an array of sensors, it is important to know the characteristics of the

noise field. Using sensors from the Southern California Seismic Network, the spatial spectrum of the ambient seismic noise field is analyzed and a data driven model for the spatial coherence function is developed. The influence of the array geometry and data processing on the coherence also is studied, which provides valuable constraints on the quality of the estimates.

2. The spatial sample covariance matrix or the cross-spectral density matrix (CSDM) is an important quantity in array processing. By exploiting the symmetry in the CSDM for a uniform line array of sensors in an isotropic noise field, analytical results are obtained for the eigenvalues and eigenvalue densities of the CSDM using random matrix theory (RMT). The resulting density is shown to have finite support on the real axis, which provides an upperbound on the magnitude of the eigenvalues of the CSDM from noise. This is valuable in noise processing applications since the eigenvalues are related to the power of the noise sources, thus providing a means for identifying the strong and spatially compact sources. The results also are extended to the case when there is attenuation in the medium.

3. The eigenvalue bounds thus derived are employed in a statistical testing framework to reject the spatially compact sources. The approach provides a viable alternative to wholesale rejection of contaminated data. By using the aforementioned analytical results and analyzing the data in the eigendomain, only the specific contaminants are rejected leaving much of the remaining data available for use. A significant improvement in the signal-to-noise ratio is also demonstrated and performance of the approach under different noise field assumptions is also studied.

1.2 Spatial Coherence Functions

The spatial coherence function (SCF) of a noise field describes the correlation between the frequency domain response at two sensors in a noise field. SCFs typically are used to study the performance of sensor arrays in noise fields with a specified

directional density function (related to the noise power in each direction). Recent advances in ambient noise interferometry have seen a renewed interest in the study of SCFs of noise fields, because the cross-correlations of noise between sensors (which is then used to retrieve the Green's function between the two points) is related to the SCF by the Fourier transform.

Consider plane waves at a frequency f, impinging on two sensors at positions A and B. From the complex valued signals $\psi_A(f)$ and $\psi_B(f)$ recorded on them, the power spectral densities (PSD) at the sensors is given by

$$P_{ii}(f) = T^{-1}\langle \psi_i(f)\psi_i^{\dagger}(f)\rangle,\ i = \{A, B\}, \tag{1.1}$$

where T is the time interval, † denotes the complex conjugate and $\langle\cdot\rangle$ the ensemble average and the cross-spectral density (CSD) is given by

$$P_{AB}(f) = T^{-1}\langle \psi_A(f)\psi_B^{\dagger}(f)\rangle. \tag{1.2}$$

The SCF between these two sensors is defined as the normalized cross-spectral density,

$$\Gamma_{AB}(f) = \frac{P_{AB}(f)}{\sqrt{P_{AA}(f)P_{BB}(f)}}. \tag{1.3}$$

In a three dimensional, homogeneous, and lossless medium, plane wave noise fields can be considered to be generated by point sources distributed uniformly on the surface of a sphere of infinite radius. Due to the spatial symmetry, the PSD is the same at every point in the field. Consider the CSD of the noise from an infinitesimal solid angle $d\Omega$ incident on two sensors at A and B separated by a distance r [Figure 1.1 (a)]:

$$\begin{aligned} dP_{AB}(f) =& \langle \psi_A(f)\psi_B^{\dagger}(f)\rangle\, d\Omega \\ =& \langle |\psi_A(f)|^2\rangle\ e^{-2\pi i f r\cos(\theta)/c}\ \sin(\theta)\, d\theta\, d\varphi, \end{aligned} \tag{1.4}$$

where c is the velocity of sound in the medium and T is taken to be 1. The second step follows from the fact that the output at B is just a time shifted version of that at A. The PSD is obtained similarly as $dP_{ii}(f) = \langle |\psi_i(f)|^2\rangle\, d\Omega$, for $i = A, B$. Since the PSD is the same everywhere, without loss of generality, we can assume $\langle |\psi_i(f)|^2\rangle$ to be unity.

Integrating over the entire sphere, the SCF is obtained as [15]

$$\Gamma_{AB}^{(3D)}(\beta) = \frac{\int_0^{2\pi}\int_0^{\pi} e^{-2\pi\imath fr\cos(\theta)/c}\sin(\theta)\,d\theta\,d\varphi}{\int_0^{2\pi}\int_0^{\pi}\sin(\theta)\,d\theta\,d\varphi} = \frac{\sin\left(\frac{2\pi fr}{c}\right)}{\left(\frac{2\pi fr}{c}\right)} = \mathrm{sinc}(2\pi\beta) \tag{1.5}$$

where $\beta = fr/c$ is the spacing to wavelength ratio. Thus, the SCF is independent of the position of the sensors and depends only on their separation distance.

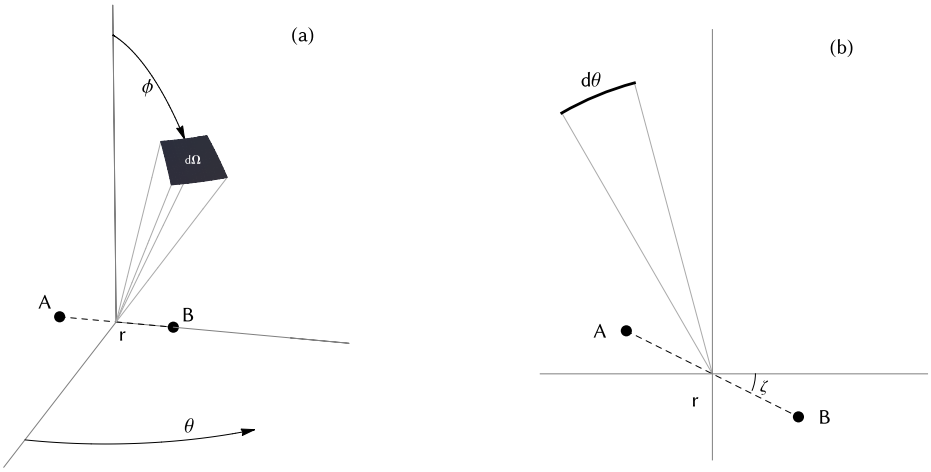

Figure 1.1: Illustration of sensor locations and geometry in (a) three dimensions and (b) two dimensions

Similarly, in a two dimensional, homogeneous and lossless medium, the plane wave noise field can be considered to be generated by point sources distributed uniformly on the circumference of a circle of infinite radius [Figure 1.1 (b)]. Proceeding as before, the SCF is obtained by integrating over the circumference as [16]

$$\Gamma_{AB}^{(2D)}(\beta) = \frac{\int_0^{2\pi} e^{-2\pi\imath fr\cos(\theta)/c}d\theta}{\int_0^{2\pi} d\theta} = \mathrm{J}_0\left(\frac{2\pi fr}{c}\right) = \mathrm{J}_0(2\pi\beta) \tag{1.6}$$

where J_0 is the Bessel function of the first kind and order zero. As in (1.5), the SCF depends only on the separation distance between the sensors.

In Chapter 2, the SCF for the seismic noise field is modeled as a linear combination of the above noise fields. In Chapters 3–6, the SCF is the generating function for the entries of the CSDM matrix.

1.3 Random Matrix Theory

Random matrix theory (RMT) is a branch of mathematics that deals with the study of the eigenvalues of matrices whose elements follow a known probability distribution. RMT first originated in multivariate statistics [17] but gained widespread attention and popularity after Wigner used the distribution of eigenvalues of a random matrix to explain the statistics of energy levels in heavy nuclei [18–21]. Today, RMT has applications in a variety of fields such as finance [22], signal processing [23–25], information theory and wireless networks [26], graph theory [27], elastodynamics [28] and wave propagation and scattering in random media [29–31].

Given an $N \times N$ square matrix $\mathbf{A}$ with eigenvalues a_i, the empirical cumulative distribution (ECD) $\mathrm{P}_{\mathbf{A}}(x)$ of the eigenvalues is defined as

$$\mathrm{P}_{\mathbf{A}}(x) = \frac{\#\{a_n \leq x\}}{N}, \tag{1.7}$$

where $\#$ denotes the cardinality of the set. For certain distributions of the elements of $\mathbf{A}$, in the limit $N \to \infty$ the ECD converges almost surely to a well defined distribution $\mathrm{P}(x)$ [32] and the corresponding probability density function ($d\mathrm{P}(x)/dx$) is often referred to as the asymptotic eigenvalue density. Most results in RMT are derived in an asymptotic setting although they hold good for moderate sized matrices as well. Although the eigenvalues of random matrices have been the primary focus, recent results also discuss the behavior of the eigenvectors [33].

The practical utility of these results primarily are due to the properties of *ergodicity* and *universality*. Ergodicity implies that the asymptotic results are independent of the specific realization of the matrix allowing such results to be applied to a specific instance. Often the asymptotic results hold for different distributions of the matrix

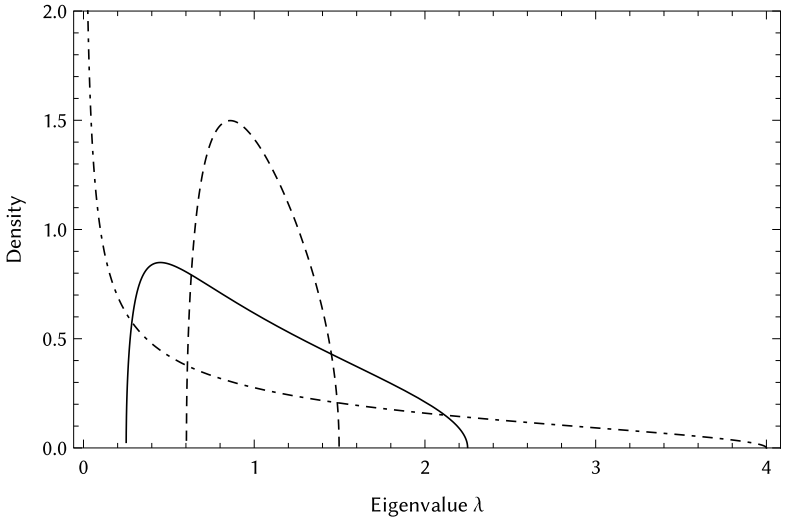

Figure 1.2: Marčenko–Pastur density for different $\nu = N/M$: 0.05 (dashed), 0.25 (solid) and 1 (dot-dashed).

elements, a property referred to as universality, which allows the results to be used in several classes of problems.

In this dissertation, RMT is used to study the eigenvalues of the CSDM, which is a normalized Wishart matrix. Wishart matrices arise frequently in multivariate statistics (covariance and precision matrices), signal processing (cross-spectral density matrices), finance (inter-stock correlation matrix), etc.

Definition 1.1 (Wishart Matrices). *The $N \times N$ matrix $\mathbf{W} = \mathbf{X}\mathbf{X}^H = \sum_{m=1}^{M} \mathbf{x}_m \mathbf{x}_m^H$, where $\mathbf{X} \in \mathbb{C}^{N \times M}$ is a Gaussian random matrix with columns $\mathbf{x}_m \sim \mathcal{CN}(0, \Sigma)$, is called a Wishart matrix with M degrees of freedom, and is denoted $\mathbf{S} \sim \mathcal{W}(\Sigma, M)$*

For the null case when $\Sigma = \mathbf{I}$, the asymptotic eigenvalue density of $\frac{1}{M}\mathbf{W}$ in the limit $N, M \to \infty$ and $N/M = \nu$, is given by the Marčenko–Pastur (MP) density [34],

$$\widehat{\mathrm{p}}_{MP}(\lambda) = \begin{cases} \frac{\sqrt{(l_+ - \lambda)(\lambda - l_-)}}{2\pi\nu\lambda} & l_- < \lambda < l_+ \\ 0 & \text{otherwise} \end{cases} \tag{1.8}$$

where $l_- = (1 - \sqrt{\nu})^2$ and $l_+ = (1 + \sqrt{\nu})^2$ are the upper and lower limits of the "spreading" of the eigenvalues of the SCM around the true eigenvalue which is 1. As shown in Figure 1.2, the spreading of the eigenvalues increases for larger ν (fewer observations

M compared to the dimension N), and as $\nu \to 0$, all eigenvalues are equal to that of the true covariance matrix.

In Chapter 3, expressions similar to (1.8) are derived for the case when Σ corresponds to the CSDM in an isotropic noise field. Corresponding relations for the upperbound (l_+) then are used in Chapter 6 to reject the strong and spatially compact noise sources..

1.4 Scope of This Dissertation

The bulk of this dissertation is contained in four chapters — Chapters 2, 3, 4 and 6. These chapters are a full reprint of papers that were either published in a professional journal or submitted for consideration in one.

Chapter 2 deals with the challenges involved in estimating the spatial coherence using a random array of sensors in a directional noise field. The seismic noise field in the 0.05–0.2 Hz band primarily is due to microseisms, which are continuous seismic background noise generated by ocean waves. The SCF typically is modeled as a superposition of plane waves propagating along the surface (fundamental mode Rayleigh waves). Using adaptive beamforming on stations from the Southern California Seismic Network, we identify the presence of higher mode Rayleigh waves. In addition, body waves that are generated in the deep ocean from distant storms and propagate through the Earth's mantle and core, also are consistently observed in the microseism band. An improved model for the seismic SCF then is obtained by incorporating the effect of these waves as linear combinations of the elementary SCFs in Chapter 1.2. The resulting SCF shows beating and phase cancellation effects from interactions between the different wavenumbers associated with the different seismic waves and these could be misidentified as being due to attenuation in the medium. The influence of the array geometry and signal processing techniques on the estimation of coherence also is discussed and taken into consideration.

Chapter 3 derives the asymptotic eigenvalues of the true noise covariance matrix (CM) for a line array with equidistant sensors in an isotropic noise field. The CM in the frequency domain is a symmetric Toeplitz sinc matrix which is shown to have

at most two distinct eigenvalues in the asymptotic limit of an infinite number of sensors. For line arrays with inter-element spacing less than half a wavelength, the CM turns out to be rank deficient, which has implications in algorithms that require the inverse of the CM. The asymptotic eigenvalue density of the spatial sample covariance matrix (SCM) or CSDM then is derived using RMT for all ratios of the inter-element spacing to the wavelength. These analytical results are useful because they provide an upperbound on the eigenvalues of the SCM from background noise. These then can be used to determine statistically those eigenvalues that are due to detriments (e.g. nearby ships) in the noise field as is done in Chapter 6.

Chapter 4 derives analytical expressions for the eigenvalues of the CM in the presence of attenuation. It is shown that attenuation has effects similar to that of a low-pass filter and tends to raise the value of the lower eigenvalues while lowering those of the large eigenvalues. The asymptotic eigenvalue density for the SCM in this case is obtained as an approximation using the polynomial method of random matrices [35, 36].

Chapter 5 examines the eigenvalues of the SCM for a towed array in deep water. The coherent noise is modeled as in Chapters 3 and 4 and it is shown that the eigenvalues from data compare well with theory. The eigenvalues also show a sharp drop in power for element spacing to wavelength ratios less than 1/2, which is related to the edge of the visible region.

Chapter 6 applies the theoretical results in Chapter 3 to shallow water experimental data. As mentioned in Section 1.1, the influence of spatially compact sources in the ocean (usually ships) often results in a bias of the travel time estimates obtained from the cross-correlations. A sequential hypothesis testing framework using the analytical results of Chapter 3 is developed. Applying the test to acoustic data from the Shallow Water 2006 experiment reveals eigenvalues dominated by loud sources that are statistical outliers for the assumed diffuse noise model. Travel times obtained from cross-correlations using only the diffuse noise component (i.e., by discarding or attenuating the outliers) converge to the predicted travel times based on the known array sensor spacing and measured soundspeed at the site. These estimates are also stable temporally, thus demonstrating the effectiveness of this approach.

Finally, Chapter 7 presents the conclusions and possible future extensions of this research.

Bibliography

[1] O. I. Lobkis and R. L. Weaver, "On the emergence of the Green's function in the correlations of a diffuse field," *J. Acoust. Soc. Am.*, vol. 110, pp. 3011–3017, December 2001.

[2] R. L. Weaver and O. I. Lobkis, "Ultrasonics without a source: Thermal fluctuation correlations at MHz frequencies," *Phys. Rev. Lett.*, vol. 87, p. 134301, 2001.

[3] R. Snieder, "Extracting the Green's function from the correlation of coda waves: A derivation based on stationary phase," *Phy. Rev. E.*, vol. 69, p. 046610, 2004.

[4] K. Wapenaar, "Retrieving the elastodynamic Green's function of an arbitrary inhomogeneous medium by cross-correlation," *Phys. Rev. Lett.*, vol. 93, p. 254301, 2004.

[5] O. A. Godin, "Recovering the Acoustic Green's Function from Ambient Noise Cross Correlation in an Inhomogeneous Moving Medium," *Phys. Rev. Lett.*, vol. 97, p. 054301, Aug 2006.

[6] P. Roux, W. A. Kuperman, and the NPAL group, "Extracting coherent wave fronts from acoustic ambient noise in the ocean," *J. Acoust. Soc. Am.*, vol. 116, pp. 1995–2003, 2004.

[7] L. A. Brooks and P. Gerstoft, "Green's function approximation from cross-correlations of 20–100 Hz noise during a tropical storm," *J. Acoust. Soc. Am.*, vol. 125, pp. 723–734, Jan 2009.

[8] M. Siderius, C. H. Harrison, and M. B. Porter, "A passive fathometer technique for imaging seabed layering using ambient noise," *J. Acoust. Soc. Am.*, vol. 120, pp. 1315–1323, 2006.

[9] J. Traer, P. Gerstoft, and W. S. Hodgkiss, "Ocean bottom profiling with ambient noise: A model for the passive fathometer," *J. Acoust. Soc. Am.*, vol. 129, no. 4, pp. 1825–1836, 2011.

[10] N. M. Shapiro, M. Campillo, L. Stehly, and M. H. Ritzwoller, "High-resolution surface-wave tomography from ambient seismic noise," *Science*, vol. 307, pp. 1615–1618, 2005.

[11] P. Gerstoft, K. G. Sabra, P. Roux, W. A. Kuperman, and M. C. Fehler, "Green's functions extraction and surface-wave tomography from microseisms in southern California," *Geophysics*, vol. 71, pp. SI23–SI31, 2006.

[12] P. Gouédard, L. Stehly, F. Brenguier, M. Campillo, Y. C. de Verdière, E. Larose, L. Margerin, P. Roux, F. J. Sánchez-Sesma, N. M. Shapiro, and R. L. Weaver, "Cross-correlation of random fields: mathematical approach and applications," *Geophysical Prospecting*, vol. 56, pp. 375–393, 2008.

[13] J. Yao and R. van der Hilst, "Analysis of ambient noise energy distribution and phase velocity bias in ambient noise tomography, with application to SE Tibet," *Geophys. J. Int.*, vol. 166, pp. 732–744, 2009.

[14] V. C. Tsai, "Understanding the amplitudes of noise correlation measurements," *Journal of Geophysical Research: Solid Earth (1978–2012)*, vol. 116, no. B9, 2011.

[15] C. H. Eckart, "The theory of noise in continuous media," *J. Acoust. Soc. Am.*, vol. 25, no. 2, pp. 195–199, 1953.

[16] M. J. Jacobson, "Space-time correlation in spherical and circular noise fields," *The Journal of the Acoustical Society of America*, vol. 34, p. 971, 1962.

[17] J. Wishart, "The generalized product moment distribution in samples from a normal multivariate population," *Biometrika*, vol. 20A, pp. 32–52, 1928.

[18] E. P. Wigner, "On the statistical distribution of the widths and spacings of nuclear resonance levels," *Mathematical Proceedings of the Cambridge Philosophical Society*, pp. 790–798, 1951.

[19] E. P. Wigner, "On the distribution of the roots of certain symmetric matrices," *The Annals of Mathematics*, vol. 67, no. 2, pp. 325–327, 1958.

[20] E. Wigner, "Distribution laws for the roots of a random hermitian matrix," *Statistical Theories of Spectra: Fluctuations*, pp. 446–461, 1965.

[21] E. P. Wigner, "Random matrices in physics," *Siam Review*, vol. 9, no. 1, pp. 1–23, 1967.

[22] V. Plerou, P. Gopikrishnan, B. Rosenow, L. A. N. Amaral, and H. E. Stanley, "Universal and nonuniversal properties of cross correlations in financial time series," *Phys. Rev. Lett.*, vol. 83, no. 7, pp. 1471–1474, 1999.

[23] R. R. Nadakuditi and A. Edelman, "Sample eigenvalue based detection of high-dimensional signals in white noise using relatively few samples," *IEEE Trans. Signal Proc.*, vol. 56, no. 7, pp. 2625–2638, 2008.

[24] R. R. Müller, "A random matrix model of communication via antenna arrays," *IEEE Trans. Info. Theory*, vol. 48, no. 9, pp. 2495–2506, 2002.

[25] R. R. Nadakuditi and J. W. Silverstein, "Fundamental limit of sample generalized eigenvalue based detection of signals in noise using relatively few signal-bearing and noise-only samples," *IEEE J. Sel. Top. Signal Proc.*, vol. 4, no. 3, pp. 468–480, 2010.

[26] A. M. Tulino and S. Verdú, "Random matrix theory and wireless communications," *Foundations and Trends in Communications and Information Theory*, vol. 1, no. 1, pp. 1–182, 2004.

[27] R. R. Nadakuditi and M. E. Newman, "Graph spectra and the detectability of community structure in networks," *Physical Review Letters*, vol. 108, no. 18, p. 188701, 2012.

[28] R. L. Weaver, "Spectral statistics in elastodynamics," *J. Acoust. Soc. Am.*, vol. 85, pp. 1005–1013, 1989.

[29] A. Aubry and A. Derode, "Random matrix theory applied to acoustic backscattering and imaging in complex media," *Phys. Rev. Lett.*, vol. 102, p. 084301, 2009.

[30] A. Aubry and A. Derode, "Detection and imaging in a random medium: A matrix method to overcome multiple scattering and aberration," *J. Appl. Phys.*, vol. 106, p. 044903, 2009.

[31] S. E. Skipetrov and A. Goetschy, "Eigenvalue distributions of large Euclidean random matrices for waves in random media," *J. Phys. A: Math. Theor.*, vol. 44, p. 065102, 2011.

[32] J. W. Silverstein, "Strong convergence of the empirical distribution of eigenvalues of large dimensional random matrices," *J. Multivar. Anal.*, vol. 54, pp. 175–192, 1995.

[33] F. Benaych-Georges and R. R. Nadakuditi, "The eigenvalues and eigenvectors of finite, low rank perturbations of large random matrices," *Advances in Mathematics*, vol. 227, no. 1, pp. 494–521, 2011.

[34] V. A. Marčenko and L. A. Pastur, "Distributions of eigenvalues of some sets of random matrices," *Math. Sb.*, vol. 72, pp. 507–536, 1967.

[35] N. R. Rao and A. Edelman, "The polynomial method for random matrices," *Foundations of Computational Mathematics*, vol. 8, no. 6, pp. 49–702, 2008.

[36] S. R. Tuladhar, J. R. Buck, and K. E. Wage, "Approximate eigenvalue distribution of a cylindrically isotropic noise sample covariance matrix," *IEEE Stat. Signal Proc. Workshop (Ann Arbor, Michigan)*, pp. 828–831, 2012.

2

FACTORS INFLUENCING THE ESTIMATE OF SPATIAL COHERENCE FROM SEISMIC ARRAYS

Recent studies have demonstrated that the coherence of seismic noise between two stations can be used to retrieve the phase velocity and attenuation. In this article, we study some of the factors that influence the estimate of the coherence in the microseism band (0.05–0.2 Hz). High resolution adaptive beamforming using stations from the Southern California Seismic Network shows a persistent presence of a higher mode Rayleigh and body waves are consistently observed in the microseism band. The presence of multiple seismic waves has implications for the spatial coherence function (SCF) between pairs of sensors. Assuming only the fundamental mode Rayleigh wave and a uniform noise distribution, the SCF is a zeroth order Bessel function with a wavenumber corresponding to the fundamental. Here, the SCF is modeled as a sum of the SCF for each wavetype and such a model is shown to better describe the observed coherence. The resulting SCF shows multi-path effects from interactions between the wavenumbers associated with the different seismic waves, and these could be misidentified as being due to attenuation or focusing and defocusing effects from anisotropy in the medium. The estimated coherence from the data also is influenced by other fac-

tors such as the geometry of the array, inhomogenities in the medium and the data processing.

2.1 Introduction

There has been significant interest over the past decade, in using the seismic ambient noise field for various applications such as surface wave tomography [1–3], seismic imaging [4] and studies of phase velocity anisotropy [3], among several others. Much of this interest stemmed from the observation that averaging the cross-correlations of diffuse waves between a pair of receivers yielded the Green's function between the two points [5, 6], followed by several key theoretical developments [7–9] and experimental evidence of its success [10–13].

Recently, several works have focused on using the coherence (normalized cross-spectral density) of seismic noise between two stations to retrieve the medium phase slowness and the frequency dependent attenuation coefficient [14–18]. Estimates of attenuation inherently are more difficult because they are influenced in non-trivial ways by several factors such as noise directionality [19], site amplification factors, focusing and defocusing effects [20], and scattering in the medium. The noise directionality can be overcome by binning the coherence into distinct distance bins and averaging the observations in each bin amounts to an azimuthal average, which renders the noise field reasonably isotropic [15]. However, [21] and [22] demonstrated numerically that in order to recover the attenuation from noise cross-correlations, the noise distrubution must be known. Using a ray-theoretical framework to analyze the effect of source distribution on the amplitudes of noise cross-correlations and coherence, it was shown that the azimuthal anisotropy impacts the amplitudes significantly, and is not overcome by averaging [23].

In this article we investigate the influence of array processing and the noise field on the estimate of the coherence. Although averaging is ubiquitous in ambient noise applications, depending on the quantity being averaged, it can result in biased estimates or produce altogether incorrect results. For example, in section 2.4 and 2.4.2 we discuss how the geometry of the array (here SCSN) impacts the coherence estimate

due to decreasing number of raypaths with distance. Likewise, averaging neighboring frequency bins to obtain a stable result can introduce attenuation-like behavior due to the oscillatory nature of the coherence.

Adaptive beamforming on the Southern Californa Seismic Network (SCSN) array (section 2.3.3) in the microseism band (0.05–0.2 Hz) shows persistent higher mode Rayleigh waves and body waves between 0.12–0.2 Hz (section 2.5.1). Microseisms are continuous seismic signals generated by ocean waves, classified simply as single frequency (SF) or double frequency (DF) microseisms. Here, the terms refer to the frequency bands: 0.05–0.12 Hz for the SF and 0.12–0.2 Hz for the DF microseisms. Although higher mode Rayleigh waves have been reported previously [24–26], and P-waves from pelagic storms are also known to be present at the higher frequencies [24, 27–30], the coherence is often modeled as only consisting of the fundamental mode. Modeling the coherence as a linear superposition of the different seismic waves, and results show that it better describes the coherence estimated from data (section 2.6), than the simple isotropic model.

2.2 Background

2.2.1 Spatial Coherence Functions

The spatial coherence function (SCF) of a noise field describes the correlations between the response at two stations in the frequency domain. Consider seismic surface waves at a frequency f, with a normalized azimuthal weight function $W(\theta)$, incident on two stations A and B positioned r apart with an interstation azimuth of ζ. From the complex valued signals $\psi_A(f)$ and $\psi_B(f)$ recorded, the cross-spectral density (CSD) is given by

$$P_{AB}(f) = T^{-1}\langle \psi_A(f)\psi_B^{\dagger}(f)\rangle, \tag{2.1}$$

where T denotes the time interval, † denotes the complex conjugate and $\langle\cdot\rangle$ the ensemble average. The SCF between these two sensors is defined as the normalized cross-spectral density,

$$\Gamma(r,\zeta) = \frac{P_{AB}(f)}{\sqrt{P_{AA}(f)P_{BB}(f)}}, \tag{2.2}$$

where $P_{AA}(f) = T^{-1}\langle \psi_A(f)\psi_A^\dagger(f)\rangle$ and $P_{BB}(f) = T^{-1}\langle \psi_B(f)\psi_B^\dagger(f)\rangle$ are the respective power spectral densities.

Following [31, equation (19)], the SCF for a given noise distribution $W(\theta)$ is obtained by integrating over all azimuths, as:

$$\begin{aligned}\Gamma_{2D}(r,\zeta) &= \frac{1}{2\pi}\int_0^{2\pi} W(\theta)\exp\left(\imath 2\pi fr\cos(\theta-\zeta)s\right)\mathrm{d}\theta \\ &= \sum_{\nu=0}^{\infty} \imath^\nu \varepsilon_\nu \mathrm{J}_\nu(2\pi frs)\left[a_\nu\cos(\nu\zeta)+b_\nu\sin(\nu\zeta)\right] \end{aligned} \tag{2.3}$$

where s is the frequency dependent slowness (inverse phase velocity) of the medium, ε_ν is 1 for $\nu = 0$ and 2 otherwise, and a_ν, b_ν are the Fourier coefficients of $W(\theta)$. Thus for arbitrary noise fields, the SCF depends on the inter-station azimuth ζ. When the noise field is isotropic, then $W(\theta) = 1$ and only the $\nu = 0$ term is non-zero, and the SCF is $\Gamma_{2D}(r) = \mathrm{J}_0(2\pi frs)$ [32], i.e. it is independent of the interstation azimuth ζ and is simply a function of the frequency f and the separation distance r.

For body waves, which propagate three dimensionally, the SCF for a noise distribution $W(\theta,\varphi)$ is given by [31, equation (43)],

$$\begin{aligned}\Gamma_{3D}(r,\zeta,\xi) =& \frac{1}{4\pi}\int_0^{2\pi}\int_0^{\pi} W(\theta,\varphi)\sin(\theta)\exp\left[\imath 2\pi frs\right. \\ &\left.\times\left(\sin(\theta)\sin(\xi)\cos(\varphi-\zeta)+\cos(\theta)\cos(\xi)\right)\right]\mathrm{d}\theta\,\mathrm{d}\varphi \\ =& \sum_{n=0}^{\infty}\sum_{m=0}^{\infty}\imath^n \mathrm{P}_n^m(\cos(\xi))j_n(2\pi frs) \\ &\times\left[a_n^m\cos(m\xi)+b_n^m\sin(m\xi)\right] \end{aligned} \tag{2.4}$$

where ξ is the inter-station angle from the z-axis, P_n^m is the associated Legendre function of the first kind, order m and degree n, a_n^m and b_n^m are the coefficients in the spherical harmonic expansion of $W(\theta,\varphi)$ and j_n is the spherical Bessel function of order n. When the noise field is isotropic, then $W(\theta,\varphi) = 1$ and only the $n = 0$ term remains, and the SCF is $\Gamma_{3D} = j_0(2\pi frs)$ [33] (or sinc).

The effect of medium attenuation on the coherence often is modeled by a multiplicative exponential term, $e^{-\alpha r}$, where α is the attenuation coefficient [15, 34–36]. The coherence (in 2D) then is written as

$$\Gamma_\alpha(r,\zeta) = e^{-\alpha r}\Gamma(r,\zeta) \tag{2.5}$$

where Γ_α denotes the SCF with attenuation. When the noise field is isotropic, (2.5) reduces to $\Gamma_\alpha(r) = e^{-\alpha r} \mathrm{J}_0(2\pi frs)$, which is the relation used for attenuation tomography [15, 16]. However, recent works [20, 23, 37] suggest that the attenuation factor in the coherence due to an isotropic surface wave field might not be exponential.

2.2.2 Estimating the SCF from seismic arrays

In general, the seismic ambient noise field is not isotropic, and the observed coherence between station pairs depends on the distribution of noise sources [23, 31]. High density seismic networks such as the SCSN have several station pairs of varying inter-station azimuths and distances (over 10000 pairs for SCSN). It then is possible to leverage the multitude of pairs available at a certain distance of separation to mitigate the effect of the directionality of the noise field, at the cost of assuming uniform medium properties for the entire study region.

[15] suggested averaging the observed coherence for multiple station pairs at a fixed separation distance, to approximate an isotropic noise distribution. Mathematically, this can be seen by integrating (2.3) over all station pair azimuths (ζ from 0 to 2π). Regardless of the noise distribution $W(\theta)$, only the $\nu = 0$ term remains.

From the observed inter-station coherencies $\widehat{\Gamma}(r_{ij}, \zeta_{ij})$, the "average spatial coherence" (ASC) for the array is obtained by binning the observations into Δ_d wide bins and averaging them [15]. The average coherence $\tilde{\Gamma}_n$ for the nth distance bin d_n is obtained as

$$\tilde{\Gamma}_n = \Re \left\langle \widehat{\Gamma}(r_{ij}, \zeta_{ij}) \right\rangle \; \forall (i,j) \in \mathcal{D}_n \tag{2.6}$$

where $\mathcal{D}_n = \{(i,j) \mid d_n \leq r_{ij} < d_{n+1}\}$ is the set of station pairs in the nth distance bin and $\Re$ denotes the real component. The imaginary part of the ASC is zero for a symmetric $W(\theta)$ and the averaging reduces the imaginary part [15, 38], thus justifying the use of only the real part.

The diminishing number of raypaths with increasing distance of separation and lack of raypaths along certain azimuths (especially at greater distances) are important to the interpretation of the observed ASC (section 2.8).

2.3 Data and Signal Processing

2.3.1 Pre-processing

Data recorded on broadband seismic stations in southern California [Figure 2.3 (a)] were collected for the entire year of 2007 at a sampling rate of 1 Hz. We use only the vertical component data in the 0.05–0.2 Hz frequency range. After removing instrument glitches in the raw data, the data were divided into snapshots of 1800 s each (30 minutes), windowed with a Blackman–Harris window and Fourier transformed with a 2048 point fast Fourier transform.

Earthquakes and other teleseismic events tend to skew the results in noise processing due to their disproportionate power compared to the background noise field. We remove outliers in the data by computing the median of the snapshot power across a 24 hour sliding window for each frequency, and discarding snapshots that have powers that are more than 1.5 median absolute deviations away from the median [39]. This approach has similarities to time domain techniques that use the ratio of the peak amplitude to the root mean square amplitude as a rejection criterion [40]. In the frequency domain, a different threshold can be used at each frequency.

2.3.2 The Normalized Cross-Spectral Density Matrix

The spatial covariance matrix (SCM) or the cross-spectral density matrix from M observations of the N dimensional snapshot vector $\mathbf{x}_m = [x_{m1}, \cdots, x_{mN}]^T$, where N is the number of stations, is defined as

$$\widehat{\Sigma} = \frac{1}{M} \sum_{m=1}^{M} \mathbf{x}_m \mathbf{x}_m^H. \tag{2.7}$$

In general, due to site amplification factors or differences in sensor characteristics, the powers at different sensors are not identical. The normalized cross-spectral density matrix (CSDM) is:

$$\widehat{\Sigma}' = \chi \widehat{\Sigma} \chi^T, \tag{2.8}$$

where $\chi = \mathrm{diag}([\frac{1}{\sqrt{\widehat{\Sigma}_{11}}}, \cdots, \frac{1}{\sqrt{\widehat{\Sigma}_{NN}}}])$, and the site amplifications are removed as sources of uncertainty.

We compute the CSDM for each month, using the snapshots that satisfy the criteria in section 2.3.1. With the normalization in (2.8), the *ij*th element of the CSDM gives an *M*-sample estimate of the coherence between the *i*th and *j*th station pair as in (2.2).

2.3.3 High Resolution Capon Beamforming

For a given frequency f, azimuth θ, and slowness s, the plane wave look vector $\mathbf{v}(\theta, s)$ is given by:

$$\mathbf{v}(\theta, s) = \frac{1}{\sqrt{N}} e^{\imath 2\pi f \mathbf{p}_\theta s} \tag{2.9}$$

where the projection vector

$$\mathbf{p}_\theta = [\mathbf{r}_1 \cdot \mathbf{u}_\theta, \ldots, \mathbf{r}_N \cdot \mathbf{u}_\theta]^T, \tag{2.10}$$

$\mathbf{r}_i$ is the position vector of the ith station (with the origin at the mean latitude and longitude), and $\mathbf{u}_\theta$ is the unit vector along θ.

The weight vector $\mathbf{w}(\theta, s)$ for the Capon beamformer [41] (or the minimum variance distortionless response beamformer) is constrained to have unit gain in the look direction, while at the same time minimizing the output power, thus leading to the optimal weights

$$\mathbf{w}_{\text{mvdr}}(\theta, s) = \frac{\widehat{\Sigma}'^{-1}\mathbf{v}(\theta, s)}{\mathbf{v}^H(\theta, s)\widehat{\Sigma}'^{-1}\mathbf{v}(\theta, s)} \tag{2.11}$$

If $\widehat{\Sigma}'^{-1}$ is not invertible (for noise processing, $M > N$, and $\widehat{\Sigma}'$ often is invertible due to uncorrelated noise), then the matrix can be made full rank by loading the diagonal to constrain the white noise gain [42]. In comparison, the weights for the conventional beamformer are given by $\mathbf{w}_{\text{conv}}(\theta, s) = \mathbf{v}(\theta, s)$. The beamformer outputs then are given by

$$B_{(\cdot)} = \mathbf{w}_{(\cdot)}^H \widehat{\Sigma}' \mathbf{w}_{(\cdot)} \tag{2.12}$$

2.4 Factors Influencing the Coherence

Factors independent of the noise field or the environment such as limitations imposed by the array geometry and artifacts from data processing can affect the esti-

mate of the coherence. Understanding these issues is beneficial in the interpretation of the coherence estimates in Section 2.6.

2.4.1 Diminishing Raypaths With Distance

Figure 2.1 (a) shows a smoothed 2D histogram of the station pairs density along distance and azimuth range for the entire SCSN. The SE-NW bias of the inter-station azimuths (arising due to the layout of the stations along the Bight) is evident from the higher density of station pairs between 80–140°. The distribution is symmetric, so only 0–180° is shown. The distribution becomes thin beyond about 350 km, occupying progressively fewer azimuths.

It is useful to have a simple rule of thumb for selecting the range in which the ASC is well estimated. This can be derived intuitively for random regional arrays such as the SCSN. Assuming the stations are normally distributed in range in all directions around the mean latitude and longitude (around 34° N, 117° W for the SCSN), then the number of raypaths with distance is Rayleigh distributed. The raypath distribution for the SCSN (solid) is shown in Figure 2.1 (b) and it resembles a Rayleigh distribution with its mode at about 160 km (the deviation is explained by the higher station density in the Los Angeles basin thus having more shorter paths).

From the histograms in Figure 2.1 (a) and (b), it is clear that the ASC generally is better estimated between about 20–380 km (over 10 raypaths/km) and bins outside this range generally provide noisy estimates. Using the ASC estimates outside this range to estimate the true SCF or attenuation might result in biased results.

2.4.2 Uneven Azimuthal Distribution of Raypaths

Figure 2.1 (c)–(f) shows the distribution of the inter-station azimuths (every 15°) at different distance bins (sector plots), and the individual station pairs that belong to the bin. While in principle, equation (2.6) amounts to an azimuthal average across all station pairs, in practice, this average is biased because of the layout of the array (e.g. a NW–SE bias in the SCSN). The potential bias arising from increased number of station pairs along certain azimuths [see the increased density of stations between

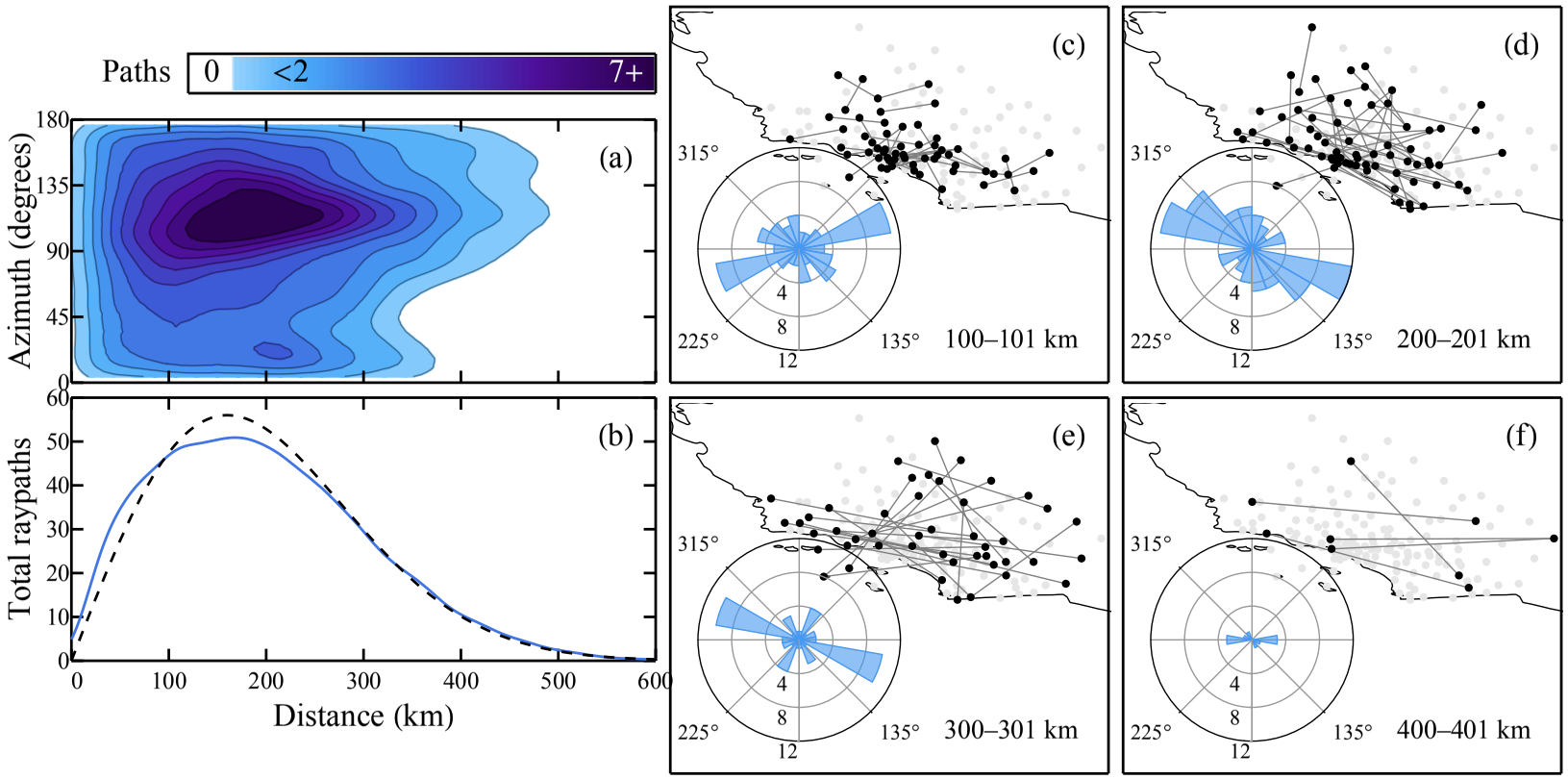

Figure 2.1: (a) Smoothed 2D histogram of the inter-station distances and azimuths for stations in the Southern California Seismic Network. (b) Raypath histogram with distance (solid) approximated by a Rayleigh distribution (dashed). (c)–(f) Inter-station azimuthal distribution (sector chart) at different distance bins showing the azimuthal bias at smaller separations and lack of sufficient station pairs at larger separations. The station pairs that are present in each bin is shown by the connected pairs.

90–135° azimuth in Figure 2.1 (a) and also excess paths along 250° in (c) and (e) and along 280–315° in (d)] can be reduced by implementing an azimuthal binning.

We bin the station pairs in $\mathcal{D}_n$ into Δ_θ wide azimuth bins, compute the mean in each range bin and then azimuthally average the means, in order to ensure a more equal weighting from all azimuths. The ASC then is given by

$$\tilde{\widehat{\Gamma}}'_n = \Re\left\langle \sum_l \frac{1}{\#\mathcal{A}_{ln}} \widehat{\Gamma}(r_{ij}, \zeta_{ij}),\ (i,j) \right\rangle \forall \in \mathcal{A}_{ln} \tag{2.13}$$

where $\mathcal{A}_{ln} = \{(i,j) \mid \theta_l \le \zeta_{ij} < \theta_{l+1}, (i,j) \in \mathcal{D}_n\}$ is the set of station pairs that are in the nth distance bin and lth azimuth bin θ_l, and # denotes cardinality of the set (empty sets are not considered). The ASC $\tilde{\widehat{\Gamma}}'$ is estimated by substituting $\widehat{\Gamma}(r_{ij}, \zeta_{ij}) = \widehat{\Sigma}'_{ij}$ in (2.13).

Equations (2.6) and (2.13) are identical when each azimuth has the same number of inter-station pairs. However, a drawback of (2.13) is that it ignores the variances at different azimuths [as does (2.6)], since the noise distribution and the anisotropy in the region are unknown. In other words, it weights azimuth bins with just a single path (poorly estimated) the same as bins with a large number of raypaths (well estimate) [e.g., see azimuthal distribution of raypaths for 300-301 km in Figure 2.1 (e)].

2.4.3 Interference Due to Frequency Averaging

It is common in signal processing to average neighboring frequency bins to get a robust estimate of the frequency content in the bin centered at f_c, at the expense of an increased bandwidth. Since each frequency bin is associated with a different wavenumber ($k = 2\pi fs$), such an averaging will introduce attenuation-like effects in the coherence due to wavenumber interference.

For example, consider isotropic surface noise with a white power spectrum in a lossless medium. Using a sampling frequency of 1 Hz and an FFT length of 2048 points, the bin width is $\Delta f \approx 0.48$ mHz. Thus, averaging 10 bins centered at $f_c \approx 0.14$ Hz gives an effective bandwidth of ≈ 4.8 mHz. As a result of this averaging, the SCF then is an average of the SCF at each individual bin.

Figure 2.2 (a) shows the individual SCFs for different frequency bins that were averaged. At greater separation distances, the coherences are sufficiently out of phase from one another to introduce intereference effects. As seen in Figure 2.2 (b), the result

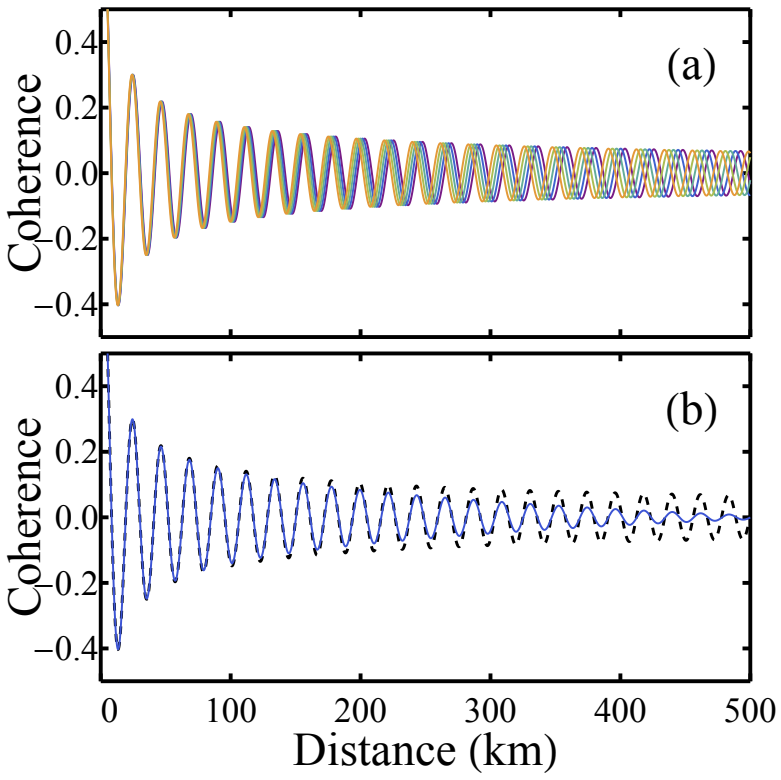

Figure 2.2: (a) Variation in SCF for a 2D isotropic noise field in a lossless medium within a 4.8 mHz bandwidth centered at 0.14 Hz (10 frequency bins; only every other bin is shown for clarity) (b) Resulting SCF due to frequency averaging (solid), showing apparent attenuation relative to the true SCF at 0.14 Hz (dashed).

of such an average introduces an apparent attenuation (solid) that was not originally present in the true SCF (dashed).

Fitting an $e^{-\alpha r}$ model to the apparent attenuation gives $\alpha \approx 1.9 \times 10^{-3}$ km^{-1}, which is similar to previously published values for the attenuation coefficient [43] (values for α from apparent attenuation vary from 1.3×10^{-3} km^{-1} at 0.05 Hz to 2.5×10^{-3} km^{-1} at 0.2 Hz for the scenario above). Thus it is important to minimize frequency averaging, and if performed, the possibility of apparent attenuation must be taken into consideration.

2.5 The Ambient Seismic Noise Field

Capon and conventional beamformer output is shown at different frequencies and months in Figure 2.3 (the beamforming is performed by discretizing the $\theta - s$ space every 1° from 0–360° in the azimuth and every 0.0025 s/km from 0.15–0.4 s/km slowness). The frequencies and months were chosen to highlight different aspects of the seismic noise field, namely:

1. SF and DF microseism noise that propagates as fundamental mode Rayleigh wave ($\mathcal{R}_0$) and appear predominantly from the west [Figure 2.3 (b)–(d), between 0.3–0.33 s/km slowness] [44].

2. First mode Rayleigh wave ($\mathcal{R}_1$), usually seen between 0.12–0.2 Hz [Figure 2.3 (c) at about 0.23 s/km slowness; also see section 2.5.1]

3. Body waves from distant storms and $\mathcal{R}_0$ (and often $\mathcal{R}_1$) at the lower end of the DF microseism band [Figure 2.3 (d) at < 0.1 s/km slowness] [28]. Also, weak body wave signals in the SF microseism band [Figure 2.3 (b)]

4. Dominant body waves from storms at the higher end of the DF microseism band [Figure 2.3 (i); see also [29]]

These waves are present at predictable times and frequencies, showing that the seismic noise field is composed of much more than just $\mathcal{R}_0$. This forms the basis for further discussion in sections 2.6 and 2.7.

2.5.1 Fundamental and Higher Mode Rayleigh Waves

Excitation of Rayleigh waves in a layered, anisotropic medium generates higher modes in addition to the fundamental, with the frequency–phase speed relationship given by the dispersion equation. Barring a few exceptions [24–26, 45], most studies using seismic noise only retrieve the dominant fundamental mode Rayleigh wave. We observe consistent and significant contributions from both the $\mathcal{R}_0$ and $\mathcal{R}_1$ of the Rayleigh waves in the DF microseism frequency band (0.12–0.2 Hz) in addition to P wave microseisms (section 2.5.2).

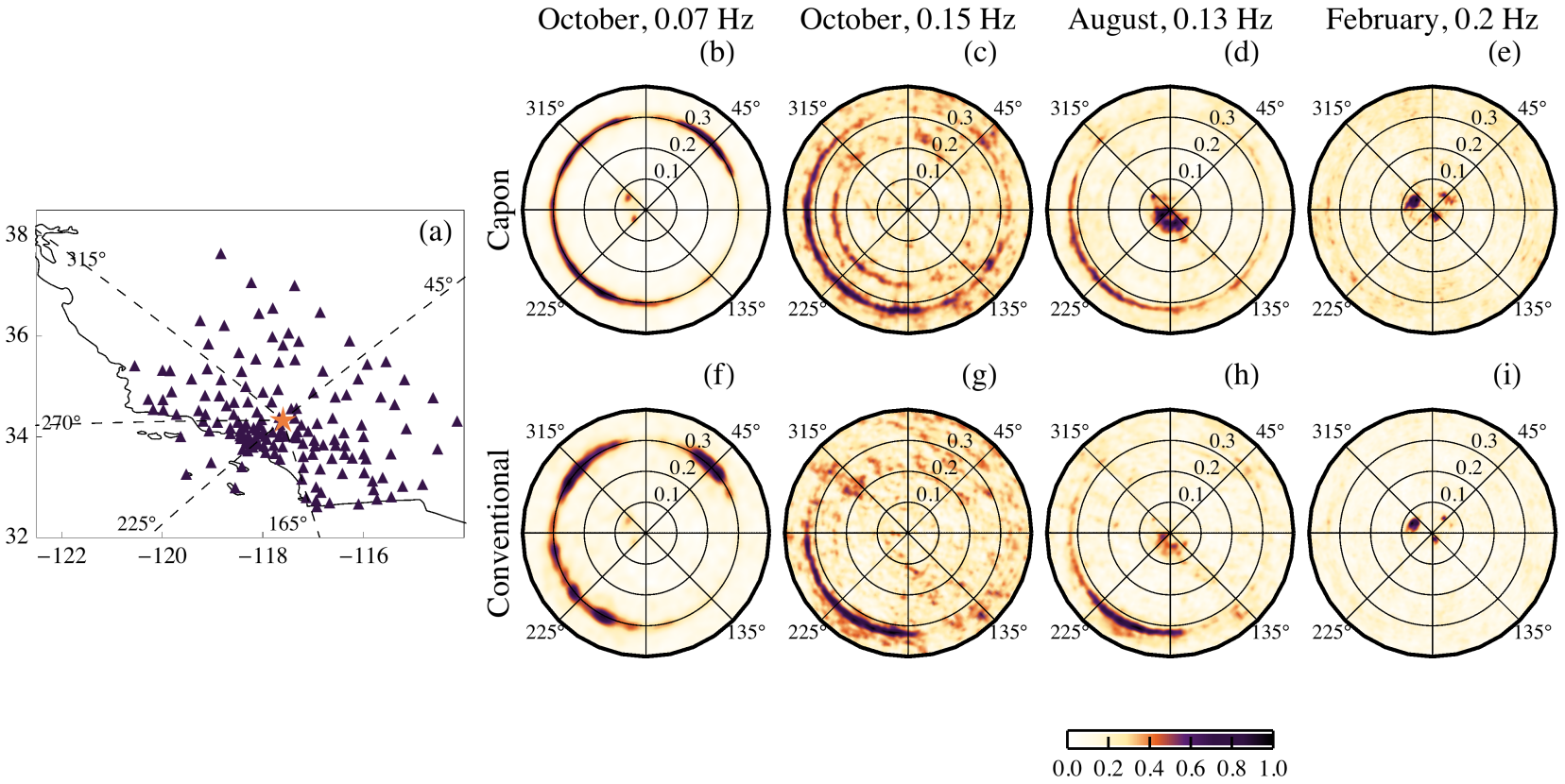

Figure 2.3: (a) Stations in the Southern California Seismic Network (▲) and key azimuths (dashed) from the center of the array (★). (b)–(d) Capon beamformer outputs for different months and frequencies normalized by the maximum in each panel. The first mode of the surface Rayleigh wave, $\mathcal{R}_1$, is seen in the DF microseism band (c). Body waves from distant storms are also seen at slownesses less than 0.1 s/km. (f)–(i) Conventional beamformer outputs for the same month and frequencies as in (b)–(e). The higher mode is not observable due to the lower resolution of the conventional beamformer.

Figure 2.4 shows the Capon beamformer output for all months in 2007 between 0.15–0.4 s/km slowness. The $\mathcal{R}_1$ wave is consistently observed at 0.24 s/km slowness, alongside the $\mathcal{R}_0$ at 0.32 s/km. The generating regions of $\mathcal{R}_1$ are confined to a smaller azimuthal region to the west of the array than $\mathcal{R}_0$. They are observed at other azimuths when accompanied by powerful storms such as those in the Labrador Sea and N Atlantic Ocean in the winter months [see 30°–60° in Figure 2.3 (a) and (b)], or hurricanes in the Gulf of Mexico and the Atlantic Ocean [see 60–120° in Figure 2.3 (h)]. $\mathcal{R}_1$ especially is illuminated strongly at certain specific azimuths [see azimuths 270° and 315° in (a)–(f), and 250° in (c), (d), (f), (k)].

The phase slownesses of the two modes are estimated and compared against the simulated dispersion curves [46]. A velocity and density profile is obtained at each of the station locations [47] (sampled every 1 km in depth till 60 km) and averaged to obtain a mean velocity model for Southern California [see Figure 2.5 (b) for the resulting model].

The dominant mode in the slownesses of interest is $\mathcal{R}_0$, and its phase slowness (averaged over the region of study) can be obtained from the beamformer output by averaging across all azimuths and searching for the maximum in a restricted slowness space (here, 0.2–0.4 s/km) as [48]

$$\hat{s}^{(\mathcal{R}_0)} = \underset{s}{\operatorname{argmax}} \langle B(\theta, s) \rangle_\theta \,,\ 0.2 \leq s \leq 0.4,\ f \in [0.05, 0.2] \tag{2.14}$$

The $\mathcal{R}_0$ phase slownesses [medians shown by circles in Figure 2.5 (c)] are very consistent across different months.

Since $\mathcal{R}_1$ is present only in the 0.12–0.2 Hz band, it can be estimated as in (2.14) but by further restricting the slowness space to exclude the fundamental mode:

$$\hat{s}^{(\mathcal{R}_1)} = \underset{s}{\operatorname{argmax}} \langle B(\theta, s) \rangle_\theta \,,\ 0.2 \leq s \leq s_{\max},\ f \in [0.12, 0.2] \tag{2.15}$$

where $s_{\max}$ is either a sufficiently large value (here, 0.27 s/km) or a frequency dependent value such as $s_{\max} = f/3 + 3/14$ (based on the simulated dispersion curve). Both approaches give identical results (squares in Figure 2.5).

The estimated slownesses for both modes agree very well with the predictions. The dispersion of the fundamental and higher modes can be used to estimate the shear wave velocity with depth for the region.

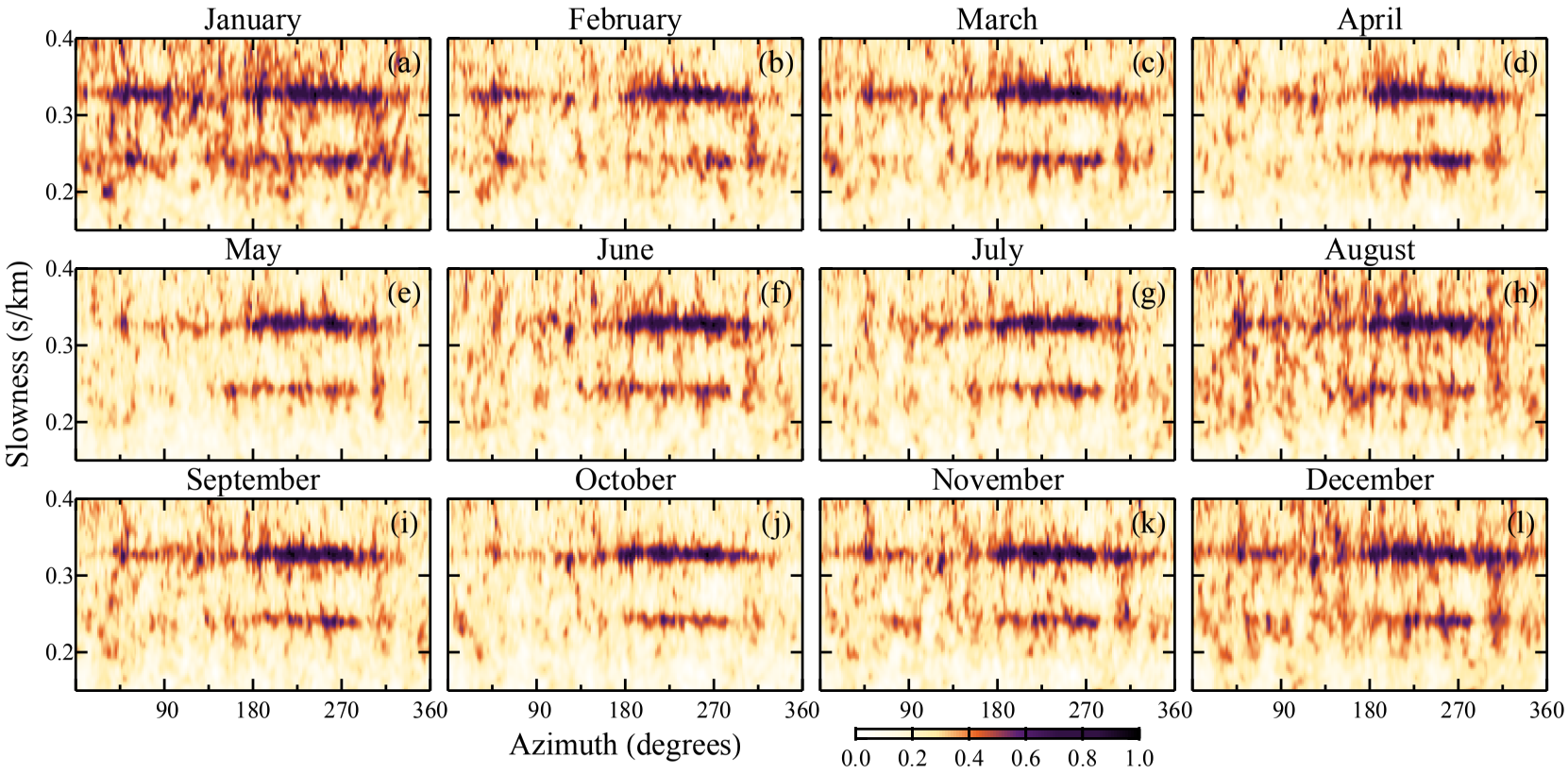

Figure 2.4: Capon beamformer outputs at 0.15 Hz between 0.15–0.4 s/km slowness for all months in 2007 (each subplot is normalized by its maximum). The first mode $\mathcal{R}_1$ of the Rayleigh wave is observed throughout the year, primarily to the west of the array. $\mathcal{R}_1$ also is observed at other azimuths when accompanied by a storm or hurricane activity [between 30–60° in (a) and (b) from storms in the Labrador Sea and the N Atlantic; between 60–120° in (h) from Atlantic hurricanes].

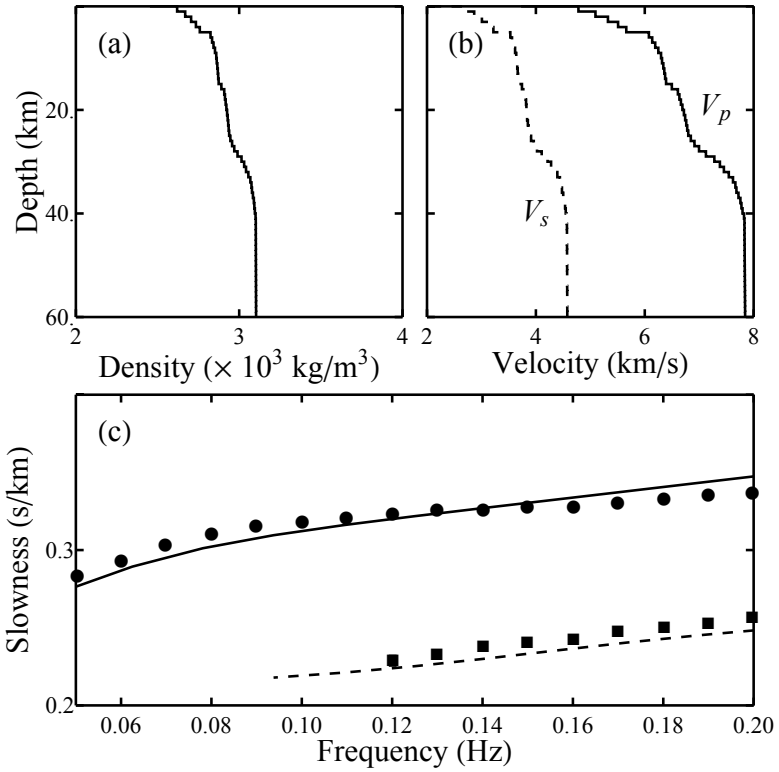

Figure 2.5: Density (a) and compressional and shear velocity (b) profiles for Southern California obtained by averaging the respective quantities at all station locations. (c) Average slowness estimates for $\mathcal{R}_0$ (•), $\mathcal{R}_1$ (■) and their corresponding theoretical curves obtained using the model in (b).

2.5.2 Body Waves from Distant Storms

Propagating energy at low slownesses (below 0.1 s/km), corresponding to body waves, have been known to originate from deep water storms [24, 27, 29]. The body wave energy is strongest above 0.16 Hz [28], but it is seen throughout the DF microseism band [29], and there even have been observations of P waves in the SF microseism band [49], and also is seen in Figure 2.3 (b) below 0.1 s/km.

The body wave arrivals seen in Figure 2.3 (d) and (e) are backprojected assuming a grid of sources and travel time tables [50] corresponding to an assumed propagation path (P, PP, etc.) [29]. The high energy regions in the backprojected maps in Figure 2.6 (P, PP and PKPbc) correspond well with the respective hindcasts. Specifically, note the absence of strong P waves from an 8.0 Mw earthquake in Peru (15 August 2007) in Figure 2.6 (b) and (c) which was removed in the outlier rejection (section 2.3.1), indicating that the energy observed is mostly from storms in the Southern Ocean.

In February, the body waves in the 0.17–0.2 Hz band primarily are from storms in the NW Pacific [Figure 2.6 (d)–(f)] and the P waves from the Atlantic storms seen in the hindcasts are observed at lower frequencies (0.16–0.18 Hz). The storms from the Southern Ocean are observed throughout the frequency band of interest.

2.6 Model for the SCF

As in section 2.5 shows, the ambient seismic noise field in southern Californa contains (in the microseism band) $\mathcal{R}_0$ and $\mathcal{R}_1$ Rayleigh waves (at DF microseism frequencies), and body waves from distant storms. It stands to reason that the estimated ASC will be influenced by these waves, possibly in undesirable ways, and thus must be taken into consideration.

The ASC $\tilde{\Gamma}$ is obtained as in (2.13) with $\Delta_d = 1$ km and $\Delta_\theta = 15°$. To avoid insufficient averaging in each bin, we compute the ASC only for those distance bins that have at least 10 station pairs (i.e., $\#\mathcal{D}_n \geq 10$). For the entire SCSN, this covers the distance bins between approximately 20–380 km and changes depending on the number of stations actually used (see section 2.4). In this section, we explore the spectral (spatial) contents of the observed ASC and show how the phase cancellation effects

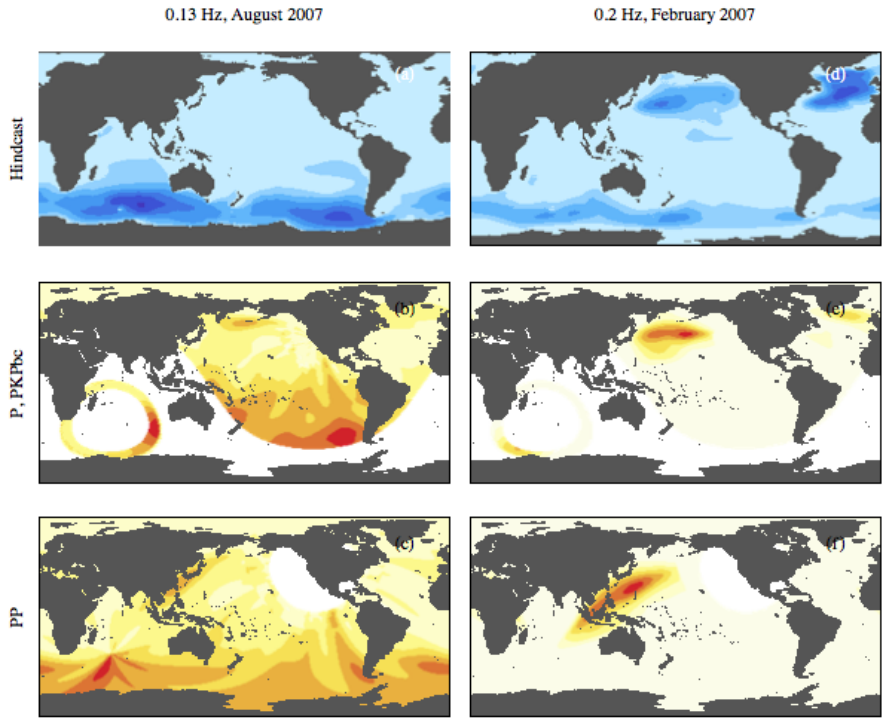

Figure 2.6: Mean ocean wave height for August 2007 (a) and body wave backprojections for the P, PP and PKPbc phases at 0.13 Hz (b) and (c). (d)–(f) same as in (a)–(c), at 0.2 Hz in February. The body wave signals primarily are from storms in the N Pacific and NW Atlantic.

from multiple waves modifies the ASC to be different from the simple order Bessel model.

2.6.1 Spectral Decomposition of the ASC Using the Hankel Transform

Hankel transforms (HT) or Fourier–Bessel transforms are integral transforms where the kernel is a Bessel function. The HT of order zero $\mathcal{H}_0$ of a function $h(x)$, $x > 0$ is given by

$$\mathcal{H}_0(k) = \int_0^\infty h(x) x \mathrm{J}_0(kx)\,\mathrm{d}x \tag{2.16}$$

and the inverse transform is

$$h(x) = \int_0^\infty \mathcal{H}_0(k) k \mathrm{J}_0(kx)\,\mathrm{d}k \tag{2.17}$$

where $k = 2\pi fs$ is the spatial frequency (or wavenumber). Since the ASC from Rayleigh waves is approximately azimuthally isotropic due to the averaging in (2.13), the HT is a natural choice to decompose the ASC. The HT is related to the f–k transform or 2D Fourier transforms that often are used in seismology, and efficient numerical algorithms exist [51] to compute the discrete HT from the observed data.

Figure 2.7 shows the HT (circles) for the ASC at different frequencies and months and the HT for the theoretical isotropic noise SCF (using the estimated slowness for $\mathcal{R}_0$ in section 2.5.1) also is overlaid (see circles in Figure 2.8 for the respective ASCs). The spectrum of the ASC at 0.07 Hz [Figure 2.7 (a)] closely resembles that of the theoretical SCF, whereas the ASCs in the DF microseism band show the presence of $\mathcal{R}_1$ and body waves in addition to $\mathcal{R}_0$ [Figure 2.7 (b)–(d)]. $\mathcal{R}_1$ generally is weaker at the lower end of the DF band [Figure 2.7 (c)] than the upper end [Figure 2.7 (d)]. The peak at about 0.2 s/km slowness in Figure 2.7 (b) possibly is due to a second mode Rayleigh wave [see at azimuths 30° and 210° in Figure 2.4 (j)]. Body waves are seen at slownesses below 0.1 s/km [see "P/PP" and "PKP" in Figure 2.7 (b)–(d)].

The presence of multiple propagation paths at each frequency (even without considering the effects of scattering), suggests that the underlying SCF might be better modeled as a superposition of 2D surface (including higher modes) and 3D body waves

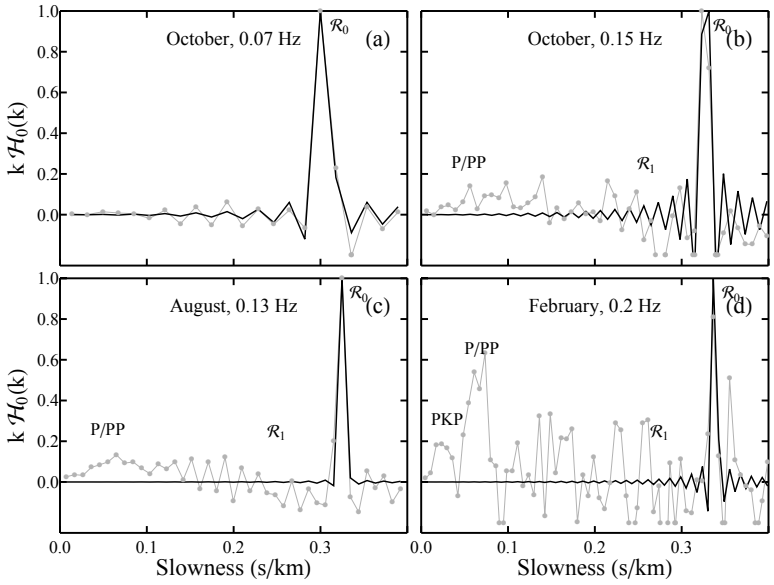

Figure 2.7: HT of the ASC (gray line, circles) showing the contributions from different waves to the spatial spectrum. The HT of $\mathcal{R}_0$ is also shown (black) for comparison. $\mathcal{R}_1$ is seen in the DF microseism band (b)–(d), weaker at the lower end of the band (c) and stronger at the upper end (d). P and PP phases between 0.04–0.1 s/km (b)–(d) and PKP phase between 0.02–0.04 s/km (d).

of different slownesses, rather than only the fundamental mode Rayleigh wave. In other words, the model SCF $\Gamma_{\text{model}}(r)$ is

$$\Gamma_{\text{model}}(r) = \sum_{m \in \mathcal{R}} q_m \, \mathrm{J}_0(2\pi f s^{(m)} r) + \sum_{p \in \mathcal{P}} q_p \, \mathrm{sinc}(2\pi f s^{(p)} r) \tag{2.18}$$

where the $q_{(\cdot)}$ indicates the relative contribution of the component to the SCF, $\mathcal{R}$ denotes the different Rayleigh wave modes (here, $\mathcal{R}_0$ and $\mathcal{R}_1$) and $\mathcal{P}$ denotes the different body wave phases.

2.6.2 Multipath Effects on the ASC

Using the estimates $\hat{s}^{(\mathcal{R}_0)}$ in (2.14) and $\hat{s}^{(\mathcal{R}_1)}$ in (2.15), we estimate the q's and $s^{(p)}$'s in (2.18) from the ASC by the following minimization:

$$\underset{q_{\mathcal{R}_0}, q_{\mathcal{R}_1}, q_{\mathcal{P}_1,\mathcal{P}_2}, s^{(\mathcal{P}_1,\mathcal{P}_2)}}{\operatorname{argmin}} \left\| \tilde{\Gamma}'_n - \sum_{m=\mathcal{R}_0,\mathcal{R}_1} q_m \, \mathrm{J}_0 \left[2\pi f \hat{s}^{(m)} d_n \right] - \sum_{p=\mathcal{P}_1,\mathcal{P}_2} q_p \, \mathrm{sinc} \left[2\pi f s^{(p)} d_n \right] \right\|_1$$

where $s^{(\mathcal{P})}$ is constrained to be between 0 and 0.1 s/km, and the ℓ_1 norm is used to reduce the impact of outliers in the data. The best fit SCF $\widehat{\Gamma}_{\text{true}}$ then is obtained by substituting the estimated quantities in (2.18). We only search for at most two body wave phases (any of P, PP or PKP) since there are usually around 1–2 distinct peaks (with a large spread) in the DF microseism band. The number of $\mathcal{P}$ components can be increased appropriately based on the number of peaks below 0.1 s/km in the corresponding HT.

The best fit SCF thus obtained are shown in Figure 2.8 (thick solid lines; circles with thin lines are the observed ASC) for the same frequencies and months considered in Figure 2.7. The multi-component SCF model in (2.18) captures closely the weak "beating" effects in the ASC [clearly seen in Figure 2.8 (c)] arising due to the interference between the different wavenumbers corresponding to different propgation paths ($\mathcal{R}_0$ and $\mathcal{R}_1$ have the same raypath but propagate at different wavespeeds). While for most purposes a simple $\mathcal{R}_0$ only model might suffice, the results here show that even modest contributions from additional wavenumbers can cause phase cancellation effects, which could influence the estimation of the attenuation.

The contribution from the body waves is shown by the dashed lines which captures the long wavelength fluctuations of the ASC [Figure 2.8 (c)]. The impact of P-wave microseisms is more pronounced on the ASC at higher frequencies, especially in the Winter months (Dec–Feb), when the body waves primarily originate from large storms in the west Pacific and north Atlantic. The resulting ASC [Figure 2.8 (d)] is more sinc-like, than a Bessel (from the estimated $\hat{q}$s, 67% of the SCF is due to body waves).

2.6.3 Composition of the SCF

The composition of the multi-component SCF also varies with season and frequency. From the estimated $\hat{q}$'s, we compute the percentages of $\mathcal{R}_1$, $\mathcal{R}_2$ and $\mathcal{P}$ (combined) and the relationship between the them is studied via a simplex plot (or ternary plot) in Figure 2.9. The plot represents the contributions as observed by the SCSN array using (2.18) for noise in the S Californa region, and will be different for a different array and region. For any point in the simplex plot, the corresponding contribution

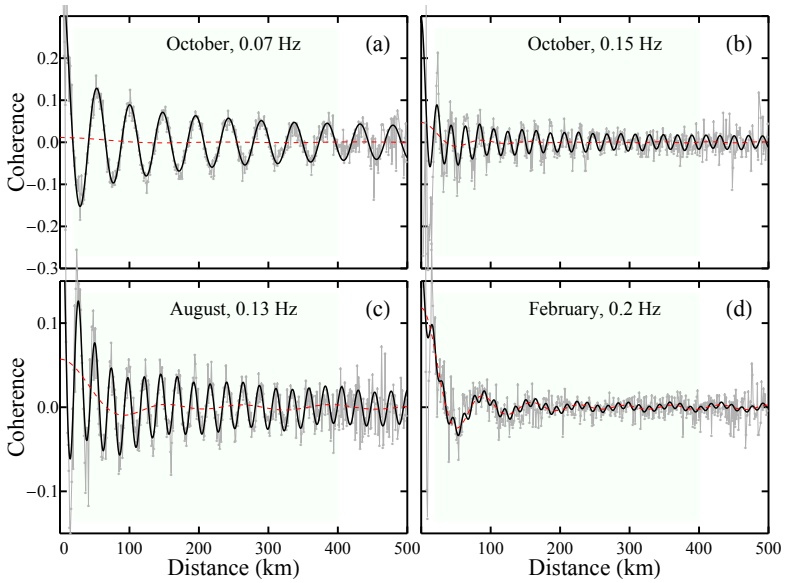

Figure 2.8: Observed ASC (circles, thin gray lines) for different months and frequencies, and the best-fit SCF (solid, black) obtained from (2.19). The fit was computed only between 20–380 km (shaded region) due to insufficient raypaths at shorter and longer distances (see section 2.4). The contribution of the P waves to the SCF is shown by dashed lines. In (d), the SCF primarily is due to P waves, and the fast decay of the coherence could be misinterpreted as being due to attenuation.

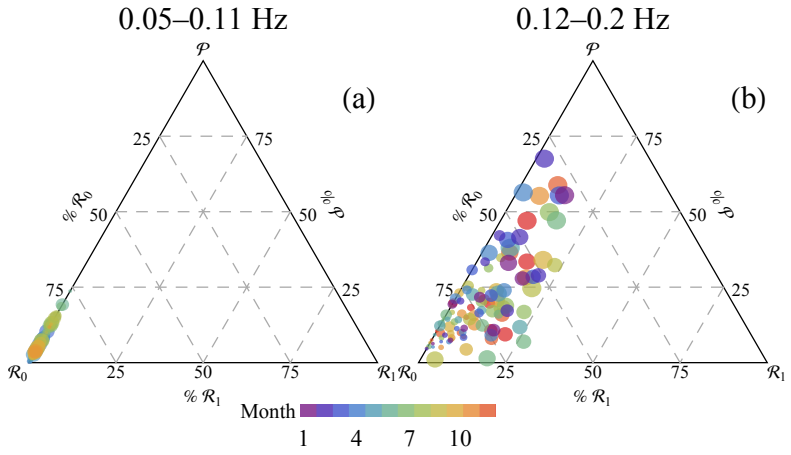

Figure 2.9: Simplex plot showing the relative contributions of $\mathcal{R}_0$, $\mathcal{R}_1$ and P waves to the SCF in the SF microseism band (a) and DF microseism band (b). The values for each component (vertex) at a given point is read from the scale on the corresponding side. In the SF band (a), $\mathcal{R}_1$ is not observed and the SCF is dominated by $\mathcal{R}_0$ with small contributions from P waves. Between 0.12–0.2 Hz [DF band, (b)], the SCF is composed of the $\mathcal{R}_0$, $\mathcal{R}_1$ and P waves (P, PP and PKPbc phases are seen with smaller contributions from other phases). Lower frequencies (smaller circles) have a larger $\mathcal{R}_0$ component in the SCF compared to the higher frequencies. During the winter months (Dec–Feb), the higher frequencies (larger circles) have a larger P component than $\mathcal{R}_1$.

from the three components (vertices) is read from the scale on the corresponding side (using guidelines directly opposite the vertex).

In the SF microseism band, $\mathcal{R}_1$ is not observed and the SCF is dominated by $\mathcal{R}_0$ [see cluster at the $\mathcal{R}_0$ vertex in Figure 2.9 (a)] throughout the year. Modest contributions from body waves are occassionally observed [such as the signals under 0.1 s/km slowness in Figure 2.3 (b)] and these are likely due to P waves generated when distant storms make landfall [29].

In comparison, the contributions are more spread out in the DF band [Figure 2.9 (b)]. At the lower end of the frequency band (smaller circles), the SCF still is predominantly due to Rayleigh waves but shows increasing $\mathcal{R}_1$ contribution with frequency (larger circles towards the $\mathcal{R}_1$ vertex). At the higher end, much of the contribution to the SCF comes from body waves (see larger circles towards the $\mathcal{P}$ vertex). Still, at most months and frequencies, at least 75% of the SCF is due to $\mathcal{R}_0$ (most circles fall within the bottom 25% of the triangle, corresponding to $> 75\%$ $\mathcal{R}_0$).

The colors of the circles also show a seasonal dependence in the relative contributions. During the northern hemisphere Winter (red, blue and purple shades corresponding to Dec–Mar), contribution from body waves is higher at the higher frequencies (large circles close to $\mathcal{P}$) compared to the rest of the year (green and yellow shades). More generally at most frequencies the blue/red shade circles are closer to $\mathcal{P}$ than $\mathcal{R}_0$. At no time or frequency does $\mathcal{R}_1$ exceed $\mathcal{R}_0$, which just reflects the fact that $\mathcal{R}_0$ is the dominant mode.

2.7 Discussion

As discussed in Section 2.4 several extrinsic factors influence the coherence estimate, and the presence of multiple seismic waves (Section 2.5) significantly alters the shape of the SCF (Section 2.6). Although we have minimized the influence of these factors in the processing and explicitly accounted for multiple seismic waves in this article, interpreting the ASC and information derived from it (such as attenuation) also depends on the inhomogenity of the medium.

2.7.1 Effect of Velocity Inhomogenity

Although it is well accepted that azimuthal averaging helps improve the distribution of noise sources (brings it closer to isotropic), its role in mitigating the focusing and defocusing effects of velocity inhomogenity is not fully understood. The station pairs at a particular distance bin also span regions with different velocities. For instance, in the 200–201 km bin [map in Figure 2.1 (d)], nearly half the station pairs fall in the Los Angeles basin area which has higher attenuation and lower velocity than the rest but the estimate of the coherence for that bin includes contributions from both regions [similarly for the 300–301 km bin in Figure 2.1 (e)]. As the distance increases, the number of available station-pairs decreases as well as being predominantly in low attenuation, high velocity regions (even rays crossing through the Los Angeles basin spend only a fraction of the total distance in the basin).

By averaging over a wide region, it is likely that the ASC contains local interference effects (i.e., at certain distance bins) from multiple wavenumbers arising from

inhomogenities. This is evident in Figure 2.8 (a), where the ASC estimates beyond 350 km are progressively shifted slightly to the right (in addition to being noisy, as explained in section 2.4) of the best-fit SCM (which fits the 20–300 km range very well). A shift to the right corresponds to a higher velocity and is due to most of the paths being in a higher velocity region. In regions with high velocity variation, averaging the coherence across different phase slownesses might introduce phase cancellations, which can have the same effect as attenuation (see section 2.6.2).

2.7.2 Challenges in Estimating the Attenuation Coefficient

Theoretical results do not consider the case when the SCF is composed of contributions from different seismic waves (distinct wavenumbers at each frequency). Each wave possibly decays with a different attenuation factor and have different geometric spreading losses, depending on its propagation path. In addition, as shown in section 2.6.2, the interference and phase cancellations from interacting wavenumbers also could have attenuation-like effects. These uncertainties, combined with the effect of scattering which has hitherto been ignored, make estimating attenuation from coherence challenging.

For the ASCs obtained in section 2.6 from (2.13), Figure 2.10 shows the logarithm of the envelopes of the ASC (circles, thin gray lines; computed using the Hilbert transform and smoothed over half a $\mathcal{R}_0$ wavelength) and of the best-fit SCFs (solid). While the ASC shows some signs of attenuation [e.g., see Figure 2.10 (c) beyond 250 km], the exact relationship governing the attenuation is not immediately apparent. For instance, the estimated true SCF has comparable amplitudes similar to the ASC at different, well-separated ranges [compare the ASC (circles) and estimated SCF (solid) at 30–80, 150–220, 310–350 km in Figure 2.10 (b) and 30–70, 120–220 km in (c)], and generally a higher amplitude at ranges in between these [sometimes lower, e.g. at 230 and 450 km in Figure 2.10 (b)].

This could be due to the effects of focusing and defocusing, which was assumed to be negligible due to the distance and azimuth averaging of the ASC, and due to the interference between the different waves (similar patterns in the ASC are also observed in Figure 6 of [15]). However, it is clear that by not accounting for the multiple waves,

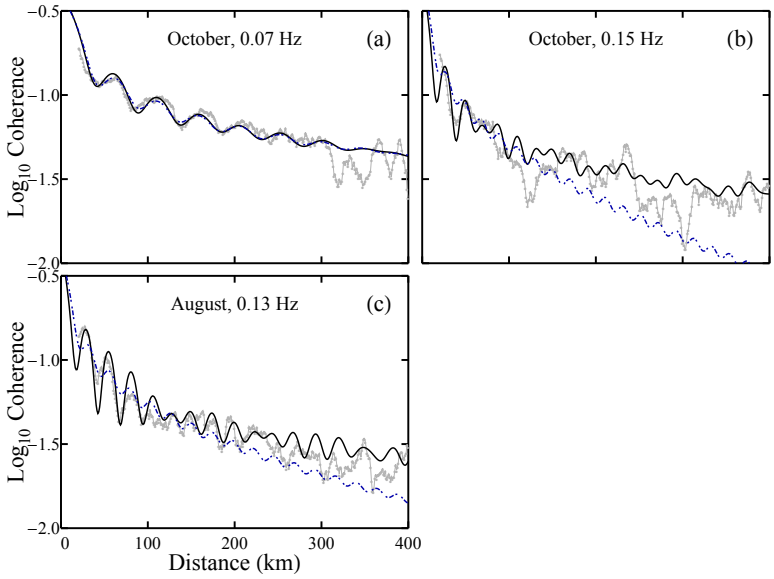

Figure 2.10: Log of the envelope of the observed ASC (circles, thin gray lines), of the best-fit SCF (solid) and of the best fit SCF using an exponentially decaying $\mathcal{R}_0$ as in [15] (dot-dashed).

one might miss the overall trend of the coherence and interpret increases in coherence at farther distances to be just noise. As a result, a simple exponential decay model (dot-dashed, computed using an SCF with only $\mathcal{R}_0$) tends to over estimate the attenuation. Retrieving meaningful estimates of the attenuation coefficient from the ASC would require careful disentangling of the effects of medium anisotropy.

2.8 Conclusions

Our analysis of seismic noise using the Southern California Seismic Network (SCSN) shows a clear presence of fundamental and first mode surface Rayleigh waves and body waves in the microseism band (0.05–0.2 Hz). The higher mode Rayleigh waves are persistent and seen throughout the year primarily from the west. The dispersion curves are estimated for both the modes and they closely resemble the predicted dispersion using velocity models for southern California. These curves will be useful in studying subsurface layering, especially in inversions for shear wave velocities.

Additional factors such as the array geometry and velocity anisotropy affect

the coherence estimates. For random regional arrays such as the SCSN, the number of raypaths with distance is approximately Rayleigh distributed, which gives a rule of thumb for the distances at which there are sufficient raypaths. Within this range, the coherence from data generally is well estimated (approximately 20–380 km for the SCSN) and is noisy elsewhere.

By modeling the underlying spatial coherence function (SCF) as a linear combination of the above wave types (with the ratios estimated from data), we show that it describes the observed coherence better than a simple zeroth order Bessel function model which corresponds to only the fundamental mode. The interactions between the wave types in the SCF leads to beating and phase cancellation effects which could be interpreted as being due to attenuation or the focusing and defocusing effects of velocity anisotropy.

2.9 Acknowledgments

This work was supported by the Office of Naval Research Grants N00014-11-1-0321 and N00014-11-1-0320. Data sources: 1. Seismic data from the Southern California Earthquake Data Center, 2. Metereological data from NOAA 3. Velocity model for Southern California from SCEDC

Chapter 2, in full, is a reprint of the material that is in preparation for submission to the Journal of Geophysical Research.

Bibliography

[1] N. M. Shapiro, M. Campillo, L. Stehly, and M. H. Ritzwoller, "High-resolution surface-wave tomography from ambient seismic noise," *Science*, vol. 307, pp. 1615–1618, 2005.

[2] K. G. Sabra, P. Gerstoft, P. Roux, W. A. Kuperman, and M. C. Fehler, "Extracting time-domain Green's function estimates from ambient seismic noise," *Geophys. Res. Lett*, vol. 32, p. L03310, 2005.

[3] F. C. Lin, M. P. Moschetti, and M. H. Ritzwoller, "Surface wave tomography of the western United States from ambient seismic noise: Rayleigh and Love wave phase velocity maps," *Geophys. J. Int.*, vol. 173, pp. 281–298, 2008.

[4] P. Gouédard, L. Stehly, F. Brenguier, M. Campillo, Y. C. de Verdière, E. Larose, L. Margerin, P. Roux, F. J. Sánchez-Sesma, N. M. Shapiro, and R. L. Weaver, "Cross-correlation of random fields: mathematical approach and applications," *Geophysical Prospecting*, vol. 56, pp. 375–393, 2008.

[5] O. I. Lobkis and R. L. Weaver, "On the emergence of the Green's function in the correlations of a diffuse field," *J. Acoust. Soc. Am.*, vol. 110, pp. 3011–3017, December 2001.

[6] R. L. Weaver and O. I. Lobkis, "Ultrasonics without a source: Thermal fluctuation correlations at MHz frequencies," *Phys. Rev. Lett.*, vol. 87, p. 134301, 2001.

[7] K. Wapenaar, "Retrieving the elastodynamic Green's function of an arbitrary inhomogeneous medium by cross-correlation," *Phys. Rev. Lett.*, vol. 93, p. 254301, 2004.

[8] R. Snieder, "Extracting the Green's function from the correlation of coda waves: A derivation based on stationary phase," *Phy. Rev. E.*, vol. 69, p. 046610, 2004.

[9] P. Roux, W. A. Kuperman, and the NPAL group, "Extracting coherent wave fronts from acoustic ambient noise in the ocean," *J. Acoust. Soc. Am.*, vol. 116, pp. 1995–2003, 2004.

[10] E. Larose, A. Derode, M. Campillo, and M. Fink, "Imaging from one-bit correlations of wideband diffuse wave fields," *J. Appl. Phys.*, vol. 95, pp. 8393–8399, 2004.

[11] P. Gerstoft, K. G. Sabra, P. Roux, W. A. Kuperman, and M. C. Fehler, "Green's functions extraction and surface-wave tomography from microseisms in southern California," *Geophysics*, vol. 71, pp. SI23–SI31, 2006.

[12] L. A. Brooks and P. Gerstoft, "Green's function approximation from cross-correlations of 20–100 Hz noise during a tropical storm," *J. Acoust. Soc. Am.*, vol. 125, pp. 723–734, Jan 2009.

[13] S. E. Fried, W. A. Kuperman, K. G. Sabra, and P. Roux, "Extracting the local Green's function on a horizontal array from ambient ocean noise," *J. Acoust. Soc. Am.*, vol. 124, pp. EL183–EL188, 2008.

[14] G. A. Prieto and G. C. Beroza, "Earthquake ground motion prediction using the ambient seismic field," *Geophys. Res. Lett.*, vol. 35, p. L14304, 2008.

[15] G. A. Prieto, J. F. Lawrence, and G. C. Beroza, "Anelastic Earth structure from the coherency of the ambient seismic noise field," *J. Geophys. Res.*, vol. 114, p. B07303, 2009.

[16] J. F. Lawrence and G. A. Prieto, "Attenuation tomography of the western United States from ambient noise," *J. Geophys. Res.*, vol. 116, p. B06302, 2011.

[17] G. A. Prieto, M. Denolle, J. F. Lawrence, and G. C. Beroza, "On amplitude information carried by the ambient seismic field," *C. R. Geoscience*, vol. 343, no. 8, pp. 600–614, 2011.

[18] J. Zhang and X. Yang, "Extracting surface wave attenuation from seismic noise using correlation of the coda of correlation," *J. Geophys. Res.*, vol. 118, no. 5, pp. 2191–2205, 2013.

[19] V. C. Tsai, "On establishing the accuracy of noise tomography travel-time measurements in a realistic medium," *Geophys. J. Int.*, vol. 178, pp. 1555–1564, 2009.

[20] R. L. Weaver, "On the amplitudes of correlations and the inference of attenuations, specific intensities and site factors from ambient noise," *C. R. Geoscience*, vol. 343, pp. 615–622, 2011.

[21] P. Cupillard and Y. Capdeville, "On the amplitude of surface waves obtained by noise correlation and the capability to recover the attenuation: a numerical approach," *Geophys. J. Int.*, vol. 181, pp. 1687–1700, 2010.

[22] N. Harmon, C. Rychert, and P. Gerstoft, "Distribution of noise sources for seismic interferometry," *Geophys. J. Int.*, vol. 183, pp. 1470–1484, 2010.

[23] V. C. Tsai, "Understanding the amplitudes of noise correlation measurements," *J. Geophys. Res.*, vol. 116, p. B09311, 2011.

[24] R. A. Haubrich and K. McCamy, "Microseisms: Coastal and pelagic sources," *Rev. Geophys.*, vol. 7, no. 3, pp. 539–571, 1969.

[25] L. A. Brooks, J. Townend, P. Gerstoft, S. Bannister, and L. Carter, "Fundamental and higher-mode Rayleigh wave characteristics of ambient seismic noise in New Zealand," *Geophys. Res. Lett.*, vol. 36, p. L23303, 2009.

[26] N. Harmon, D. Forsyth, and S. Webb, "Using Ambient Seismic Noise to Determine Short-Period Phase Velocities and Shallow Shear Velocities in Young Oceanic Lithosphere," *Bull. Seis. Soc. Am.*, vol. 97, no. 6, pp. 2009–2023, 2007.

[27] P. Gerstoft, M. C. Fehler, and K. G. Sabra, "When Katrina hit California," *Geophys. Res. Lett.*, vol. 33, pp. 1–6, Jan 2006.

[28] J. Zhang, P. Gerstoft, and P. D. Bromirski, "Pelagic and coastal sources of p-wave microseisms: Generation under tropical cyclones," *Geophys. Res. Lett.*, vol. 37, no. 15, p. L15301, 2010.

[29] P. Gerstoft, P. M. Shearer, N. Harmon, and J. Zhang, "Global P, PP, and PKP wave microseisms observed from distant storms," *Geophys. Res. Lett.*, vol. 35, p. L23306, 2008.

[30] M. Landès, F. Hubans, N. M. Shapiro, A. Paul, and M. Campillo, "Origin of deep ocean microseisms by using teleseismic body waves," *J. Geophys. Res.*, vol. 115, no. B5, 2010.

[31] H. Cox, "Spatial correlation in arbitrary noise fields with application to ambient sea noise," *J. Acoust. Soc. Am.*, vol. 54, no. 5, pp. 1289–1301, 1973.

[32] K. Aki, "Space and time spectra of stationary stochastic waves, with special reference to microtremors," *Bull. Earthquake Res. Inst. Univ. Tokyo*, vol. 35, pp. 415–457, 1957.

[33] C. H. Eckart, "The theory of noise in continuous media," *J. Acoust. Soc. Am.*, vol. 25, no. 2, pp. 195–199, 1953.

[34] W. S. Liggett Jr. and M. J. Jacobson, "Covariance of noise in attenuating media," *J. Acoust. Soc. Am.*, vol. 36, no. 6, pp. 1183–1194, 1964.

[35] H. Nakahara, "Formulation of the spatial autocorrelation (SPAC) method in dissipative media," *Geophys. J. Int.*, vol. 190, pp. 1777–1783, 2012.

[36] S. C. Walker, "A model for spatial coherence from directive ambient noise in attenuating, dispersive media," *J. Acoust. Soc. Am.*, vol. 132, no. 1, pp. EL15–EL21, 2012.

[37] X. Liu and Y. Ben-Zion, "Theoretical and numerical results on effects of attenuation on correlation functions of ambient seismic noise," *Geophys. J. Int.*, 2013.

[38] M. W. Asten, "On bias and noise in passive seismic data from finite circular array data processed using SPAC methods," *Geophysics*, vol. 71, no. 6, pp. V153–V162, 2006.

[39] P. J. Huber, *Robust Statistics*. Wiley, New York, 1981.

[40] G. D. Bensen, M. H. Ritzwoller, M. P. Barmin, A. L. Levshin, F. Lin, M. P. Moschetti, N. M. Shapiro, and Y. Yang, "Processing seismic ambient noise data to obtain reliable broad-band surface wave dispersion measurements," *Geophys. J. Int.*, vol. 169, pp. 1239–1260, 2007.

[41] J. Capon, "High-resolution frequency-wavenumber spectrum analysis," *Proceedings of the IEEE*, vol. 57, no. 8, pp. 1408–1418, 1969.

[42] H. L. van Trees, *Detection, Estimation, and Modulation Theory Part IV: Optimum Array Processing*. New York: Wiley, 2002.

[43] B. J. Mitchell, "Anelastic structure and evolution of the continental crust and upper mantle from seismic surface wave attenuation," *Rev. Geophys.*, vol. 33, no. 4, pp. 441–462, 1995.

[44] P. Gerstoft and T. Tanimoto, "A year of microseisms in southern California," *Geophys. Res. Lett.*, vol. 34, p. L20304, 2007.

[45] K. Nishida, H. Kawakatsu, Y. Fukao, and K. Obara, "Background Love and Rayleigh waves simultaneously generated at the Pacific Ocean floors," *Geophys. Res. Lett.*, vol. 35, p. L16307, 2008.

[46] R. B. Hermann, "Computer Programs in Seismology, version 3.30," *Saint Louis University*, 2010.

[47] M. Kohler, H. Magistrale, and R. Clayton, "Mantle heterogeneities and the SCEC three-dimensional seismic velocity model version 3," *Bull. Seis. Soc. Am.*, vol. 93, pp. 757–774, 2003.

[48] N. Harmon, P. Gerstoft, C. A. Rychert, and G. A. Abers, "Phase velocities from seismic noise using beamforming and cross correlation in Costa Rica and Nicaragua," *Geophys. Res. Lett.*, vol. 35, p. L19303, 2008.

[49] L. Stehly, M. Campillo, and N. Shapiro, "A study of the seismic noise from its long-range correlation properties," *J. Geophys. Res.*, vol. 111, no. B10, 2006.

[50] B. Kennett, E. Engdahl, and R. Buland, "Constraints on seismic velocities in the earth from traveltimes," *Geophys. J. Int.*, vol. 122, no. 1, pp. 108–124, 1995.

[51] M. Guizar-Sicairos and J. C. Gutiérrez-Vega, "Computation of quasi-discrete hankel transforms of integer order for propagating optical wave fields," *J. Opt. Soc. Am. A*, vol. 21, no. 1, pp. 53–58, 2004.

3

ASYMPTOTIC EIGENVALUE DENSITY OF NOISE COVARIANCE MATRICES

The asymptotic eigenvalues are derived for the true noise covariance matrix (CM) and the noise sample covariance matrix (SCM) for a line array with equidistant sensors in an isotropic noise field. In this case, the CM in the frequency domain is a symmetric Toeplitz sinc matrix which has at most two distinct eigenvalues in the asymptotic limit of an infinite number of sensors. Interestingly, for line arrays with inter-element spacing less than half a wavelength, the CM turns out to be rank deficient. The asymptotic eigenvalue density of the SCM is derived using random matrix theory (RMT) for all ratios of the inter-element spacing to the wavelength. When the CM has two distinct eigenvalues, the eigenvalue density of the SCM separates into two distinct lobes as the number of snapshots is increased. These lobes are centered at the two distinct eigenvalues of the CM. The asymptotic results agree well with analytic solutions and simulations for arrays with a small number of sensors.

3.1 Introduction

Over the past decade, it has been shown that cross-correlations of a diffuse field between a pair of receivers yields the Green's function between them [1,2]. Since

ambient noise is ubiquitous, the immense potential of this technique to image remote areas of the ocean and the interior of the earth using arrays of sensors and naturally occurring noise has made it a rich area of current research in seismology [3, 4] and ocean acoustics [5, 6], and structural engineering [7] among others. The use of many receivers and the random nature of the ambient noise field provides a good setting for the application of random matrix theory (RMT) [8, 9]. Here, we study the eigenvalues of noise covariance matrices from an array of sensors.

In array processing problems, the noise field often is assumed to be *isotropic*, i.e., it consists of random waves propagating towards the array from all directions. The spatial coherence function Γ of the noise recorded on two sensors in a 3-D isotropic noise field is [10]

$$\Gamma = \mathrm{sinc}(2\beta) \tag{3.1}$$

where $\mathrm{sinc}(x) = \sin(\pi x)/(\pi x)$ and β is the ratio of the spacing between the sensors to the wavelength under consideration ($\beta = f\Delta x/c$, where f is the frequency, Δx is the spacing between the sensors, and c is the speed of wave propagation in the medium). For a linear array of N equidistant sensors, the elements of the covariance matrix Σ (CM) of the noise field (normalized to unit power on each sensor) are given by

$$\Sigma_{ij} = \mathrm{sinc}\left(2\beta|i-j|\right), \tag{3.2}$$

which is a symmetric Toeplitz matrix. Thus, the spatial correlations are only dependent on β and the separation $|i-j|$.

With real noise data, the sample covariance matrix (SCM) $\widehat{\Sigma}$ is estimated from M i.i.d. observations of the array snapshot vector (*i.e.*, the Fourier coefficients of the observation vector at a particular frequency) $\psi_m,\ m = \{1, \ldots, M\}$ as

$$\widehat{\Sigma} = \frac{1}{M}\sum_{m=1}^{M} \psi_m \psi_m^H. \tag{3.3}$$

The eigenvalues of the SCM deviate from the true CM and the density of these eigenvalues,

$$\widehat{\mathrm{p}}(\lambda) = \frac{1}{N}\sum_{n=1}^{N} \delta(\lambda - \lambda_n) \tag{3.4}$$

where λ_n are the eigenvalues of $\widehat{\Sigma}$, are typically studied using random matrix theory (RMT), in the asymptotic limit as the array dimension and the observation dimension both grow large proportionately, i.e., $N, M \to \infty,\ N/M = \nu$, the ratio of the number of array elements to the number of snapshots. RMT also has applications in a wide variety of fields such as signal detection [11], communication via antennas [12], information theory and wireless networks [13], elastodynamics [14] and wave propagation and scattering in random media [15–17].

Prior work involving RMT and eigenvalue densities relevant to this article include [18, 19]. While [18] deals with estimating the true eigenvalues of the CM from the observed SCM for a few distinct sources, we focus on the asymptotic eigenvalue density of the SCM for a noise only model (i.e., no sources). Knowledge of these densities could be used in monitoring environments, i.e., a change in the density could be interpreted as a change in the environmental conditions. The results also could be used in conjunction with [19] to identify eigenvalues corresponding to strong interferers in the environment (e.g., ships in ocean acoustics and earthquakes in seismology). In Section 3.3.2, it is shown that the SCM for isotropic noise fields is rank deficient even when the number of snapshots is more than the number of array elements (i.e., $\nu \leq 1$). This result is certainly important to consider in applications which require the inverse of the SCM, such as adaptive beamforming.

The rest of the paper is organized as follows. A statistical model for the SCM is chosen in Section 3.1.1, followed by a recap of known results for an uncorrelated noise SCM. Section 3.1.3 discusses preliminary details that aid in the derivation of the eigenvalues in Section 3.2. In Section 3.3, the asymptotic eigenvalue density of the SCM is derived using Stieltjes transforms and studied in detail for all values of β. The asymptotic results are compared with analytical results for finite N in Section 3.4 and using simulations for practical values of N in Section 3.5, followed by conclusions in Section 3.6.

3.1.1 Statistical Model for the SCM

The noise snapshot vector is modeled as a stationary, zero-mean, complex Gaussian stochastic process with covariance Σ, i.e., $\psi_m \sim \mathcal{CN}(0, \Sigma)$. Realizations of

the noise SCM then can be generated from the true CM Σ as [18]

$$\widehat{\Sigma} = \frac{1}{M}\Sigma^{1/2}\mathbf{X}\left(\Sigma^{1/2}\mathbf{X}\right)^{H}, \tag{3.5}$$

where $\mathbf{X}$ is an $N \times M$ random matrix belonging to the Gaussian unitary ensemble (GUE)[1] whose entries are zero-mean complex Gaussian random variables drawn from $\mathcal{CN}(0,1)$, and $\Sigma^{1/2}$ is a non-negative definite square root of the true CM, Σ.

Here we restrict our focus to $\nu \leq 1$, i.e., there are at least as many snapshots as the number of array elements, because the stationarity of the environment over reasonable intervals allows for sufficient averaging (i.e., snapshot starved scenarios are not considered).

3.1.2 Uncorrelated Noise at $\beta = 1/2$

At $\beta = 1/2$ (half-wavelength spacing) the off-diagonal terms in (3.2) are zero and $\Sigma = \mathbf{I}$. In other words, the noise is spatially uncorrelated from sensor to sensor.

The eigenvalue density of the SCM in this case, in the limit $N, M \to \infty$ and $N/M = \nu$, is given by the Marčenko–Pastur (MP) density [20],

$$\widehat{\mathrm{p}}_{MP}(\lambda) = \begin{cases} \frac{\sqrt{(l_+ - \lambda)(\lambda - l_-)}}{2\pi\nu\lambda} & l_- < \lambda < l_+ \\ 0 & \text{otherwise} \end{cases} \tag{3.6}$$

where $l_- = (1 - \sqrt{\nu})^2$ and $l_+ = (1 + \sqrt{\nu})^2$ are the upper and lower limits of the "spreading" of the eigenvalues of the SCM around the true eigenvalue which is 1.

This holds true for multiples of the half wavelength spacing i.e., $\beta = q/2,\ q \in \mathbb{N}$ and for all other values of β, the noise is correlated and the densities of the SCM will deviate from the simple MP density.

3.1.3 Preliminaries

Symmetric sinc Toeplitz matrices (henceforth referred to as sinc matrices) also arise in solutions to certain differential equations [21], covariance matrix tapering [22, 23], etc. In general, the eigenvalues of an infinite dimensional Toeplitz

[1] The distribution of the elements in a GUE random matrix is invariant to transformations by a unitary matrix

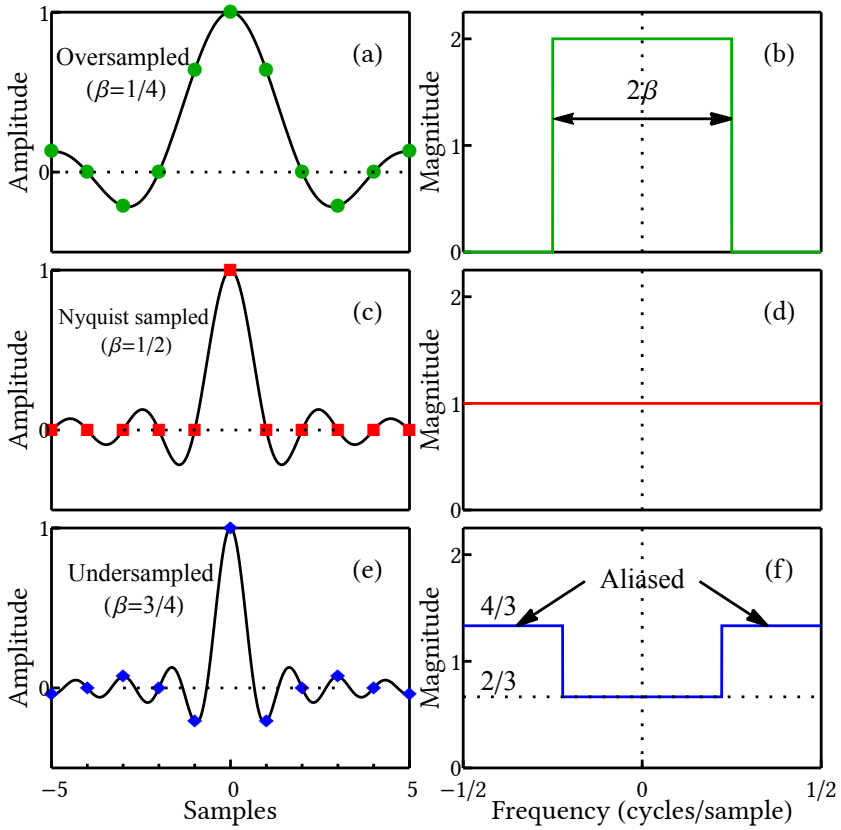

Figure 3.1: Schematic showing the sinc function and its Fourier transform when β is (a,b) less than the Nyquist frequency (c,d) at the Nyquist frequency, i.e. $\beta = 1/2$ and (e,f) greater than the Nyquist frequency.

matrix constructed from absolutely summable sequences with an absolutely summable Fourier series (called Wiener class Toeplitz matrices) are related to the Fourier series of the sequence [24, 25]. Although the underlying sinc sequence in Σ is not absolutely summable, this result still holds, as shown in Section 3.2.

The relation between the Fourier transform of the sinc function and the eigenvalues of the sinc matrix has been shown previously [26, 27]. The eigenvalues of the finite dimensional sinc matrix also were studied in detail in the context of discrete prolate spheroidal wave functions [21, 27] for $\beta \leq 1/2$ and for block Toeplitz sinc matrices in the context of asynchronous CDMA systems [28]. In Section 3.2, we consider the asymptotic eigenvalues of the true CM Σ for all $\beta \in (0, \infty)$, as the array dimension $N \to \infty$.

A key to understanding the asymptotic behavior of the eigenvalues is the behavior of the Fourier transform of the sampled sinc function when it is oversampled or undersampled (see Fig. 3.1). Consider the infinite sequence $\mathrm{sinc}(2\beta n)$ where $n \in \mathbb{Z}$, i.e., a sampling interval of Δx corresponding to the inter-element spacing of the line array. The Fourier transform of the continuous sinc function is a rectangular function of bandwidth 2β (highest frequency β). In order to avoid aliasing in the Fourier transform of the sampled sinc, we need $2\beta \leq 1$, or $\beta \leq 1/2$. At the Nyquist sampling $\beta = 1/2$ (and at multiples of $1/2$), the sinc is sampled at only its peak and zeros, and corresponds to a unit sample. As a result, the Fourier transform is 1 [see Fig. 3.1(c,d)]. When $\beta < 1/2$, it is oversampled and the Fourier transform is zero outside the bandwidth of the sinc [see Fig. 3.1(a,b)]. When $\beta > 1/2$, the sinc function is undersampled and this introduces aliasing in the Fourier space [see Fig. 3.1(e,f)]. These behaviors of the Fourier transform are reflected in the eigenvalues of the CM.

3.1.4 Notations

Throughout this paper, matrices are represented by bold, uppercase symbols and vectors by bold, lowercase symbols. With the exception of ν, quantities pertaining to the SCM are denoted with a carat, $\hat{}$. In order to compare infinite dimensional

matrices, a normalized rank is defined as

$$\mathcal{R}(\cdot) = \lim_{N\to\infty} \frac{\text{rank}(\cdot)}{N} \tag{3.7}$$

For convenience, N is implicitly assumed even in Section 3.2.1, although the same can be done for odd N (asymptotic result remains unchanged).

3.2 Asymptotic Eigenvalues of the Noise CM

3.2.1 Derivation of the Eigenvalues

Let $f_n = \text{sinc}(2\beta n),\ n \in \mathbb{Z}$ be an even sequence that is absolutely square summable, with a Fourier transform

$$\varphi(\kappa) = \sum_{n=-\infty}^{\infty} f_n e^{-\imath 2\pi\kappa n} \tag{3.8}$$

where κ is the spatial frequency.

Proposition 3.1 (Asymptotic eigenvalues of the sinc matrix Σ). *Defining λ_k and $\mathbf{u}_k$ as*

$$\lambda_k = \sum_{n=-N/2}^{N/2-1} f_n e^{-\imath 2\pi nk/N} \tag{3.9}$$

and

$$\mathbf{u}_k = \frac{1}{\sqrt{N}} \left[1, e^{-\imath 2\pi k/N}, \ldots, e^{-\imath 2\pi k(N-1)/N}\right]^T \tag{3.10}$$

where $k \in \{-N/2, \ldots, N/2-1\}$ is the equivalent of a discrete Fourier transform spatial frequency bin, then as $N \to \infty$, λ_k and $\mathbf{u}_k$ are the eigenvalues and eigenvectors of Σ.

Proof. If λ_k and $\mathbf{u}_k$ are the eigenvalues and eigenvectors of Σ, then the equation

$$\Sigma\mathbf{u}_k = \lambda_k\mathbf{u}_k \tag{3.11}$$

must hold as $N \to \infty$. Writing Σ as

$$\Sigma = \begin{bmatrix} f_0 & f_1 & \cdots & f_{N-1} \\ f_{-1} & f_0 & \cdots & f_{N-2} \\ \vdots & \vdots & \ddots & \vdots \\ f_{-N+1} & f_{-N+2} & \cdots & f_0 \end{bmatrix}, \tag{3.12}$$

the jth element ($j = 1, \ldots, N$) of the vector $\Sigma \mathbf{u}_k$ is

$$\begin{aligned}\left[\Sigma \mathbf{u}_k\right]_j &= \frac{1}{\sqrt{N}} \sum_{n=1-j}^{N-j} f_n e^{-\imath 2\pi k(n+j-1)/N} \\ &= \frac{1}{\sqrt{N}} \sum_{n=1-j}^{N-j} \alpha_{jkn},\end{aligned} \tag{3.13}$$

where $\alpha_{jkn} = f_n e^{-\imath 2\pi k(n+j-1)/N}$ is introduced as a shorthand notation. Similarly, the jth element of the vector $\lambda_k \mathbf{u}_k$ is

$$\left[\lambda_k \mathbf{u}_k\right]_j = \frac{1}{\sqrt{N}} \sum_{n=-N/2}^{N/2-1} \alpha_{jkn} \tag{3.14}$$

Subtracting (3.13) from (3.14):

$$\left[\Sigma \mathbf{u}_k - \lambda_k \mathbf{u}_k\right]_j = \frac{1}{\sqrt{N}} \begin{cases} -\displaystyle\sum_{n=-N/2}^{-j} \alpha_{jkn} + \sum_{n=N/2}^{N-j} \alpha_{jkn} & j \leq N/2 \\ \displaystyle\sum_{n=1-j}^{-N/2-1} \alpha_{jkn} - \sum_{n=N-j+1}^{N/2-1} \alpha_{jkn} & j > N/2 \end{cases} \tag{3.15}$$

Using the triangle inequality and reverting to the original notation, (3.15) results in

$$\left|\left[\Sigma \mathbf{u}_k - \lambda_k \mathbf{u}_k\right]_j\right|^2 \leq \frac{1}{N} \begin{cases} \displaystyle\sum_{n=-N/2}^{-j} |f_n|^2 + \sum_{n=N/2}^{N-j} |f_n|^2 & j \leq N/2 \\ \displaystyle\sum_{n=1-j}^{-N/2-1} |f_n|^2 - \sum_{n=N-j+1}^{N/2-1} |f_n|^2 & j > N/2 \end{cases} \tag{3.16}$$

Taking the norm of the entire vector, and combining the terms in the first and last components, the terms in the second and penultimate components and so forth, we get

$$\begin{aligned}\left\|\Sigma \mathbf{u}_k - \lambda_k \mathbf{u}_k\right\|_2^2 \leq & \frac{1}{N} \sum_{j=1}^{N/2} \left(\sum_{n=-N+j}^{-j} |f_n|^2 + \sum_{j}^{N-j} |f_n|^2 \right) \\ \leq & \frac{2}{N} \sum_{j=1}^{N/2} \sum_{n=j}^{N-j} |f_n|^2 = \frac{2}{N} \sum_{j=1}^{N/2} \sum_{n=j}^{N-j} \operatorname{sinc}^2(2\beta n) \\ \leq & \frac{1}{2\beta^2 N} \sum_{j=1}^{N/2} \sum_{n=j}^{\infty} \frac{1}{n^2}\end{aligned} \tag{3.17}$$

Since the functions $1/x^2$ (and $1/x$) are strictly convex on $(0, \infty)$, the RHS of (3.17) can be simplified as:

$$\sum_{j=1}^{N/2} \sum_{n=j}^{\infty} \frac{1}{n^2} < \sum_{j=1}^{N/2} \int_{j-1/2}^{\infty} \frac{dx}{x^2} < \sum_{j=1}^{N/2} \frac{1}{j-1/2} < \int_{1/2+\varepsilon}^{N/2+1/2} \frac{dy}{y-1/2} = \ln\left(\frac{N}{2\varepsilon}\right) \tag{3.18}$$

From (3.17) and (3.18), $\exists\ \varepsilon > 0$ independent of N, such that $\ln(\frac{N}{2\varepsilon})/(2\beta^2 N)$ goes to zero independent of k as $N \to \infty$. Hence,

$$\|\Sigma \mathbf{u}_k - \lambda_k \mathbf{u}_k\|_2 \to 0 \text{ as } N \to \infty\ \forall\ k \tag{3.19}$$

or λ_k and $\mathbf{u}_k$ are the eigenvalues and eigenvectors of Σ respectively. □

When $N \to \infty$, from (3.9) and (3.8), $\lambda_k = \varphi(k/N)$ i.e., $\varphi(\kappa)$ sampled uniformly at N points in $[-1/2, 1/2)$. As illustrated in Fig. 3.1, $\varphi(\kappa)$ only takes on one or two distinct values. Thus, the eigenvalue density $\mathrm{p}(\lambda)$ of Σ can be written succinctly as

$$\mathrm{p}(\lambda) = \xi_1 \delta(\lambda - \Lambda_1) + \xi_2 \delta(\lambda - \Lambda_2), \tag{3.20}$$

where $\Lambda_{1,2}$ are the two distinct eigenvalues and $\xi_{1,2}$ are their multiplicity ratios defined as follows:

1. For $\beta < 1/2$ (oversampling)

$$\varphi(\kappa) = \frac{1}{2\beta} \operatorname{rect}\left(\frac{\kappa}{2\beta}\right), \tag{3.21}$$

where $\operatorname{rect}(x) = 1\ \forall\ |x| \leq 1/2$ and 0 elsewhere. Hence, the two distinct values of λ_k are

$$\Lambda_1 = \frac{1}{2\beta} \text{ and } \Lambda_2 = 0 \tag{3.22}$$

and the multiplicity ratios are related to the bandwidth as

$$\xi_1 = 2\beta \text{ and } \xi_2 = 1 - 2\beta. \tag{3.23}$$

In this case, Σ is rank deficient due to the zero eigenvalues.

2. For $\beta = 1/2$ (Nyquist sampling) and multiples thereof, $\Lambda_1 = \Lambda_2 = 1$ and $\Sigma = \mathbf{I}$.

3. For $\beta > 1/2$ (undersampling) and not a multiple of $1/2$, aliasing is introduced due to the folding of the eigenvalue spectrum onto itself [see Fig. 3.2(b)]. As a result, both Λ_1 and Λ_2 are non-zero when $\beta > 1/2$ and $\beta \neq q/2,\ q \in \mathbb{N}$, resulting in Σ being full rank. $\Lambda_{1,2}$ then can be written as

$$\Lambda_1 = \frac{q+1}{2\beta} \text{ and } \Lambda_2 = \frac{q}{2\beta}, \tag{3.24}$$

with q such that $q < 2\beta \leq q+1$. The term $q/(2\beta)$ accounts for the folding of the spectrum. Similarly, the multiplicity ratios are given by

$$\xi_1 = 2\beta - q \text{ and } \xi_2 = q + 1 - 2\beta. \tag{3.25}$$

3.2.2 Physical Interpretation and Effects of Finite Arrays

For $\beta \leq 1/2$, the eigenvectors (3.10) of the non-zero eigenvalues correspond to waves from specific angles θ_κ impinging on the array

$$\theta_\kappa = \arcsin\left(\frac{\kappa}{\beta}\right). \tag{3.26}$$

Thus $\theta_0 = 0$ corresponds to a wave impinging at broadside and $\theta_{\pm\beta} = \pm\pi/2$ corresponds to the array end-fire direction (see Fig. 3.2). The zero eigenvalues Λ_2 for $\beta < 1/2$ correspond to the invisible space [29, §3.3.2], as it does not correspond to any propagating wave [see Fig. 3.2(b)].

For finite N the transition between Λ_1 and Λ_2 becomes more gradual due to truncation effects similar to the effect observed for finite Fourier transforms and this is discussed in Section 3.5. Approximations for the eigenvalues in the transition region for finite N are described in [21], scaled down by a factor of 2β.

3.3 Asymptotic Eigenvalue Density of the Noise SCM Using Random Matrix Theory

For the statistical assumptions made in (3.5), the eigenvalue density $\widehat{\mathrm{p}}(\lambda)$ of $\widehat{\Sigma}$ converges to a probability density function that is related to the true eigenvalue spectral density $\mathrm{p}(\lambda)$ of Σ [30].

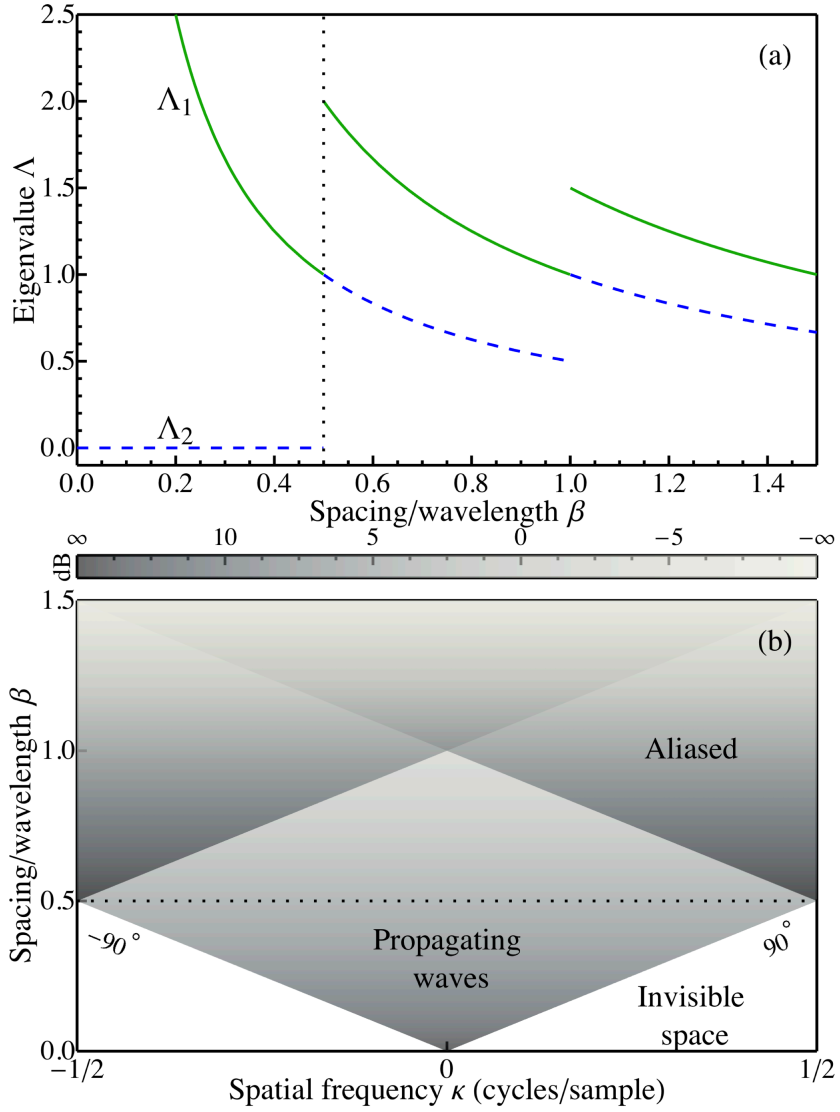

Figure 3.2: (a) Distinct eigenvalues Λ_1 (solid) and Λ_2 (dashed) of Σ versus β, the ratio of spacing to wavelength. The dotted line marks $\beta = 1/2$ the half-wavelength spacing. (b) Change in eigenvalues versus spatial frequency and β. The invisible space and aliased regions also are marked.

The behavior of the eigenvalues of the SCM in the asymptotic limit, is characterized by the Stieltjes transform of its distribution [31]. In this section, we present the relevant results from RMT in Section 3.3.1, followed by the derivation for the densities for all β in Sections 3.3.2–3.3.4.

3.3.1 Background

For the density $\widehat{\mathrm{p}}(\lambda) : \mathbb{R} \to \mathbb{R}$, its Stieltjes transform $\hat{s} = \hat{s}(z)$ is a complex valued function defined as

$$\hat{s}(z) = \int_{-\infty}^{\infty} \frac{\widehat{\mathrm{p}}(\lambda)}{\lambda - z}\, d\lambda,\ z \in \mathbb{C}^{+} = \{z \in \mathbb{C} \mid \mathrm{Im}[z] > 0\} \tag{3.27}$$

Equation (3.27) can be inverted explicitly to retrieve the density as [13]

$$\widehat{\mathrm{p}}(\lambda) = \lim_{\varepsilon \to 0^{+}} \frac{1}{\pi} \mathrm{Im}\left[\hat{s}(\lambda + \imath\varepsilon)\right] \tag{3.28}$$

Since for all $\beta \in (0, \infty)$, Σ is bounded in spectral norm and the observations follow Gaussian statistics in (3.5), the Stieltjes transform $\hat{s}$ of the asymptotic eigenvalue density $\widehat{\mathrm{p}}(\lambda)$ is a solution to [30]:

$$\hat{s} = \sum_{i=1,2} \frac{\xi_i}{\Lambda_i \left(1 - \nu - \nu z \hat{s}\right) - z}, \tag{3.29}$$

As $\nu \to 0$, $\hat{s} \to s$, which is the Stieltjes transform of $\mathrm{p}(\lambda)$, the eigenvalue density of Σ in (3.20), and is given by

$$s = \sum_{i=1,2} \frac{\xi_i}{\Lambda_i - z}. \tag{3.30}$$

Considering (3.29) for $z \to \lambda \in \mathbb{R}\backslash\{0\}$ and simplifying, $\hat{s}$ then is the root of a polynomial with real coefficients (whose degree is 2 or 3, depending on the number of distinct non-zero eigenvalues of Σ). Since the array element spacing, frequency of interest and the ratio of number of array elements to the number of snapshots are known, (3.29) can be solved in terms of β (or equivalently, Λ_i and ξ_i) and ν.

Since $\widehat{\mathrm{p}}(\lambda)$ has not been defined at $\lambda = 0$, we define it as follows, using the fact that the area under the density is 1:

$$\widehat{\mathrm{p}}(0) = 1 - \int_{\lambda > 0} \widehat{\mathrm{p}}(\lambda) d\lambda \tag{3.31}$$

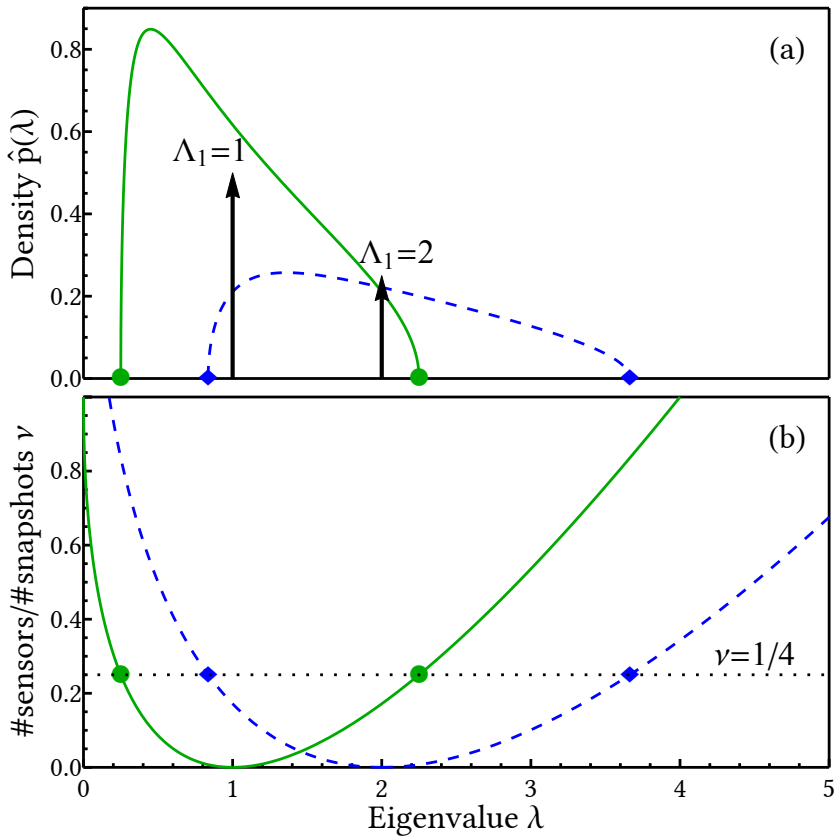

Figure 3.3: (a) Asymptotic eigenvalue density for $\nu = 1/4$ and $\beta = 1/4$ (dashed, $\Lambda_1 = 2$) and $\beta = 1/2$ (solid, M-P density, $\Lambda_1 = 1$). Only the contribution from the non-zero eigenvalue is shown for $\beta = 1/4$. The extent of spreading is marked by symbols and the non-zero eigenvalue Λ_1 in each case is marked by an arrow. (b) Change in the spreading of the densities in (a) for different ν.

Noting that covariance matrices are non-negative definite (i.e., eigenvalues are non-negative) and that the normalized ranks $\mathcal{R}(\Sigma)$ and $\mathcal{R}(\widehat{\Sigma})$ are equal in the asymptotic limit, it follows that

$$\widehat{\mathrm{p}}(0) = \mathrm{p}(0) = \begin{cases} \xi_2 & \beta < 1/2, \\ 0 & \text{otherwise.} \end{cases} \tag{3.32}$$

3.3.2 Density for Spatially Oversampled Case ($\beta < 1/2$)

In this section, the eigenvalue density is first derived from the MP density using linear algebra and then again using Stieltjes transforms in order to illustrate concepts essential in Section 3.3.4.

Using the eigendecomposition $\Sigma = \mathbf{U}\mathbf{\Lambda}\mathbf{U}^H$ in (3.5) gives

$$\widehat{\Sigma} = \frac{1}{M}\mathbf{U}\mathbf{\Lambda}^{1/2}\mathbf{X}'\left(\mathbf{\Lambda}^{1/2}\mathbf{X}'\right)^H\mathbf{U}^H, \tag{3.33}$$

where $\mathbf{X}'$ is also an $N \times M$ random matrix with elements $\sim \mathcal{CN}(0,1)$ (since $\mathbf{X}$ is GUE). From (3.22), the eigenvalues of Σ and $\mathbf{\Lambda}$ are Λ_1 with multiplicity ratio ξ_1 and zero with multiplicity ratio ξ_2. Due to the zero eigenvalue, only the upper ξ_1 portion of $\mathbf{X}'$ contributes to the matrix multiplication in the asymptotic limit or equivalently, the array elements to snapshot ratio decreases to $\tilde{\nu} = \nu\xi_1$. Hence the distribution of the non-zero eigenvalue of $\widehat{\Sigma}$ also follows the MP density in (3.6), albeit with $\tilde{\nu}$ instead of ν.

So, the eigenvalue density of $\widehat{\Sigma}$ can be written as

$$\widehat{\mathrm{p}}(\lambda) = \begin{cases} \xi_1 \frac{\sqrt{(\lambda_+ - \lambda)(\lambda - \lambda_-)}}{2\pi\nu\lambda} & \lambda_- < \lambda < \lambda_+ \\ \xi_2\delta(\lambda) & \text{otherwise} \end{cases} \tag{3.34}$$

Here, $\lambda_\pm$ are modified forms of $l_\pm$ in (3.6), to account for $\widetilde{\nu}$ and the scaling by Λ_1, given by

$$\lambda_\pm = \Lambda_1\left(1 \pm \sqrt{\widetilde{\nu}}\right)^2 = \frac{(1 + \sqrt{2\beta\nu})^2}{2\beta} \tag{3.35}$$

The first term in (3.34) accounts for the density due to the spreading of the non-zero eigenvalue Λ_1 [see Fig. 3.3(a)] and the second term in (3.34) is the density due to the zero eigenvalue. The density at $\lambda = 0$ remains unchanged from that of the true CM as in (3.32). Note that although the first term is similar in form to the M-P density in (3.6), the spreading $\lambda_\pm$ is different and is given by (3.39).

Equation (3.34) also can be arrived at using the Stieltjes transform in Section 3.3.1. Using Λ_i and ξ_i from (3.22) and (3.23), (3.29) simplifies to

$$\nu\lambda^2\hat{s}^2 + \lambda\left[2\beta\lambda - 2(\beta - 1)\nu - 1\right]\hat{s} + 2\beta(1 - \nu + \lambda) + \nu - 1 = 0, \tag{3.36}$$

To obtain the density $\widehat{\mathrm{p}}$ from (3.28), (3.36) is solved for $\hat{s}$, keeping only the solution where $\mathrm{Im}[\hat{s}] > 0$ since $\widehat{\mathrm{p}}(\lambda) > 0$, resulting in

$$\mathrm{Im}[\hat{s}] = \sqrt{-D}/(2\nu\lambda^2) \quad \text{for} \quad D < 0 \tag{3.37}$$

where the discriminant D is factored as

$$\begin{aligned} D &= \lambda^2\left[4\beta^2(\nu - \lambda)^2 - 4\beta(\nu + \lambda) + 1\right] \\ &= 4\beta^2\lambda^2(\lambda - \lambda_-)(\lambda - \lambda_+), \end{aligned} \tag{3.38}$$

with

$$\lambda_{\pm} = \frac{(1 \pm \sqrt{2\beta\nu})^2}{2\beta} = (\sqrt{\Lambda_1} \pm \sqrt{\nu})^2, \tag{3.39}$$

which is identical to (3.35). Hence, the real roots of the discriminant D provide the bounds for the density. $\mathrm{Im}[\hat{s}]$ can then be written as

$$\mathrm{Im}[\hat{s}] = \begin{cases} \frac{\xi_1\sqrt{(\lambda_+ - \lambda)(\lambda - \lambda_-)}}{2\nu\lambda} & \lambda_- < \lambda < \lambda_+, \\ 0 & \text{otherwise} \end{cases} \tag{3.40}$$

and from (3.28) and (3.32), (3.34) can be obtained.

Typically, in array processing applications, zero eigenvalues are encountered only when the SCM is snapshot starved ($\nu > 1$). However, from (3.34), the SCM always will be degenerate for $\beta < 1/2$.

3.3.3 Density for Spatially Nyquist Sampled Case ($\beta = 1/2$)

The density in this case and for all $\beta = q/2,\ q \in \mathbb{N}$ is given by the M-P density as discussed in Section 3.1.2. Equation (3.34) is a generalized form of M-P and indeed (3.6) follows from (3.34) for $\Lambda_1 = 1$ and $\xi_2 = 0$. From Fig. 3.3(b), it is clear that the spreading of the eigenvalues is wider in the oversampled case (dashed) than the Nyquist sampled case (solid), even though the noise power on each sensor is the same.

3.3.4 Density for Spatially Undersampled Case ($\beta > 1/2$)

Eigenvalue densities for SCMs, where the true CM has two non-zero eigenvalues (with multiplicities), have been studied in the context of detecting signals in uncorrelated noise [32]. Proceeding as in the previous section, (3.29) simplifies to

$$\begin{aligned} &\hat{s}^3\lambda^2\Lambda_1\Lambda_2\nu^2 + \hat{s}^2\lambda\nu\left[\lambda(\Lambda_1 + \Lambda_2) + 2\Lambda_1\Lambda_2(\nu - 1)\right] \\ &+ \hat{s}\left[\lambda^2 + \lambda\nu(\Lambda_2\xi_1 + \Lambda_1\xi_2) + \lambda(\Lambda_1 + \Lambda_2)(\nu - 1)\right. \\ &\left.+\Lambda_1\Lambda_2(\nu - 1)^2\right] + \lambda + (\Lambda_1\xi_2 + \Lambda_2\xi_1)\,(\nu - 1) = 0. \end{aligned} \tag{3.41}$$

The above cubic has one real root and the other two roots, if complex, exist as conjugate pairs. Normalizing (3.41) to the form $\hat{s}^3 + a_2\hat{s}^2 + a_1\hat{s} + a_0 = 0$, the desired solution for

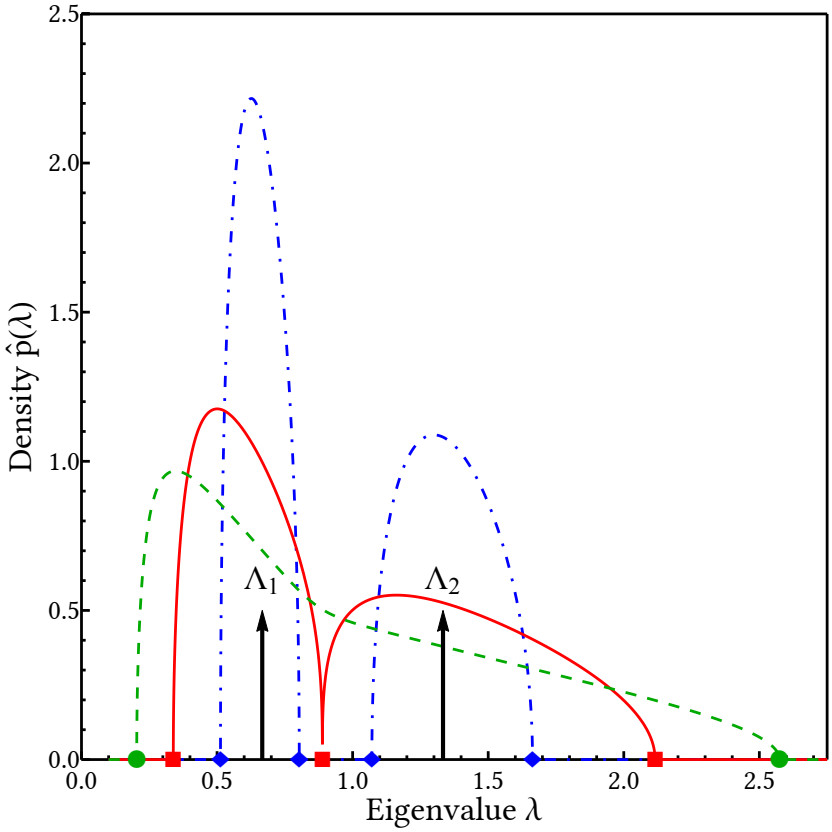

Figure 3.4: Asymptotic eigenvalue density of the SCM for $\beta = 3/4$ and $\nu = 1/40$ (dot-dashed), $\nu = 1/4$ (dashed) and $\nu_s \approx 0.115$ the value of ν where the two regions combine (dotted). Each of these densities have finite intervals, marked by symbols. The eigenvalues Λ_1 and Λ_2 of the true CM Σ are shown by the arrows.

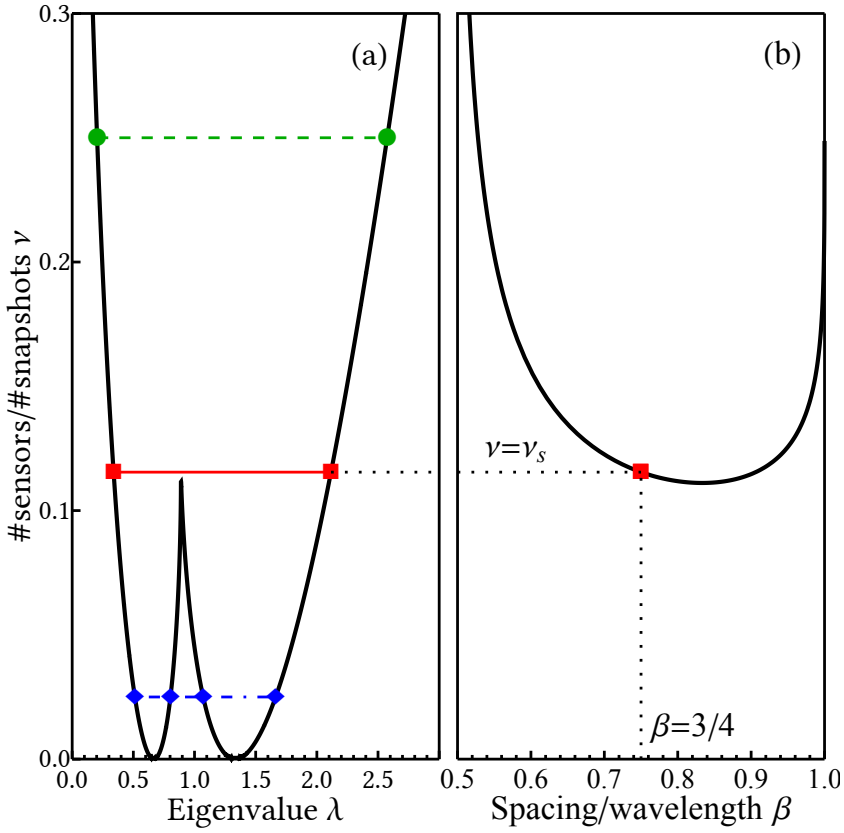

Figure 3.5: (a) Spreading of the asymptotic eigenvalue density for $\beta = 3/4$, showing the intervals of supports for $\nu = 1/4$ (dashed, circles), $\nu = 1/40$ (dot-dashed, diamonds) and $\nu = \nu_s \approx 0.115$ (horizontal solid line, squares) where the density splits into two intervals. (b) Change in ν_s with β for $\beta \in (1/2, 1)$ and the solid square marks ν_s corresponding to $\beta = 3/4$ in (b).

$\mathrm{Im}[\hat{s}]$ is given by

$$\mathrm{Im}[\hat{s}] = \mathrm{Im}\left[\frac{\left(1+i\sqrt{3}\right)R}{2} + \frac{\left(1-i\sqrt{3}\right)Q}{2R}\right], \tag{3.42}$$

where $R = \sqrt[3]{P+\sqrt{-D}}$ and $Q = (a_2^3 - 3a_1)/9$, with the discriminant $D = Q^3 - P^2$ and $P = (-2a_2^3 + 9a_1a_2 - 27a_0)/54$. Finally, to obtain the density from (3.28), $\mathrm{Im}[\hat{s}]$ is replaced with $|\mathrm{Im}[\hat{s}]|$ to include the positive contribution from the conjugate solution (see Fig. 3.4).

As in the previous section the real roots of the discriminant D (considering it as a polynomial in λ) give the bounds where $\widehat{\mathrm{p}}(\lambda) > 0$. The spreading of the eigenvalue density [Fig. 3.5(a)] can be understood from a physical viewpoint as follows.

When the SCM $\widehat{\Sigma}$ is formed from a relatively smaller number of snapshots, i.e., $M \sim N$ or $\nu \sim 1$, there is a larger uncertainty as to what the true eigenvalues are (small sample size). This results in the eigenvalues of the SCM spreading across the two true eigenvalues and resulting in a single spread out region [dashed line in Fig. 3.4 and Fig. 3.5(a)].

When the number of snapshots is much larger than the number of array elements i.e., $\nu \ll 1$, the uncertainty in the sample eigenvalues reduces and there are two intervals where $\widehat{\mathrm{p}}(\lambda) > 0$, localized around each of the true eigenvalues [dot-dashed line in Fig. 3.4 and Fig. 3.5(a)]. Having two distinct intervals is equivalent to the discriminant having four real roots.

The presence of two lobes in the eigenvalue density of the SCM has implications in signal detection. For example, if one were unaware of this phenomenon, one might conclude erroneously that the lobe associated with the larger eigenvalue is due to a signal, when in reality, it is only noise. Therefore, it is of interest to determine at what value of ν the density splits in two so as to take into account when processing data.

In Fig. 3.5(a), the curve splits into two distinct lobes at $\nu \approx 0.115$. The ν where this occurs, ν_s is a double root and can be obtained by setting the discriminant of the discriminant of the cubic to zero (see Appendix), and is found as

$$\nu_s = \frac{(\Lambda_1 - \Lambda_2)^2}{\left[\left(\Lambda_1^2 \xi_1\right)^{1/3} + \left(\Lambda_2^2 \xi_2\right)^{1/3}\right]^3} \tag{3.43}$$

The resulting curve for ν_s for $\beta \in (1/2, 1)$ is shown in Fig. 3.5(b). At all values of ν below this curve, the density will have two lobes.

3.4 Eigenvalue Density of the SCM for Finite N

Matrices of the type $\mathbf{X}\mathbf{X}^H$, where $\mathbf{X}$ is a GUE random matrix, are known as Wishart matrices [33] and the joint probability densities of their eigenvalues have been known for a while [34–37]. These densities are generally expressed as hypergeometric functions of the matrices themselves and are complicated and difficult to work with for both numerical and analytical analysis [37]. In recent work, the form of these

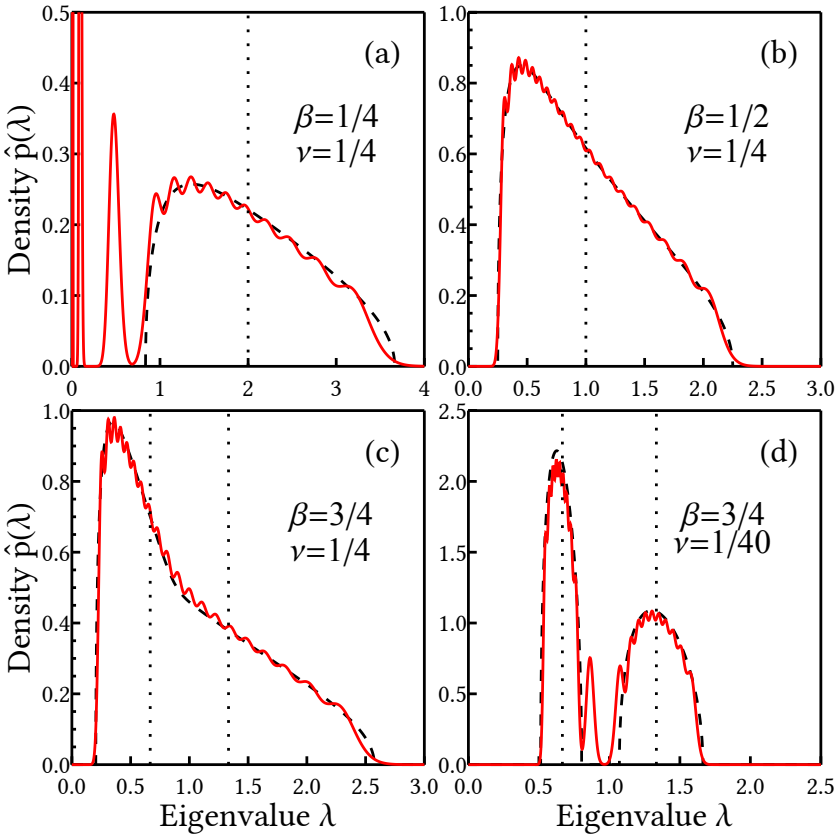

Figure 3.6: Asymptotic eigenvalue density (dashed line) and the analytical density for finite N, with $N = 20$ array elements, and (a–c) spacing to wavelength ratios $\beta = 1/4, 1/2$ and $3/4$ respectively for $\nu = 1/4$ (ratio of number of sensors to number of snapshots) i.e. $M = 80$ and (d) $\beta = 3/4$ for $\nu = 1/40$, i.e. $M = 800$

expressions were simplified by rederiving in terms of the product of two determinants [38, 39].

The results from [39] are applied to the isotropic noise SCM and the corresponding densities for different β are given in (3.44) and (3.45) in Appendix 3.B. In Fig. 3.6 the analytical densities for $N = 20$ (solid line) and the asymptotic density (dashed line) are shown for different values of β. The simpler asymptotic solution holds well for modest values of N, although it does not capture the effect of the transition eigenvalues [Fig. 3.6 in panel (a) around 0.5 and panel (d) around 0.8]. The number of local peaks in the solid line is the same as the number of distinct eigenvalues of the finite SCM, and correspond to the expectation of the means of the individual eigenvalues.

Evaluation of (3.44) and (3.45) are computationally intensive even for modest N. The computational complexity increases drastically with N [roughly $O(N^4)$], and the large exponents of both large and small numbers in the expressions make it unsuitable for numerical work without significant effort due to the limitations of floating point arithmetic. This is not immediately apparent from [39], as only the $N = 3$ case is considered there. In comparison, the asymptotic result captures most of the features of the eigenvalue density, and can be easily calculated from (3.34) or (3.42).

3.5 Simulations

A Monte–Carlo simulation is performed to compare the theoretical asymptotic results with the empirical eigenvalue density obtained for a finite N. In Fig. 3.7 and Fig. 3.8, realizations of the SCM are obtained as in (3.5) and the empirical densities of the eigenvalues are averaged over 1000 realizations in order to obtain statistically stable distributions. The asymptotic solution (solid lines) are obtained from (3.34) for $\beta = 1/4$, (3.6) for $\beta = 1/2$ and (3.28) with (3.42) for $\beta = 3/4$.

Fig. 3.7 shows the resulting empirical densities when $\nu = 1/4$ and different β for $N = 100$ [Fig. 3.7(a–c)] and $N = 20$ [Fig. 3.7(d–f)] respectively. In Fig. 3.7(a), nearly half the area is due to the peak at $\lambda = 0$ [exactly half in the asymptotic limit, as $\widehat{\mathrm{p}}(0) = \xi_2 = 1/2$ from (3.32)]. The asymptotic solutions describe the empirical densities

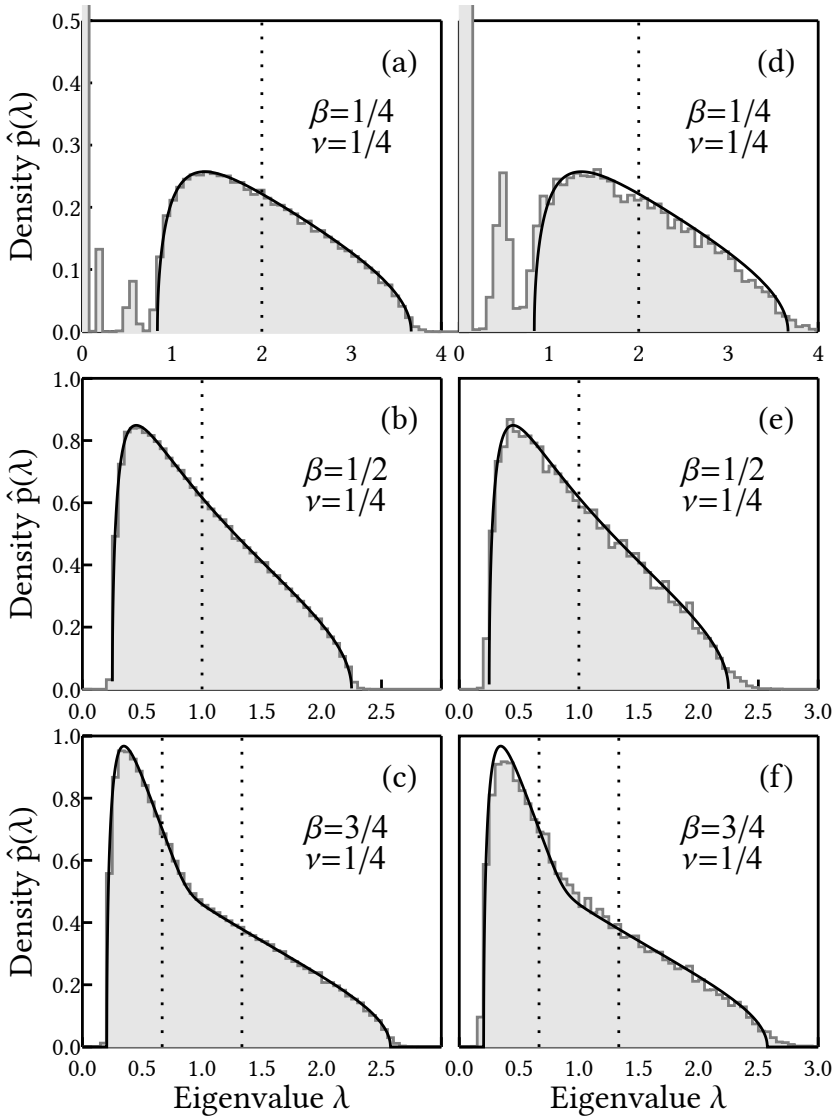

Figure 3.7: Asymptotic eigenvalue density (solid line) and the empirical eigenvalue density (grey), with $N = 100$ array elements, $\nu = 1/4$ (ratio of number of sensors to number of snapshots) and spacing to wavelength ratios β of (a) 1/4 (b) 1/2 and (c) 3/4. (d,e,f): Same as in (a,b,c) except with $N = 20$. The dotted lines show the locations of the distinct non-zero true eigenvalues. In (a) and (d), the y-axis is only shown between 0–0.5 so as to display the density due to the non-zero eigenvalue prominently.

quite well, except for tails at large λ as opposed to a sharp edge in the asymptotic case, which become more prominent as N decreases [e.g., Fig. 3.7(b) vs Fig. 3.7(e)].

Another clear consequence of finite N, is the contribution from transition eigenvalues, seen between 0.1–0.8 in Fig. 3.7(a,d) for $\beta = 1/4$. While their effect is not seen in Fig. 3.7(c,f) at $\nu = 1/4$ for $\beta = 3/4$, it becomes apparent when the number of snapshots is increased to $\nu = 1/40$ in Fig. 3.8(c,f). Here, the densities localize around the two asymptotic eigenvalues ($\Lambda_1 = 4/3$ and $\Lambda_2 = 2/3$) and the contributions from the transition eigenvalues [centered around $n/N = \xi_1 = 0.5$ in Fig. 3.8(a,d), where ξ_1 is from (3.25)] fill up the region in between them. Even at $\nu = \nu_s \approx 0.115$, when the density splits in the asymptotic case, the empirical density does not split entirely because of the transition eigenvalues, resulting in a non-zero contribution in Fig. 3.8(b,e).

Both of the above effects (tails and contributions from transition eigenvalues) are due to the finite dimension of the SCM and hence, they are not present in the asymptotic result. These effects become more pronounced as N decreases, because the transition eigenvalues form a larger percentage of the total number of eigenvalues [6/20 in Fig. 3.8(d) vs. 6/100 in Fig. 3.8(a)]. The difference between the largest eigenvalue of the CM in Fig. 3.8(a,d) and the corresponding asymptotic value in (3.24) is on the order of 10^{-14} for $N = 20$ and 10^{-15} for $N = 100$, indicating that the analytic solution is quite accurate.

3.6 Conclusions

In this article, the asymptotic eigenvalue densities have been derived for noise covariance matrices (CM) for line arrays with uniformly spaced elements in an isotropic noise field. The CM has at most two distinct eigenvalues for all values of β, the ratio of inter-element spacing to wavelength. From independent observations of the noise field, a sample noise covariance matrix (SCM) is formed using more snapshots than the number of array elements and its eigenvalues are analyzed using random matrix theory (RMT).

When the sensors are spaced less than half a wavelength apart, the SCM is always singular, no matter how many snapshots are used. For spacings of more than

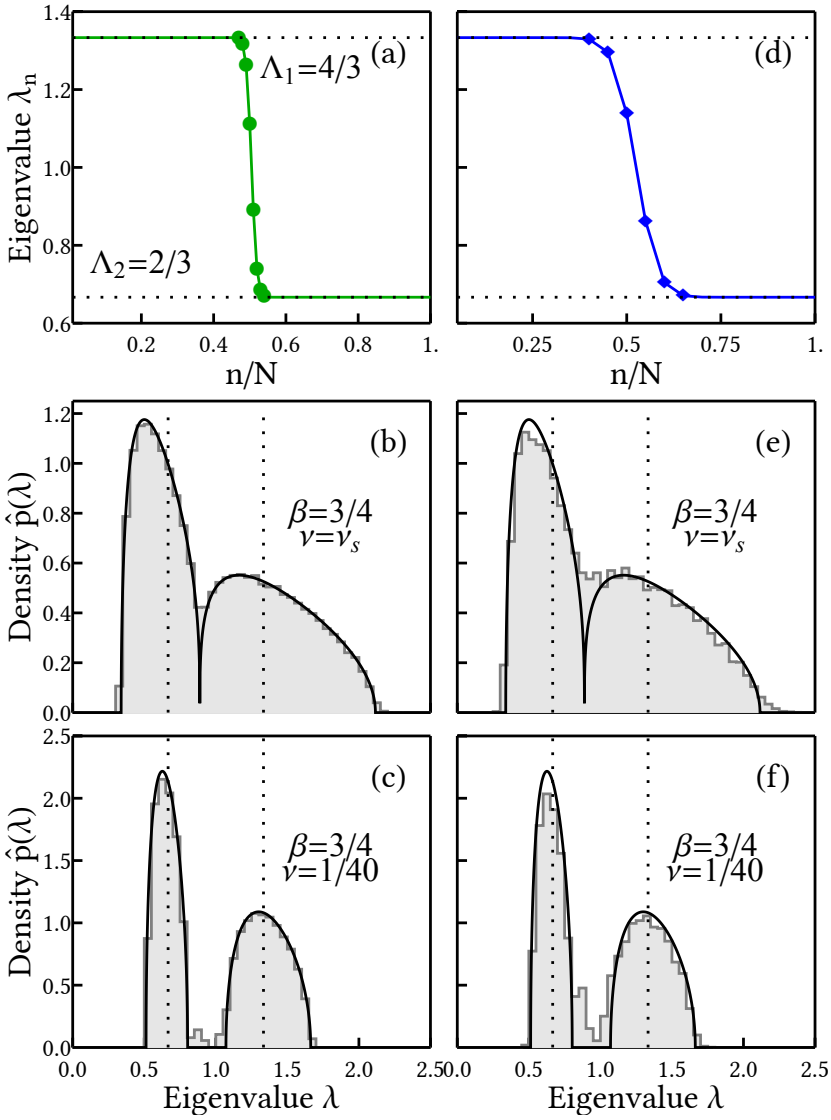

Figure 3.8: Effect of transition eigenvalues on the empirical eigenvalue density (grey) for $\beta = 3/4$ and (a)–(c) $N = 100$ and (d)–(f) $N = 20$. (a) and (d): Eigenvalues of the CM. The x-axis is a normalized index where $n = \{1, \ldots, N\}$. Only eigenvalues deviating from either Λ_1 or Λ_2 by 0.1% are marked. (b) and (e): Empirical density of the SCM $\nu = \nu_s \approx 0.115$ when the density splits. (c) and (f): Same as (b) and (e) for $\nu = 1/40$. The asymptotic density is shown by the solid line.

half a wavelength apart, the SCM is full rank if sufficient snapshots are used, but the eigenvalue density can split into two distinct densities.

Analytical results for finite Wishart matrices and simulations with finite SCMs confirm the asymptotic results derived using RMT. The results hold well even for arrays with as low as 20 sensors.

3.7 Acknowledgments

This work was supported by the Office of Naval Research, Grant Nos. N00014-11-1-0320 and N00014-11-1-0321.

Chapter 3, in full, is a reprint of the material as it appears in R. Menon, P. Gerstoft and W. S. Hodgkiss, "Asymptotic Eigenvalue Density of Noise Covariance Matrices", IEEE Trans. Signal Proc., **60**, 3415-3424 (2012) . The dissertation author was the primary researcher and author of this paper.

3.A Outline of Approach to Solve for ν_s

The derivation of (3.43) is tedious and the intermediate equations are lengthy and hence, omitted. An outline of the approach is provided here with hints.

1. Starting with (3.41), calculate the discriminant of the polynomial in $\hat{s}$. The result is a polynomial of degree 8 in λ that can be factored into a product of λ^4 and a quartic in λ.

2. Noting that $\lambda > 0$, only the quartic needs to be considered. Calculating the discriminant of the quartic results in a polynomial of degree 23 in ν, which can be factored into a product of ν^{14} and a polynomial of degree 9 in ν.

3. Again, discarding the ν^{14} term, the remaining degree 9 polynomial can be simplified into a cube of a cubic in ν. Finally, ν_s is the real root of

$$\begin{aligned}
&\nu^3 \left(\Lambda_1^2\xi_1 + \Lambda_2^2\xi_2\right)^3 \\
&- 3\nu^2 \left(\Lambda_1 - \Lambda_2\right)^2 \left(\Lambda_1^4\xi_1^2 - 7\Lambda_2^2\Lambda_1^2\xi_1\xi_2 + \Lambda_2^4\xi_2^2\right) \\
&+ 3\nu \left(\Lambda_1 - \Lambda_2\right)^4 \left(\Lambda_1^2\xi_1 + \Lambda_2^2\xi_2\right) - \left(\Lambda_1 - \Lambda_2\right)^6 = 0,
\end{aligned}$$

which upon simplifying, gives (3.43).

3.B Eigenvalue Density of the SCM for Finite N

Let Σ_N and $\widehat{\Sigma}_N$ denote the isotropic noise CM and SCM when N is finite and $\sigma_1, \ldots, \sigma_N$ be the eigenvalues of Σ_N. The following expressions are adapted from [39], using the notation followed in this text where necessary.

3.B.1 Density When $\beta = q/2,\ q \in \mathbb{N}$

Using (38) in [39], the density for finite N when $\beta = q/2,\ q \in \mathbb{N}$ (i.e., Σ is the identity matrix) is

$$\begin{aligned}\widehat{\mathrm{p}}_N(\lambda) =& K \sum_{n=1}^{N} \sum_{n'=1}^{N} (-1)^{n+n'} (M\lambda)^{n+n'-2+M-N} \\ & \times e^{-M\lambda} \det(\Omega(n, n'))\end{aligned} \tag{3.44}$$

where

$$\begin{aligned}K =& \frac{M}{\prod_{i=1}^{N}(M-i)! \prod_{j=1}^{N}(N-j)!} \\ \Omega_{ij}(n, n') =& N^{-1/(N-1)} \left[\mu_{ij}(n, n') + M - N\right]! \\ \mu_{ij}(n, n') =& \begin{cases} i+j-2 & \text{if } i < n \text{ and } j < n' \\ i+j & \text{if } i \geq n \text{ and } j \geq n' \\ i+j-1 & \text{otherwise} \end{cases}\end{aligned}$$

3.B.2 Density for All Other β

Using (41) in [39], the density for all other β for finite N is

$$\begin{aligned}\widehat{\mathrm{p}}_N(\lambda) =& K' \sum_{n=1}^{N} \sum_{n'=1}^{N} (-1)^{n+n'} (M\lambda)^{M-N+n-1} \\ & \times e^{-M\lambda/\sigma_{n'}} \det(\Omega'(n, n'))\end{aligned} \tag{3.45}$$

where

$$
\begin{aligned}
K' =& K \prod_{i=1}^{N} (i-1)! \frac{\det(\Sigma_N)^{-M}}{\det(\mathbf{V})} \\
\mathbf{V}_{ij} =& (-\sigma_j)^{1-i} \\
\Omega'_{ij}(n,n') =& N^{-1/(N-1)} (\sigma_{r(j,n')})^{M-N+r(i,n)} \\
& \times (M-N+r(i,n)-1)! \\
r(i,j) =& \begin{cases} i & i < j \\ i+1 & i \geq j \end{cases}
\end{aligned}
$$

Bibliography

[1] O. I. Lobkis and R. L. Weaver, "On the emergence of the Green's function in the correlations of a diffuse field," *J. Acoust. Soc. Am.*, vol. 110, pp. 3011–3017, December 2001.

[2] R. L. Weaver and O. I. Lobkis, "Ultrasonics without a source: Thermal fluctuation correlations at MHz frequencies," *Phys. Rev. Lett.*, vol. 87, p. 134301, 2001.

[3] K. G. Sabra, P. Gerstoft, P. Roux, W. A. Kuperman, and M. C. Fehler, "Extracting time-domain Green's function estimates from ambient seismic noise," *Geophys. Res. Lett*, vol. 32, p. L03310, 2005.

[4] N. M. Shapiro, M. Campillo, L. Stehly, and M. H. Ritzwoller, "High-resolution surface-wave tomography from ambient seismic noise," *Science*, vol. 307, pp. 1615–1618, 2005.

[5] P. Roux, W. A. Kuperman, and the NPAL group, "Extracting coherent wave fronts from acoustic ambient noise in the ocean," *J. Acoust. Soc. Am.*, vol. 116, pp. 1995–2003, 2004.

[6] L. A. Brooks and P. Gerstoft, "Green's function approximation from cross-correlations of 20–100 Hz noise during a tropical storm," *J. Acoust. Soc. Am.*, vol. 125, pp. 723–734, Jan 2009.

[7] A. Duroux, K. G. Sabra, J. Ayers, and M. Ruzzane, "Extracting guided waves from cross-correlations of elastic diffuse fields: applications to remote structural health monitoring," *J. Acoust. Soc. Am.*, vol. 127, pp. EL42–EL47, 2010.

[8] M. L. Mehta, *Random Matrices.* Academic Press, 3rd ed., 2004.

[9] A. Edelman and N. R. Rao, "Random matrix theory," *Acta Numerica*, vol. 14, no. -1, pp. 233–297, 2005.

[10] H. Cox, "Spatial correlation in arbitrary noise fields with application to ambient sea noise," *J. Acoust. Soc. Am.*, vol. 54, no. 5, pp. 1289–1301, 1973.

[11] R. R. Nadakuditi and A. Edelman, "Sample eigenvalue based detection of high-dimensional signals in white noise using relatively few samples," *IEEE Trans. Signal Proc.*, vol. 56, no. 7, pp. 2625–2638, 2008.

[12] R. R. Müller, "A random matrix model of communication via antenna arrays," *IEEE Trans. Info. Theory*, vol. 48, no. 9, pp. 2495–2506, 2002.

[13] A. M. Tulino and S. Verdú, "Random matrix theory and wireless communications," *Foundations and Trends in Communications and Information Theory*, vol. 1, no. 1, pp. 1–182, 2004.

[14] R. L. Weaver, "Spectral statistics in elastodynamics," *J. Acoust. Soc. Am.*, vol. 85, pp. 1005–1013, 1989.

[15] A. Aubry and A. Derode, "Random matrix theory applied to acoustic backscattering and imaging in complex media," *Phys. Rev. Lett.*, vol. 102, p. 084301, 2009.

[16] A. Aubry and A. Derode, "Detection and imaging in a random medium: A matrix method to overcome multiple scattering and aberration," *J. Appl. Phys.*, vol. 106, p. 044903, 2009.

[17] S. E. Skipetrov and A. Goetschy, "Eigenvalue distributions of large Euclidean random matrices for waves in random media," *J. Phys. A: Math. Theor.*, vol. 44, p. 065102, 2011.

[18] X. Mestre, "On the asymptotic behaviour of the sample estimates of eigenvalues and eigenvectors of covariance matrices," *IEEE Trans. Signal Proc.*, vol. 56, no. 11, pp. 5353–5368, 2008.

[19] R. R. Nadakuditi and J. W. Silverstein, "Fundamental limit of sample generalized eigenvalue based detection of signals in noise using relatively few signal-bearing and noise-only samples," *IEEE J. Sel. Top. Signal Proc.*, vol. 4, no. 3, pp. 468–480, 2010.

[20] V. A. Marčenko and L. A. Pastur, "Distributions of eigenvalues of some sets of random matrices," *Math. Sb.*, vol. 72, pp. 507–536, 1967.

[21] D. Slepian, "Prolate spheroidal wave functions, Fourier analysis, and uncertainty — v: The discrete case," *The Bell System Technical Journal*, vol. 57, no. 5, pp. 1371–1430, 1978.

[22] M. Zatman, "Production of adaptive array troughs by dispersion synthesis," *Electron. Lett.*, vol. 31, no. 25, pp. 2141–2142, 1995.

[23] R. J. Mailloux, "Covariance matrix augmentation to produce adaptive array pattern troughs," *Electron. Lett.*, vol. 31, no. 25, pp. 771–772, 1995.

[24] U. Grenander and G. Szegö, *Toeplitz forms and their applications.* Chelsea publishing Co., New York, 1984.

[25] R. M. Gray, "Toeplitz and circulant matrices: A review," *Found. Trends. Comm. Inf. Theory*, vol. 2, no. 3, pp. 155–239, 2006.

[26] H. J. Landau and H. Widom, "The eigenvalue distribution and frequency limiting," *J. Math. Anal.*, vol. 77, pp. 469–481, 1980.

[27] D. Slepian, "Some comments on Fourier analysis, uncertainty and modeling," *SIAM Review*, vol. 25, no. 3, pp. 379–393, 1983.

[28] L. Cottatellucci, R. R. Müller, and M. Debbah, "Asynchronous CDMA systems with random spreading — Part I: Fundamental limits," *IEEE Trans. Inform. Theory*, vol. 56, no. 4, pp. 1477–1497, 2010.

[29] D. H. Johnson and D. E. Dudgeon, *Array processing: Concepts and techniques.* Prentice Hall, 1993.

[30] J. W. Silverstein, "Strong convergence of the empirical distribution of eigenvalues of large dimensional random matrices," *J. Multivar. Anal.*, vol. 54, pp. 175–192, 1995.

[31] J. W. Silverstein and S. Choi, "Analysis of the limiting spectral distribution of large dimensional random matrices," *J. Multivar. Anal.*, vol. 54, pp. 395–209, 1995.

[32] Z. Burda, A. T. Görlich, A. Jarosz, and J. Jurkiewicz, "Signal and noise in correlation matrix," *Physica A*, vol. 343, pp. 295–310, 2004.

[33] J. Wishart, "The generalized product moment distribution in samples from a normal multivariate population," *Biometrika*, vol. 20A, pp. 32–52, 1928.

[34] A. T. James, "The distribution of the latent roots of the covariance matrix," *Ann. Math. Statist.*, vol. 31, pp. 151–158, 1960.

[35] T. W. Anderson, "Asymptotic theory for principal component analysis," *Ann. Statist.*, vol. 34, pp. 122–148, 1963.

[36] T. W. Anderson, *An introduction to multivariate statistical analysis.* John Wiley & Sons, Inc., 2nd ed., 1984.

[37] M. Siotani, T. Hayakawa, and Y. Fujikoshi, *Modern Multivariate Statistical Analysis: A Graduate Course and Handbook*. American Sciences Press, Inc., 1985.

[38] M. Chiani, M. Z. Win, and A. Zanella, "On the capacity of spatially correlated mimo rayleigh fading channels," *IEEE Trans. Inform. Theory*, vol. 49, no. 10, pp. 2363–2371, 2003.

[39] A. Zanella, M. Chiani, and M. Z. Win, "On the marginal distribution of the eigenvalues of wishart matrices," *IEEE Trans. Commun.*, vol. 57, no. 4, pp. 1050–1060, 2009.

4

EFFECT OF MEDIUM ATTENUATION ON THE ASYMPTOTIC EIGENVALUES OF NOISE COVARIANCE MATRICES

Covariance matrices of noise models are used in signal and array processing to study the effect of various noise fields and array configurations on signals and their detectability. Here, the asymptotic eigenvalues of noise covariance matrices in 2D and 3D attenuating media are derived. The asymptotic eigenvalues are given by a continuous function, which is the Fourier transform of the infinite sequence formed by sampling the spatial coherence function. The presence of attenuation decreases the value of the large eigenvalues and raises the value of the smaller eigenvalues (compared to the attenuation free case). The eigenvalue density of the sample covariance matrix also shows variation in shape depending on the attenuation, which potentially could be used to retrieve medium attenuation properties from observations of noise.

4.1 Introduction

Covariance matrices (CMs) play a central role in several applications such as direction of arrival estimation [1, 2], signal detection from limited data [3–5], channel

estimation in wireless communications [6,7] and ambient noise processing [8–10]. Estimating the CM or its eigenvalues from finite observations [11,12] also plays an important role in these applications. The presence of structure in the CM (e.g., a Hermitian Toeplitz matrix [13]) makes it possible to gain analytical insights into the asymptotic behavior of the eigenvalues.

Here, we are concerned with the spatial CMs from measurements of noise on a uniform line array (ULA). We derive the asymptotic eigenvalues for CMs in 2D and 3D media with attenuation, and demonstrate that the attenuation has a significant effect on the eigenvalues of the CM. We futher demonstrate using a random matrix theory based approximation [14], that the eigenvalue density of the sample covariance matrix (SCM) is also affected by the attenuation, which is of interest in the development of signal processing algorithms based on the physics of propagation in a given medium.

4.2 Background

4.2.1 The Spatial Coherence Function

Consider two sensors Δx apart, and the signals recorded on them, $\psi_1(f)$ and $\psi_2(f)$ at frequency f. The respective power spectral densities are $P_{11}(f) = \langle \psi_1(f)\psi_1^\dagger(f)\rangle$ and $P_{22}(f) = \langle \psi_2(f)\psi_2^\dagger(f)\rangle$ where † denotes the complex conjugate and $\langle\cdot\rangle$ the ensemble average. The spatial coherence function (SCF) between these two sensors is defined as the normalized cross-spectral density (henceforth, the dependence on f is dropped),

$$\Gamma = \frac{P_{12}}{\sqrt{P_{11}P_{22}}} \tag{4.1}$$

The functional forms of Γ are well known for uncorrelated and uniformly distributed sources in the medium. In 2D and 3D media without attenuation, the respective SCFs are [15]

$$\Gamma_0^{\mathrm{2D}}(\beta) = \mathrm{J}_0(2\pi\beta) \tag{4.2}$$

$$\Gamma_0^{\mathrm{3D}}(\beta) = \mathrm{sinc}(2\beta) \tag{4.3}$$

where $\mathrm{sinc}(z) = \frac{\sin(\pi z)}{\pi z}$, $\beta = \frac{f\Delta x}{c} \geq 0$ is the spacing to wavelength ratio, c is the phase

speed and the subscript 0 indicates no attenuation. The SCFs in (4.2) and (4.3) are not dependent on the individual sensor locations, but only on their separation distance.

The effect of medium attenuation (assumed homogeneous) is introduced using a term that exponentially decays with the distance of separation between the sensors (which manifests in β) [16–19] and the SCF is

$$\Gamma_\delta(\beta) = e^{-2\pi\beta\delta}\Gamma_0(\beta) \tag{4.4}$$

where δ is the *loss tangent*.

4.2.2 The Spatial Covariance Matrix

For a ULA of N sensors with a uniform spacing Δx, the SCF of the noise field between the ith and the jth sensors is $\Gamma_\delta(\beta|i-j|)$ where β now is redefined as the spacing to wavelength ratio for adjacent sensors. The normalized CM Σ_δ (or the normalized cross-spectral density matrix) of the frequency domain observations at frequency f is then related to Γ_δ as

$$\Sigma_\delta(i,j) = \Gamma_\delta(\beta|i-j|). \tag{4.5}$$

$\Gamma_\delta(\beta|i-j|)$, with constant β can be considered to be sampled from the continuous function $\Gamma_\delta(\beta|x|)$ at integer values of x. $\Gamma_\delta(\beta|x|)$ is used in Section 4.3 to derive the asymptotic eigenvalues of Σ_δ.

The spatial CM is an important quantity in analyzing noise data, as the time domain cross-correlation between any two pairs of sensors can be obtained simply by taking the inverse Fourier transform of the corresponding element (as a function of frequency). The framework also allows one to use eigenanalysis techniques such as principal components analysis and RMT.

The CM in (4.5) is a Hermitian Toeplitz matrix with real and non-negative eigenvalues. The asymptotic eigenvalues of Σ_δ as $N \to \infty$ are related to the Fourier transform of the underlying infinite sequence $\Gamma_\delta(\beta|n|),\ n \in \mathbb{Z}$ in the Toeplitz matrix (sampled from $\Gamma_\delta(\beta|x|)$ with a sampling interval of 1), if the sequence is absolutely summable [13]. The property of absolute summability of $\Gamma_\delta(\beta|n|)$ guarantees the existence of its Fourier transform $\varphi_\delta(\kappa)$ and the absolute convergence of the error between the samples of $\varphi_\delta(\kappa)$ and the eigenvalues of Σ_δ as $N \to \infty$.

4.3 Asymptotic Eigenvalues of the CM

For a general CM with a corresponding Γ_δ, which may not be absolutely summable, the matrix based approach in [8] may be used to show a weaker convergence of the error term. The Fourier transform of Γ_δ is

$$\varphi_\delta(\kappa) = \sum_{n=-\infty}^{\infty} \Gamma_\delta(\beta|n|) e^{-\imath 2\pi\kappa n} \tag{4.6}$$

where $\kappa \in [-\frac{1}{2}, \frac{1}{2})$ is the normalized spatial frequency (cycles/sample). $\varphi_\delta(\kappa)$ is a continuous function describing the asymptotic eigenvalues of Σ_δ. Using the continuous Fourier transform (CFT) $\mathcal{G}_\delta(\gamma)$ of the SCF,

$$\mathcal{G}_\delta(\gamma) = \int_{-\infty}^{\infty} \Gamma_\delta(\beta|x|) e^{-\imath 2\pi\gamma x} \, \mathrm{d}x, \tag{4.7}$$

where γ is the ordinary spatial frequency, (4.6) is written as

$$\varphi_\delta(\kappa) = \sum_{n=-\infty}^{\infty} \mathcal{G}_\delta(\kappa - n). \tag{4.8}$$

Since Γ_δ is real and even, $\mathcal{G}_\delta$ and φ_δ are also real and even. For the attenuation free case, $\Gamma_0^{2\mathrm{D}}$ and $\Gamma_0^{3\mathrm{D}}$ are bandlimited functions, hence only the $n = 0$ term contributes in (4.8) for $\beta \leq \frac{1}{2}$ (i.e., no spatial aliasing).

In the following section, we obtain the asymptotic eigenvalues of the CM in attenuating media for the 2D and 3D noise fields i.e., when the SCF is given by (4.4) and also establish the convergence of empirical results for 2D media without attenuation.

4.3.1 2D Medium With Attenuation

The infinite sequence $\Gamma_\delta^{2\mathrm{D}}(\beta|n|)$ from (4.4), is absolutely summable because of the presence of an attenuation term. Noting that $|\mathrm{J}_0(x)| \leq 1$, we have $\forall \delta > 0$:

$$\begin{aligned}\sum_{n=-\infty}^{\infty} |\Gamma_\delta^{2\mathrm{D}}(\beta|n|)| &= \sum_{n=-\infty}^{\infty} |e^{-2\pi\beta\delta|n|} \mathrm{J}_0(2\pi\beta n)| \\ &\leq \sum_{n=-\infty}^{\infty} e^{-2\pi\beta\delta|n|} = \frac{e^{2\pi\beta\delta} + 1}{e^{2\pi\beta\delta} - 1} < \infty\end{aligned}$$

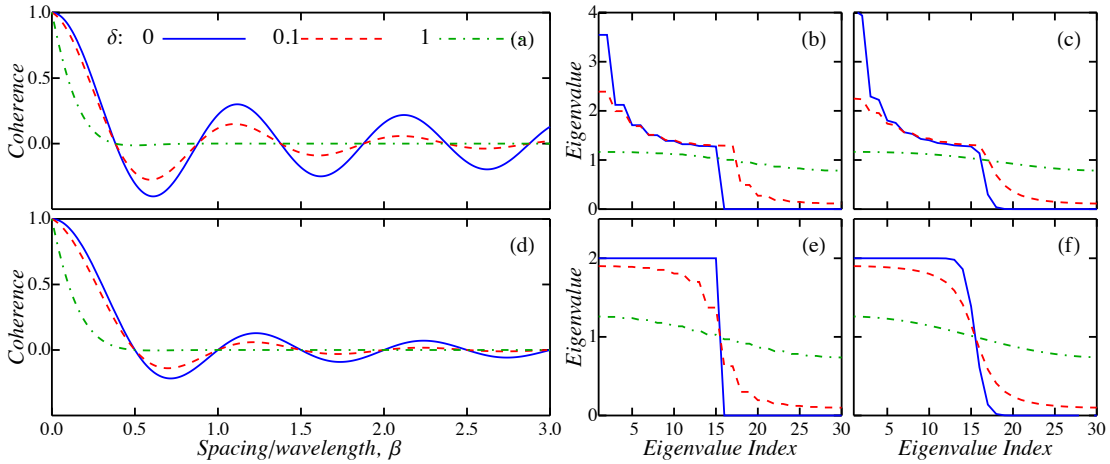

Figure 4.1: (a) SCF $\Gamma_\delta^{2D}(\beta)$ for $\delta = 0$ (solid), 0.1 (dashed) and 1 (dot-dashed). (b) Approximate eigenvalues from sampling the Fourier transform $\varphi_\delta^{2D}(\kappa)$ of the SCF at $N = 30$ equispaced samples in $[-\frac{1}{2}, \frac{1}{2})$ for $\beta = \frac{1}{4}$ and (c) numerical eigenvalues of the spatial CM Σ_δ for $N = 30$ sensors for the same values of δ and β. (d)–(f) Same as in (a)–(c) for 3D media.

The CFT of the SCF Γ_δ^{2D} is evaluated by using the integral representation of the Bessel function:

$$\begin{aligned}\mathcal{G}_\delta^{2D}(\gamma) &= \frac{1}{\pi}\int_{-\infty}^{\infty} e^{-\imath 2\pi\gamma x} e^{-2\pi\beta\delta|x|} \int_0^{\pi} e^{\imath 2\pi\beta x\cos(\theta)}\,\mathrm{d}\theta\,\mathrm{d}x \\ &= \Re\left[\frac{1}{\pi^2}\int_0^{\pi}\frac{\mathrm{d}\theta}{\beta\delta + \imath\gamma - \imath\beta\cos(\theta)}\right] \\ &= \frac{1}{\pi}\Re\left[\frac{1}{\sqrt{(\beta\delta+\imath\gamma)^2+\beta^2}}\right] \end{aligned} \tag{4.9}$$

(the second step follows from the fact that the imaginary part of the integrand is odd, and the last step is obtained using the substitution $u = \tan\theta/2$). $\varphi_\delta^{2D}(\kappa)$ is then obtained using (4.8) and (4.9).

When $\delta = 0$ (i.e., no attenuation), $\mathcal{G}_\delta^{2D}$ in (4.9) reduces to the CFT of Γ_0^{2D} in (4.2) and $\varphi_0^{2D}(\kappa)$ for $\beta \le \frac{1}{2}$ [only the $n = 0$ term contributes in (4.8)] is [10]

$$\varphi_0^{2D}(\kappa) = \frac{\mathrm{rect}\left(\frac{\kappa}{2\beta}\right)}{\pi\sqrt{\beta^2-\kappa^2}} \tag{4.10}$$

where $\mathrm{rect}(x) = 1 \;\forall\; |x| \leq \frac{1}{2}$ and 0 otherwise. The convergence of $\Gamma_0^{2\mathrm{D}}(\beta|n|)$ is shown in the appendix.

4.3.2 3D Medium With Attenuation

Just as in Section 4.3.1, $\Gamma_\delta^{3\mathrm{D}}(\beta|n|)$ from (4.4) can also be shown to be absolutely summable. Its CFT is evaluated by convolving the Fourier transforms of each of the terms in the expression as:

$$\begin{aligned}\mathcal{G}_\delta^{3\mathrm{D}}(\gamma) &= \mathcal{F}\left[e^{-2\pi\beta\delta|x|}\right] \star \mathcal{F}\left[\mathrm{sinc}(2\beta x)\right] \\ &= \left[\frac{1}{\pi}\frac{\beta\delta}{\beta^2\delta^2+\gamma^2}\right] \star \left[\frac{1}{2\beta}\,\mathrm{rect}\left(\frac{\gamma}{2\beta}\right)\right]\end{aligned}$$

where $\mathcal{F}$ denotes the CFT. Then, it follows that

$$\begin{aligned}\mathcal{G}_\delta^{3\mathrm{D}}(\gamma) &= \frac{\delta}{2\pi}\int_{-\infty}^{\infty}\frac{\mathrm{rect}\left(\frac{\gamma'}{2\beta}\right)}{\beta^2\delta^2+(\gamma-\gamma')^2}\,\mathrm{d}\gamma' \\ &= \frac{1}{2\pi\beta}\left[\tan^{-1}\left(\frac{\gamma+\beta}{\beta\delta}\right)-\tan^{-1}\left(\frac{\gamma-\beta}{\beta\delta}\right)\right] \qquad (4.11)\end{aligned}$$

Finally, $\varphi_\delta^{3\mathrm{D}}(\kappa)$ is obtained using (4.8) and (4.11).

When $\delta = 0$ (i.e., no attenuation), $\Gamma_\delta^{3\mathrm{D}}$ in (4.11) reduces to the CFT of $\Gamma_0^{3\mathrm{D}}$ in (4.3) and $\varphi_0^{3\mathrm{D}}(\kappa)$ for $\beta \leq \frac{1}{2}$ [only the $n = 0$ term contributes in (4.8)] is [8]

$$\varphi_0^{3\mathrm{D}}(\kappa) = \frac{1}{2\beta}\,\mathrm{rect}\left(\frac{\kappa}{2\beta}\right) \qquad (4.12)$$

4.4 Discussion

4.4.1 Effect of Attenuation on the Bandwidth and the Eigenvalues

The presence of attenuation ($\delta \neq 0$) makes the SCF an infinite bandwidth function (bandwidth here refers to the support in the Fourier domain). Hence in general, simplified expressions for $\varphi_\delta(\kappa)$ cannot be obtained as a function of δ, and must be computed using the sum (4.8). The effect of the attenuation term on the SCF is shown

in Fig. 4.1 (a) for Γ_δ^{2D} for $\delta = 0$ (no attenuation), 0.1, and 1 [Fig. 4.1 (d) for Γ_δ^{3D}]. The corresponding eigenvalues of Σ_δ for $N = 30$ sensors, with $\beta = \frac{1}{4}$ [Fig. 4.1(c), (f)] are approximated well by N equispaced samples [Fig. 4.1(b), (e)] from $\varphi_\delta(\kappa)$.

The broadening of the support (or bandwidth) due to an increase in attenuation visibly lowers the larger eigenvalues of the CM and raises the smaller eigenvalues [for example, in Fig 4.1 (c), $\lambda_{1,2} \approx 4$ for $\delta = 0$ (no attenuation) and ≈ 2.4 for $\delta = 0.1$]. In addition, the transition region (near index 15) between the large eigenvalues and the small eigenvalues, which is sharp for no attenuation ($\delta = 0$), spreads out as δ increases. The broadening of the transition region is more apparent in the 3D case [Fig. 4.1 (e), (f)]. As a result, the smaller eigenvalues which were zero in the attenuation free case [8,10], no longer are, and this increases the rank of the CM. For $\delta = 1$, i.e. high attenuation, the eigenvalues are all close to 1 and become exactly 1 when $\delta \to \infty$.

4.4.2 Eigenvalue Density of the Sample Covariance Matrix

In practice, the CM is often unknown and one uses the SCM estimated from M observations of the data. The SCM $\widehat{\Sigma}_\delta$ is modeled as

$$\widehat{\Sigma}_\delta = \frac{1}{M}\Sigma_\delta^{\frac{1}{2}}\mathbf{X}\mathbf{X}^H\Sigma_\delta^{\frac{1}{2}} \tag{4.13}$$

where $\mathbf{X}$ is an $N \times M$ random matrix whose entries are drawn from $\mathcal{CN}(0,1)$, and $\Sigma_\delta^{\frac{1}{2}}$ is a non-negative definite square root of the true CM, Σ_δ.

Obtaining the SCM eigenvalue density from $\varphi_\delta(\kappa)$ by naïvely using Stieltjes transforms is non-trivial due to the eigenvalue structure in $\varphi_\delta(\kappa)$. Using a computationally efficient approach [14] using the polynomial method [20], it is possible to approximate the eigenvalue density of the SCM in the attenuated case (if some of the eigenvalues are zero, only the non-zero eigenvalues used and scaled appropriately).

The N equispaced samples from $\varphi_\delta(\kappa)$ for $\kappa \in [-\frac{1}{2}, \frac{1}{2})$, $\{\lambda_1, \ldots, \lambda_N\}$ (sorted largest first) are divided into three sets:

$$\begin{aligned}
\Lambda_\delta^{\text{dist}} &= \{\lambda_i | \lambda_i > \lambda_N(1+\sqrt{\nu})^2\} \\
\Lambda_\delta^{\text{mid}} &= \{\lambda_i | \lambda_N(1+\sqrt{\nu}) < \lambda_i \leq \lambda_N(1+\sqrt{\nu})^2\} \\
\Lambda_\delta^{\text{low}} &= \{\lambda_i | \lambda_i \leq \lambda_N(1+\sqrt{\nu})\}
\end{aligned} \tag{4.14}$$

where $\nu = N/M$. $\Lambda_\delta^{\text{dist}}$ denotes the set of large eigenvalues that are "well separated" from the rest and each have a distinct contribution to the density. Sets $\Lambda_\delta^{\text{mid}}$ and $\Lambda_\delta^{\text{low}}$ denote eigenvalues with similar spreading behavior and can each be replaced by a single representative eigenvalue weighted appropriately [21]. Accordingly, the Stieltjes transform of the SCM eigenvalue density can then be written as

$$\hat{s}(z) = \sum_{\lambda_i \in \Lambda_\delta^{\text{dist}}} \frac{\frac{1}{N}}{\lambda_i \chi - z} + \sum_{\lambda_i \in \Lambda_\delta^{\text{mid}}} \frac{\frac{1}{N}}{\lambda_{\text{mid}} \chi - z} + \sum_{\lambda_i \in \Lambda_\delta^{\text{low}}} \frac{\frac{1}{N}}{\lambda_N \chi - z}$$

where $\chi = 1 - \nu - \nu z \hat{s}(z)$ and $\lambda_{\text{mid}} = \frac{\lambda_N}{2}(1 + \sqrt{\nu} + (1 + \sqrt{\nu})^2)$. Thus, all the eigenvalues in $\Lambda_\delta^{\text{mid}}$ and $\Lambda_\delta^{\text{low}}$ are replaced by λ_{mid} and λ_N respectively.

Forming the polynomial in $\hat{s}$ and solving for its roots (solved numerically, as the degree of the polynomial is almost always greater than 4), the SCM density can be obtained as

$$\widehat{\mathrm{p}}(\lambda) = \lim_{\varepsilon \to 0^+} \frac{1}{\pi} \mathrm{Im}[\hat{s}^*(\lambda + \iota\varepsilon)] \tag{4.15}$$

where $\hat{s}^*(z)$ is the appropriate root of the polynomial that has a non-negative imaginary component (since the density is always non-negative).

Fig. 4.1 shows the approximate eigenvalue density for the SCM when $N = 30$ and $M = 120$ (i.e., $\nu = \frac{1}{4}$) for different δ and the representative eigenvalues used in the Stieltjes transforms. The distributions are varied in their shapes, depending on the attenuation and approaches the Marčenko–Pastur density for large attenuation ($\delta = 1$). This variation in shape is less pronounced when the number of observations decreases (i.e., $\nu \to 1$ for the $M \geq N$ scenario) because the spreading of the eigenvalues is much higher, reducing the clustering phenomenon.

4.5 Conclusions

The asymptotic eigenvalues of noise covariance matrices in diffuse noise fields with attenuation were derived for 2D and 3D media. The presence of attenuation decreases the value of the large eigenvalues when compared to the attenuation free case, and also raises the smaller eigenvalues due to the broadening of the bandwidth of the spatial coherence function. The shape of the eigenvalue density of the finite SCM

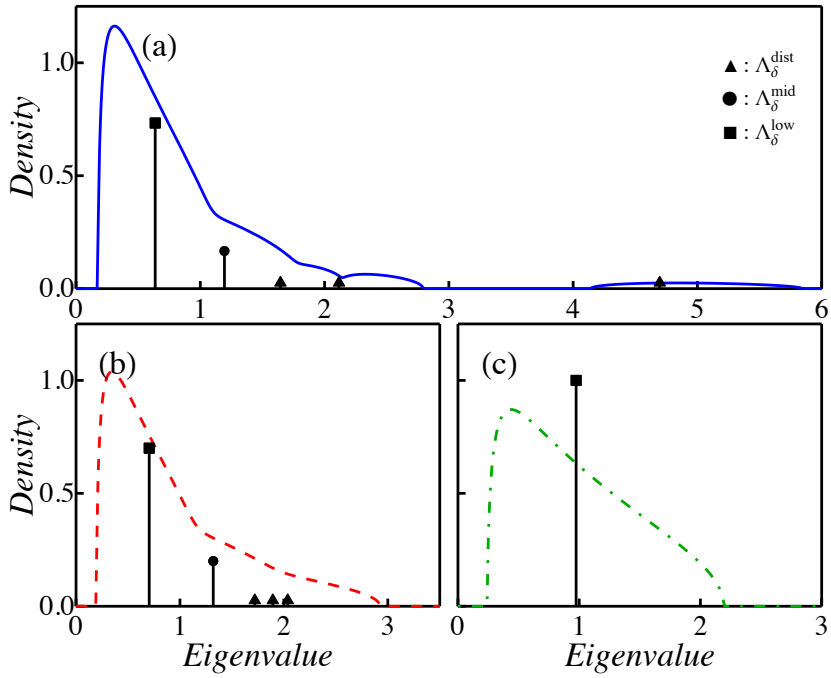

Figure 4.1: Approximate eigenvalue density of the SCM for the 2D attenuated case when the number of sensors $N = 30$, observations $M = 120$, spacing/wavelength $\beta = \frac{1}{2}$ and attenuation δ = (a) 0, (b) 0.1 and (c) 1. The markers indicate the representative eigenvalues and their weights used in the Stieltjes transform for the different groups in (4.14).

varies with attenuation and this potentially could be used to retrieve medium attenuation properties.

4.6 Acknowledgments

This work was supported by the Office of Naval Research, Grant Nos. N00014-11-1-0320 and N00014-11-1-0321.

Chapter 4, in full, is a reprint of the material as it appears in R. Menon, P. Gerstoft and W. S. Hodgkiss, "Effect of Medium Attenuation on the Asymptotic Eigenvalues of Noise Covariance Matrices", IEEE Signal Proc. Lett., **20**, 435-438 (2013). The dissertation author was the primary researcher and author of this paper.

4.A Convergence of the Error for the Bessel Sequence

The Bessel sequence, $\mathrm{J}_0(2\pi\beta n),\ n \in \mathbb{Z}$ is not absolutely summable and hence the convergence of the error term is not absolute, as in Sections 4.3.1 and 4.3.2. Convergence can be demonstrated by computing the error vector $\Sigma\mathbf{u}_i - \lambda_i\mathbf{u}_i$, where λ_i and $\mathbf{u}_i$ are the ith eigenvalue and eigenvector, as in Section II.A in [8]. Following the derivation until Eq. (15) in [8] and taking the ℓ^q-norm instead of the ℓ^2-norm, we get

$$\begin{aligned}
\|\Sigma\mathbf{u}_i - \lambda_i\mathbf{u}_i\|_q^q \leq & \frac{2}{N^{\frac{q}{2}}} \sum_{j=1}^{\frac{N}{2}} \sum_{n=j}^{N-j} |\mathrm{J}_0(2\pi\beta n)|^q \\
\leq & \frac{2}{N^{\frac{q}{2}}} \sum_{j=1}^{\frac{N}{2}} \sum_{n=-\infty}^{\infty} |\mathrm{J}_0(2\pi\beta n)|^q \\
= & N^{1-\frac{q}{2}} \sum_{n=-\infty}^{\infty} |\mathrm{J}_0(2\pi\beta n)|^q
\end{aligned} \tag{4.16}$$

$\mathrm{J}_0(2\pi\beta n)$ can be shown to have a finite ℓ^q-norm for $q > 2$ using the Hausdorff–Young inequality [22]:

Theorem 4.1 (Hausdorff–Young inequality). *If f is a function defined on a locally compact Abelian group G with measure μ, and $\mathcal{F}[f]$ its Fourier transform defined on the Pon-*

tryagin dual group $\hat{G}$ with measure $\hat{\mu}$, then for $1 \leq p \leq 2$,

$$\|\mathcal{F}[f]\|_q^{(\hat{G},\hat{\mu})} \leq \|f\|_p^{(G,\mu)} \tag{4.17}$$

such that $1/p + 1/q = 1$, where $\|\cdot\|_p^{(G,\mu)}$ denotes the norm on the Lebesgue space $\mathcal{L}^p(G,\mu)$.

Here, the function f is $\varphi_0^{\text{2D}}(\kappa)$ defined on the unit circle (G, mapped one-to-one to $\kappa \in [-\frac{1}{2}, \frac{1}{2})$) with the Lebesgue measure (μ), $\mathcal{F}[f]$ is the sequence $\mathrm{J}_0(2\pi\beta n)$ (the Fourier coefficients) defined on the set of integers ($\hat{G}$) with a counting measure ($\hat{\mu}$). Applying Theorem 4.1 and using (4.8) for $\beta \leq \frac{1}{2}$ gives:

$$\begin{aligned}\left(\sum_{n=-\infty}^{\infty} |\mathrm{J}_0(2\pi\beta n)|^q\right)^{\frac{p}{q}} &\leq \int_{-\frac{1}{2}}^{\frac{1}{2}} \left|\varphi_0^{\text{2D}}(\kappa)\right|^p \mathrm{d}\kappa = \frac{2}{\pi^p} \int_0^{\beta} \frac{\mathrm{d}\kappa}{\left(\beta^2 - \kappa^2\right)^{\frac{p}{2}}} \\ &= \pi^{-p}\beta^{1-p}\mathcal{B}\left(\frac{1}{2}, 1 - \frac{p}{2}\right)\end{aligned} \tag{4.18}$$

where $\mathcal{B}(x,y)$ is the Beta function (using the substitution $\kappa = \beta\sqrt{t}$). The RHS of (4.18) is bounded for $p < 2$ but not for $p = 2$, since $\mathcal{B}(x,y) \to \infty$ as $y \to 0$). Hence, due to Parseval's theorem, $\mathrm{J}_0(2\pi\beta n)$ cannot exist in ℓ^2 (i.e., it is not absolutely square summable) and has a finite ℓ^q-norm only if $q > 2$ (using $\frac{1}{p} + \frac{1}{q} = 1$).

Thus, the error term in (4.16) is less than $\mathcal{O}(N^{1-\frac{q}{2}})$ for $q > 2$ and approaches 0 independent of i. This argument is valid for all values of β (accounting for spatial aliasing).

Bibliography

[1] P. Kwok and P. Brandon, "Eigenvalues of noise covariance matrix of linear array in the presence of two directional interferences," *Electronics Lett.*, vol. 15, no. 2, pp. 50–51, 1979.

[2] R. O. Schmidt, "Multiple emitter location and signal parameter estimation," *IEEE Trans. Antennas Prop.*, vol. 34, no. 3, pp. 276–280.

[3] M. Wax and T. Kailath, "Detection of signals by information theoretic criteria," *IEEE Trans. Acoust., Speech, Signal Proc.*, vol. ASSP-33, no. 2, pp. 287–392, 1985.

[4] R. R. Nadakuditi and A. Edelman, "Sample eigenvalue based detection of high-dimensional signals in white noise using relatively few samples," *IEEE Trans. Signal Proc.*, vol. 56, no. 7, pp. 2625–2638, 2008.

[5] R. R. Nadakuditi and J. W. Silverstein, "Fundamental limit of sample generalized eigenvalue based detection of signals in noise using relatively few signal-bearing and noise-only samples," *IEEE J. Sel. Top. Signal Proc.*, vol. 4, no. 3, pp. 468–480, 2010.

[6] R. R. Müller, "On the asymptotic eigenvalue distribution of concatenated vector-valued fading channels," *IEEE Trans. Info. Theory*, vol. 48, no. 7, pp. 2086–2091, 2002.

[7] H. Gazzah, P. A. Regalia, and J.-P. Delmas, "Asymptotic eigenvalue distribution of block Toeplitz matrices and application to blind SIMO channel identification," *IEEE Trans. Inf. Theory*, vol. 47, no. 3, pp. 1243–1251, 2001.

[8] R. Menon, P. Gerstoft, and W. S. Hodgkiss, "Asymptotic eigenvalue density of noise covariance matrices," *IEEE Trans. Signal Proc.*, vol. 60, no. 7, pp. 3415–3424, 2012.

[9] R. Menon, P. Gerstoft, and W. S. Hodgkiss, "Cross-correlations of diffuse noise in an ocean environment using eigenvalue based statistical inference," *J. Acoust. Soc. Am.*, vol. 132, no. 5, pp. 3213–3224, 2012.

[10] P. Gerstoft, R. Menon, W. S. Hodgkiss, and C. F. Mecklenbräuker, "Eigenvalues of the sample covariance matrix for a towed array," *J. Acoust. Soc. Am.*, vol. 132, no. 4, pp. 2388–2396, 2012.

[11] X. Mestre, "On the asymptotic behaviour of the sample estimates of eigenvalues and eigenvectors of covariance matrices," *IEEE Trans. Signal Proc.*, vol. 56, no. 11, pp. 5353–5368, 2008.

[12] J. Yao, A. Kammoun, and J. Najim, "Eigenvalue estimation of parameterized covariance matrices of large dimensional data," *IEEE Trans. Signal Proc.*, vol. 60, pp. 5893–5905, nov. 2012.

[13] R. M. Gray, "On the asymptotic eigenvalue distribution of Toeplitz matrices," *IEEE Trans. Inf. Theory*, vol. 18, pp. 725–730, 1972.

[14] S. R. Tuladhar, J. R. Buck, and K. E. Wage, "Approximate eigenvalue distribution of a cylindrically isotropic noise sample covariance matrix," *IEEE Stat. Signal Proc. Workshop (Ann Arbor, Michigan)*, pp. 828–831, 2012.

[15] H. Cox, "Spatial correlation in arbitrary noise fields with application to ambient sea noise," *J. Acoust. Soc. Am.*, vol. 54, no. 5, pp. 1289–1301, 1973.

[16] W. S. Liggett Jr. and M. J. Jacobson, "Covariance of noise in attenuating media," *J. Acoust. Soc. Am.*, vol. 36, no. 6, pp. 1183–1194, 1964.

[17] G. A. Prieto, J. F. Lawrence, and G. C. Beroza, "Anelastic Earth structure from the coherency of the ambient seismic noise field," *J. Geophys. Res.*, vol. 114, p. B07303, 2009.

[18] S. C. Walker, "A model for spatial coherence from directive ambient noise in attenuating, dispersive media," *J. Acoust. Soc. Am.*, vol. 132, no. 1, pp. EL15–EL21, 2012.

[19] H. Nakahara, "Formulation of the spatial autocorrelation (SPAC) method in dissipative media," *Geophys. J. Int.*, vol. 190, pp. 1777–1783, 2012.

[20] N. R. Rao and A. Edelman, "The polynomial method for random matrices," *Foundations of Computational Mathematics*, vol. 8, no. 6, pp. 49–702, 2008.

[21] D. Paul, "Asymptotics of sample eigenstructure for a large dimensional spiked covariance model," *Statistica Sinica*, vol. 17, no. 4, pp. 1617–1642, 2007.

[22] W. Beckner, "Inequalities in Fourier analysis," *Ann. Math.*, vol. 102, no. 1, pp. 159–182, 1975.

5

EIGENVALUES OF THE SAMPLE COVARIANCE MATRIX FOR A TOWED ARRAY

It is well-known that observations of the spatial sample covariance matrix (SCM, also called the cross-spectral matrix) reveal that the ordered noise eigenvalues of the SCM decay steadily, but common models predict equal noise eigenvalues. Random Matrix Theory (RMT) is used to derive and discuss properties of the eigenvalue spectrum of the data SCM for linear arrays, with an application to ocean acoustic data. Noise on the array is considered either incoherent or propagating acoustic noise that is coherent across the array. Using conventional 3D or 2D isotropic noise models with full or snapshot-deficient observations, realizations of the SCM eigenvalues are explained using random matrix theory. Deep-water towed-array data are analyzed and it is shown that the eigenvalues of the SCM compare well with theory. It is demonstrated how RMT can be applied to study eigenvalue spectrum estimation as dependent on array properties (element spacing to wavelength ratio) and data sampling (snapshots). Apart from explaining the observed noise eigenvalue spectrum, the improved model of the eigenvalue spectrum has important applications in array signal processing.

5.1 Introduction

Often the ocean acoustic data sample covariance matrix (SCM, or cross-spectral matrix) is assumed to consist of a few large signal-plus-noise eigenvalues followed by a set of equal-value noise-only eigenvalues representing uncorrelated noise. However, it is well-known that the SCM from real data observations is characterized by steadily decaying noise-only eigenvalues.

In array processing, a common rule of thumb is that the SCM is "well-estimated" when the number of snapshots is 2–3 times the array dimension [1–3]. This depends on the type of noise and application under consideration. Often, the number of snapshots available for forming the SCM is less than this, especially for large arrays [4–10].

Using random matrix theory (RMT) [11,12] to model the statistical properties of the SCM [13–19], the eigenvalue distributions are more informative than using the expectation alone. A random matrix is a matrix-valued random variable, i.e. the elements are stochastic variables. RMT can be used to study the distribution of eigenvalues under asymptotic assumptions. Using RMT, it can be shown that the eigenvalues have well-defined statistical properties. For acoustics, RMT has found applications in, e.g., elastodynamics [20] and wave propagation and scattering in random media [21–24].

Using tools from RMT, we study the asymptotic behavior of the SCM eigenvalues under the assumption that both the sample size (snapshots) and number of sensors tends to infinity while their ratio is constant. This is in contrast to taking the mean of the SCM where sample size (snapshots) tends to infinity while number of sensors is constant. Initially, RMT was developed assuming uncorrelated observations, with the distribution of the SCM eigenvalues given by the Marčenko–Pastur (MP) density [25]. More relevant for ocean acoustic applications, both the coherent and the incoherent noise components in the observations can be modeled in the SCM via a complex Wishart distribution.

This paper discusses the SCM eigenvalue decay structure focusing on the coherent noise component using simulations and real data and thus motivates further studies using RMT. Using RMT, it might be possible to model the convergence of the SCM and design improved eigenvalue based array-processing algorithms.

5.2 Noise Covariance Matrix

The sample covariance matrix (SCM) is defined as

$$\widehat{\Sigma} = \frac{1}{M}\sum_{m=1}^{M} \mathbf{x}_m \mathbf{x}_m^H, \tag{5.1}$$

where $\mathbf{x}_m,\ m = \{1,\ldots,M\}$ is the N-element complex-valued observation vector at a particular frequency f and M the number of snapshots. We are interested in the eigendecomposition of the SCM with ordered eigenvalues $\lambda_1 \geq \ldots \geq \lambda_N$, the eigenvalue spectrum.

Using a linear model

$$\mathbf{x} = \sum_{k=1}^{K} S_k \mathbf{s}_k + \mathbf{n}_\mathrm{c} + \mathbf{n}_\mathrm{i}, \tag{5.2}$$

where $\mathbf{n}_\mathrm{i} \sim \mathcal{CN}(0, \sigma_\mathrm{i}^2\mathbf{I})$ represents incoherent noise, i.e., sensor self-noise and $\mathbf{n}_\mathrm{c} \sim \mathcal{CN}(0, \sigma_\mathrm{c}^2\Sigma_\mathrm{c})$ represents coherent propagating noise between sensors with the diagonal elements of Σ_c normalized to 1. There are $K \ll N$ discrete sources from direction $\mathbf{s}_k$ with complex amplitude S_k.

Assuming $\mathbf{s}_k$, $\mathbf{n}_\mathrm{c}$, and $\mathbf{n}_\mathrm{i}$ are uncorrelated, the covariance matrix (CM) is

$$\Sigma = E(\mathbf{x}\mathbf{x}^H) = \sum_{k=1}^{K} |S_k|^2 \mathbf{s}_k \mathbf{s}_k^H + \sigma_\mathrm{c}^2\Sigma_\mathrm{c} + \sigma_\mathrm{i}^2\mathbf{I}. \tag{5.3}$$

It is well known that the estimate Eq. (5.1) converges to Eq. (5.3) for $M \to \infty$ in a mean square sense. From this model it often is assumed that the first K eigenvalues contain signal-plus-noise and the remaining $N-K$ eigenvalues are just due to noise. In particular for incoherent noise only, i.e. $\sigma_\mathrm{c}^2 = 0$, all non-signal eigenvalues are equal-valued:

$$\lambda_j = \sigma_\mathrm{i}^2, \qquad j = K+1, \cdots, N. \tag{5.4}$$

In the remainder it is assumed $K = 0$.

We have discussed Eq. (5.2) in terms of propagating coherent noise and non-propagating sensor noise. The incoherent noise is uncorrelated between the sensors, but for certain array spacings the coherent noise also becomes uncorrelated.

The noise snapshot vector $\mathbf{n}_c + \mathbf{n}_i$ in Eq. (5.2) is modeled as a stationary, zero-mean, complex Gaussian stochastic process with covariance $\Sigma = \sigma_c^2\Sigma_c + \sigma_i^2\mathbf{I}$, i.e., $\mathbf{x}_m \sim \mathcal{CN}(0, \Sigma)$. Based on this model, the SCM $\widehat{\Sigma}$ in Eq. (5.1) is complex Wishart distributed with M degrees of freedom and covariance Σ i.e., $M\widehat{\Sigma} \sim \mathcal{W}_N(\sigma_c^2\Sigma_c + \sigma_i^2\mathbf{I}, M)$.

5.2.1 Statistical Description of Eigenvalues

The classical equal-valued eigenvalues for the incoherent noise Eq. (5.4) is derived based on the assumption that the system parameter (array size) N is constant and the number of snapshots $M \to \infty$. A full statistical description is obtained taking $v = N/M$ constant and then let $M \to \infty$ (i.e., N increases with M). This can be analyzed using RMT for incoherent or coherent [19] noise. For $v = 0$ the results correspond to the classical ensemble average.

The statistics of the SCM eigenvalues can be characterized by several distributions, such as,

1. The joint distribution of the eigenvalues [26].
2. The distribution of the largest eigenvalue λ_1. For Wishart matrices, this is described by the Tracy-Widom density (when scaled and centered appropriately) [27].
3. The distribution of the jth largest eigenvalue. [28]
4. The empirical distribution of the eigenvalues, e.g. the Marčenko–Pastur (MP) distribution in Section 5.2.2.1.

For characterizing the noise, we are concerned with the last item above.

The empirical cumulative distribution function (CDF) of the SCM eigenvalues is defined as:

$$F(\lambda) = \frac{\#\{\lambda_j \leq \lambda\}}{N}, \tag{5.5}$$

where $\#$ represents the cardinality of the set, i.e. the number of eigenvalues less than λ.

To give the empirical CDF a probabilistic interpretation, we define the random variable Λ which takes realizations from the finite set of eigenvalues $\{\lambda_1, \ldots, \lambda_N\}$ with uniform probability. Specifically, we define $\mathrm{P}\{\Lambda = \lambda_j\} = \frac{1}{N}$ for all $j = 1, \ldots, N$ and

$$\mathrm{P}\{\Lambda \leq \lambda\} = \sum_{j:\, \lambda_j \leq \lambda} \mathrm{P}\{\Lambda = \lambda_j\} = F(\lambda). \tag{5.6}$$

Thus, the distribution of a uniformly selected eigenvalue is identical to the CDF.

The eigenvalue density of the SCM is defined as

$$\mathrm{p}(\lambda) = \frac{1}{N} \sum_{j=1}^{N} \delta(\lambda - \lambda_j) = \frac{\mathrm{d}F(\lambda)}{\mathrm{d}\lambda}. \tag{5.7}$$

In the following, we examine $\mathrm{p}(\lambda)$ for coherent and incoherent noise.

5.2.2 Incoherent Noise

Array processing is typically performed under the assumption of uncorrelated noise between the sensors. Important early results in RMT are based on uncorrelated observations.

5.2.2.1 *Marčenko–Pastur (MP) Density*

For noise that appears uncorrelated between the sensors, the snapshots are distributed as $\mathbf{n}_\mathrm{i} \sim \mathcal{CN}(0, \sigma_\mathrm{i}^2 \mathbf{I})$. For $M \to \infty$ and $\nu = N/M$, $0 \leq \nu \leq 1$ constant (i.e., number of elements N increases with M), the eigenvalues of the SCM $\widehat{\boldsymbol{\Sigma}}_\mathrm{i}$ are distributed as given by the Marčenko–Pastur (MP) density [25]

$$\mathrm{p}_{\mathrm{MP}}(\lambda) = \begin{cases} \frac{\sqrt{(l_+ - \lambda)(\lambda - l_-)}}{2\pi\nu\lambda\sigma_\mathrm{i}^2} & l_- < \lambda < l_+ \\ 0 & \text{otherwise} \end{cases} \tag{5.8}$$

where $l_- = \sigma_\mathrm{i}^2(1 - \sqrt{\nu})^2$ and $l_+ = \sigma_\mathrm{i}^2(1 + \sqrt{\nu})^2$ are the upper and lower limits of the "spreading" of the eigenvalues of the SCM around the true eigenvalue σ_i^2.

Figure 5.1(a) shows the MP density, Eq. (5.8), for $\sigma_\mathrm{i}^2 = 1$ and $\nu = 1$, 1/4, and 1/25. The largest eigenvalue is about l_+ or 4, 9/4, and 36/25 times σ_i^2, illustrating how the density becomes narrower as ν decreases (M increases). For $\nu \to 0$ the MP density approaches a delta function at σ_i^2, in agreement with Eq. (5.4) for $K = 0$. The classical result for the expectation Eq. (5.3) corresponds to $\nu \to 0$.

5.2.2.2 *Simulation of Incoherent Noise Eigenvalues*

The MP density Eq. (5.8) is only valid asymptotically, but this density works well for finite array size N and snapshots M as demonstrated in Fig. 5.1(b) and 5.1(c), see also Sect. 5.2.3.5 for the snapshot-deficient case. For finite N and M, realizations of the SCM can be generated from its distribution $M\widehat{\Sigma} \sim \mathcal{W}_N(\sigma_i^2\mathbf{I}, M)$. The simulations use a constant array size $N = 64$ and computes the SCM eigenvalues for $M = N, 4N, 25N$ (or $\nu = 1, 1/4, 1/25$). Fig. 5.1(b) shows how the observed eigenvalues of the SCM are related to the MP density and Fig. 5.1(c) shows the conventional ordered display illustrating the decay of eigenvalues with eigenvalue index.

Clearly, as M increases the eigenvalues approach the constant value given in Eq. (5.4). For real arrays the observation time is finite and often $M \approx N$ as the number of snapshots is limited by requiring a stationary environment.

5.2.3 Coherent Noise

Environmental noise sources are coherent between pairs of sensors due to propagation effects in the ocean. This is in contrast to sensor noise which is incoherent and typically much lower in power than the environmental noise. Note that environmental noise may appear uncorrelated at specific element spacings (Sect. 5.2.2). For the 3D isotropic noise model this occurs at half-wavelength spacing.

5.2.3.1 *3D Isotropic Noise Eigenvalues*

For a linear array of N equidistant sensors and assuming a 3D isotropic noise field, the elements of the coherent noise covariance matrix (CM) $\sigma_c^2\Sigma_c^{3D}$ of the noise field are proportional to [19, 29] (omitting σ_c^2),

$$[\Sigma_c^{3D}]_{ij} = \operatorname{sinc}(2\beta|i-j|), \tag{5.9}$$

where $\operatorname{sinc}(x) = \sin(\pi x)/(\pi x)$ and β is the ratio of the spacing between the sensors to the wavelength under consideration ($\beta = f\Delta x/c$, where f is the frequency, Δx is the spacing between the sensors, and c is the phase speed of wave propagation in the medium). Eq. (5.9) is a symmetric Toeplitz matrix. Thus, the spatial correlations are only dependent on β and the separation $|i-j|$.

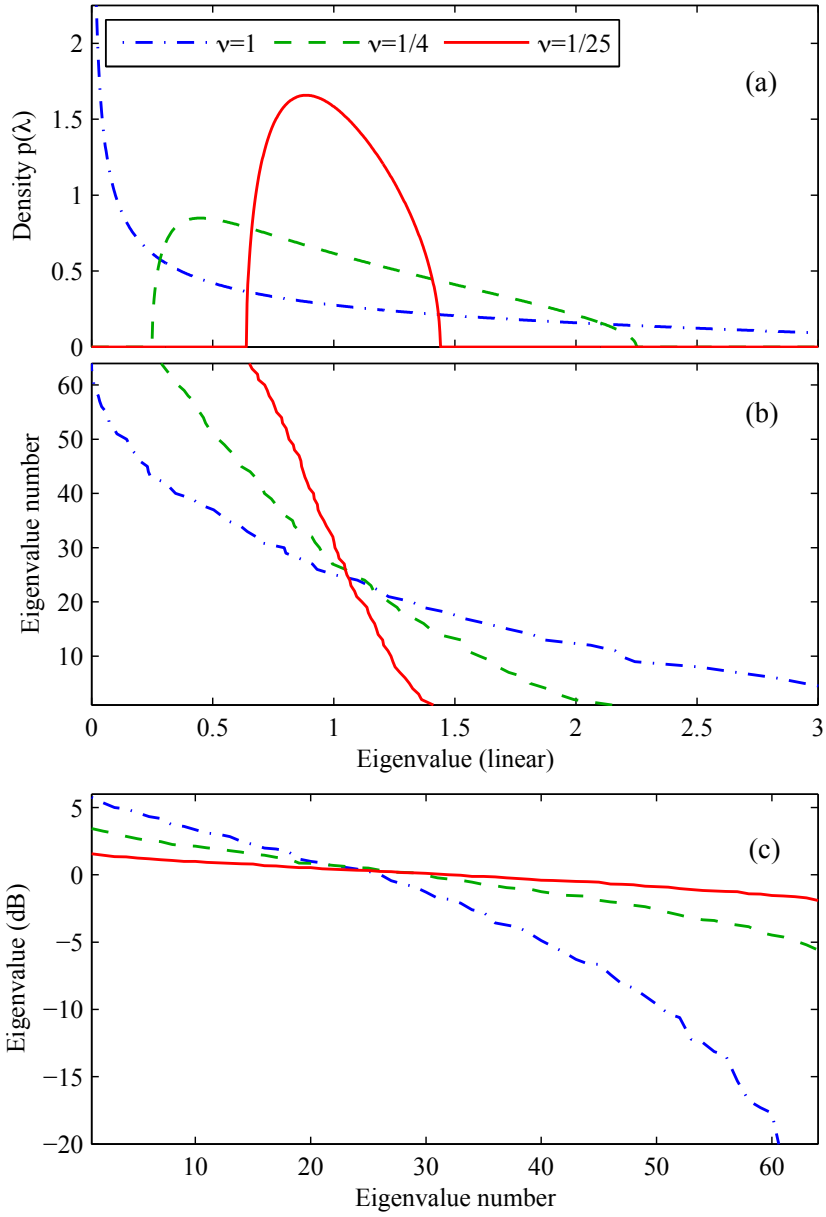

Figure 5.1: (a) Eigenvalue probability density of the incoherent noise SCM corresponding to a Marčenko–Pastur (MP) density Eq. (5.8) for $\sigma_i^2 = 1$ and $\nu = N/M = 1, 1/4, 1/25$. (b) and (c) Eigenvalues of the SCM for an array with $N = 64$ and number of snapshots M, $\nu = N/M = 1, 1/4, 1/25$. In (c) the axes are changed relative to (b) and the eigenvalue is in dB.

Asymptotically, the eigenvalues of a symmetric Toeplitz matrix are sampled from the Fourier transform of the sequence of elements that form the rows of the matrix [30]. Thus, asymptotically ($N \to \infty$), the eigenvalues of Σ_c^{3D} in Eq. (5.9) are proportional to the Fourier transform of the sinc function $\varphi(\kappa)$, which is the rectangle function:

$$\varphi(\kappa) = \frac{1}{2\beta} \operatorname{rect}\left(\frac{\kappa}{2\beta}\right), \tag{5.10}$$

where $\kappa \in [-1/2, 1/2)$ is the spatial frequency. Hence, the eigenvalues have at most two distinct values and for $\beta \leq 1/2$ just one non-zero value [19, 31], with multiplicity ratio 2β (the multiplicity ratio is the identical number of eigenvalues relative to the array dimension).

For large but finite N, an approximate formula for the eigenvalues of Σ_c^{3D} can be obtained by sampling Eq. (5.10) at N points as in Eq. (5.11) and the $1/2$ is introduced to obtain symmetry of the sampled eigenvalues.

$$\lambda_j^{3D} = \begin{cases} \frac{1}{2\beta} & \text{for} \quad \frac{j-1/2}{N} \leq 2\beta \\ 0 & \text{otherwise,} \end{cases} \tag{5.11}$$

where $j \in 1, \ldots, N$.

For $\beta < 1/2$, Σ_c^{3D} is rank deficient due to the zero eigenvalues of multiplicity ratio $(1 - 2\beta)$. For $\beta = 1/2$ (half-wavelength element spacing), $\Sigma_c^{3D} = \mathbf{I}$ and thus $\lambda_j^{3D} = 1, j = 1, \ldots, N$ and Σ_c^{3D} is full rank.

Using the CM eigenvalues, the density for the eigenvalues of the SCM can be derived [19]. Since the CM has just one distinct non-zero eigenvalue, Eq. (5.11), the density is inferred from the MP density as follows. 1) The zero CM eigenvalues remain zero in the SCM. 2) As the multiplicity ratio of the non-zero eigenvalue is 2β as opposed to 1 for the MP density, the equivalent array element to snapshot ratio becomes $\widetilde{\nu} = 2\beta\nu$. 3) Since the probability of obtaining a non-zero eigenvalue is 2β, the density of the non-zero eigenvalues is scaled by 2β. 4) Further, we need to scale the spread of the eigenvalues with $\sigma_c^2 \frac{1}{2\beta}$. This gives the coherent MP density

$$\mathrm{p}_{\mathrm{cMP}}(\lambda) = \begin{cases} 2\beta \frac{\sqrt{(\lambda_+ - \lambda)(\lambda - \lambda_-)}}{2\pi\nu\lambda\sigma_c^2} & \lambda_- < \lambda < \lambda_+ \\ (1 - 2\beta)\delta(\lambda) & \text{otherwise,} \end{cases} \tag{5.12}$$

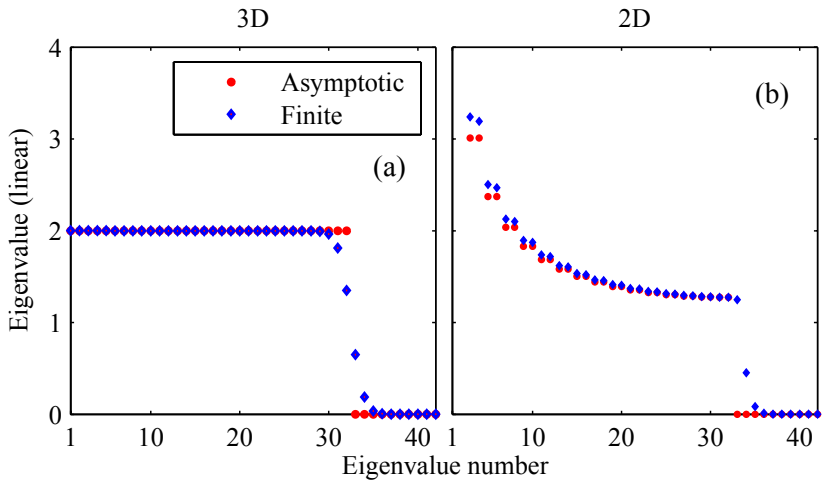

Figure 5.2: CM eigenvalues based on (a) 3D and (b) 2D isotropic noise for $\beta = 1/4$ and $N = 64$. The approximate eigenvalues [•, (a) Eq. (5.11) and (b) Eq. (5.16)] as well as the eigenvalues for a finite array (♦) are shown.

with

$$\lambda_{\pm} = \frac{\sigma_c^2}{2\beta}\left(1 \pm \sqrt{\nu}\right)^2 = \sigma_c^2\left(\sqrt{\frac{1}{2\beta}} \pm \sqrt{\nu}\right)^2 . \tag{5.13}$$

The first term in Eq. (5.12) accounts for the density due to the spreading of the non-zero eigenvalues and the second term in Eq. (5.12) is the density due to the zero eigenvalues.

5.2.3.2 *2D Isotropic Noise Eigenvalues*

For a 2D isotropic noise field [32], the coherent noise CM is proportional to

$$[\Sigma_c^{2D}]_{ij} = J_0\left(2\pi\beta|i-j|\right), \tag{5.14}$$

where J_0 is the zeroth order Bessel function. Since Σ_c^{2D} also is Toeplitz symmetric, its eigenvalues are samples from the Fourier transform of $J_0(2\pi\beta x)$:

$$\varphi(\kappa) = \mathcal{F}\left[J_0(2\pi\beta x)\right] = \frac{\mathrm{rect}(\frac{\kappa}{4\pi\beta})}{\pi\beta\sqrt{1-(\kappa/2\pi\beta)^2}} \tag{5.15}$$

where $\kappa \in [-\pi, \pi)$ is the spatial frequency. Thus, similar to the 3D case, for finite N an approximate formula for the eigenvalues is obtained by sampling Eq. (5.15) and for

$\beta \leq 1/2$, the (unsorted) eigenvalues are given by

$$\lambda_j^{2D} = \begin{cases} \frac{1}{\pi\beta\sqrt{1-|\frac{j-(N+1)/2}{N\beta}|^2}} & \text{for} \quad \left|\frac{j-(N+1)/2}{N}\right| \leq \beta \\ 0 & \text{otherwise,} \end{cases} \tag{5.16}$$

where $j \in 1, \ldots, N$. These eigenvalues come in pairs due to the symmetry around $N/2$.

Similar to the 3D case for $\beta < 1/2$, Σ_c^{2D} is rank deficient due to the zero eigenvalues of multiplicity ratio $(1 - 2\beta)$ (asymptotically, $N \to \infty$) as shown in Eq.(5.16). The first zero of the Bessel function, $J_0(2\pi\beta x)$, for $x = 1$ occurs at $\beta = 0.38$, but successive zeros do not occur at multiples of 0.38 and hence their spacing is not periodic (although the asymptotic expansion $J_0(2\pi\beta x) \approx \sqrt{\frac{1}{\pi^2\beta x}}\cos(2\pi\beta x - \pi/4)$ suggests that the zeros occur periodically for large arguments). Hence for a 2-sensor array [32], the noise on the array is uncorrelated at $\beta = 0.38$, but for larger uniformly spaced arrays, the 2D isotropic noise SCM will never be uncorrelated, even at $\beta = 0.5$.

The CM eigenvalue spectrum for 3D and 2D isotropic noise is shown in Fig. 5.2 for $N = 64$ and $\beta = 1/4$. The CM eigenvalues are computed using classical eigenvalue methods on Σ_c [♦, Eqs. (5.9) and (5.14)] and the asymptotic formulas [•, Eqs. (5.11) and (5.16)], see Fig. 5.2. For the 2D case [Fig. 5.2(b)], the large eigenvalues come in pairs and eigenvalues 1–2 are beyond the limits of the plot. For finite N, there are a number of eigenvalues near the normalized eigenvalue index 2β (these are not in pairs), defining the edge of the visible region. The visible region of the array is where the eigenvectors correspond to element-to-element phase shifts of physically propagating waves in the medium.

The SCM eigenvalue density for 2D isotropic noise is not available analytically and is obtained from simulation as demonstrated in Sect. 5.2.3.3.

5.2.3.3 *Simulation of Coherent Noise Eigenvalues*

The SCM eigenvalue densities are estimated numerically using Monte Carlo simulation and shown here for 3D and 2D isotropic noise for $N = 64$ and $\beta = 1/4$.

The SCMs are generated as $M\widehat{\Sigma}_c \sim \mathcal{W}_N(\Sigma_c, M)$ and their ordered eigenvalues are shown in Fig. 5.3(a) and 5.3(c) for a single realization. The difference in structure between the SCM eigenvalues for 3D [Fig. 5.3(a)] and 2D [Fig. 5.3(c)] isotropic noise is

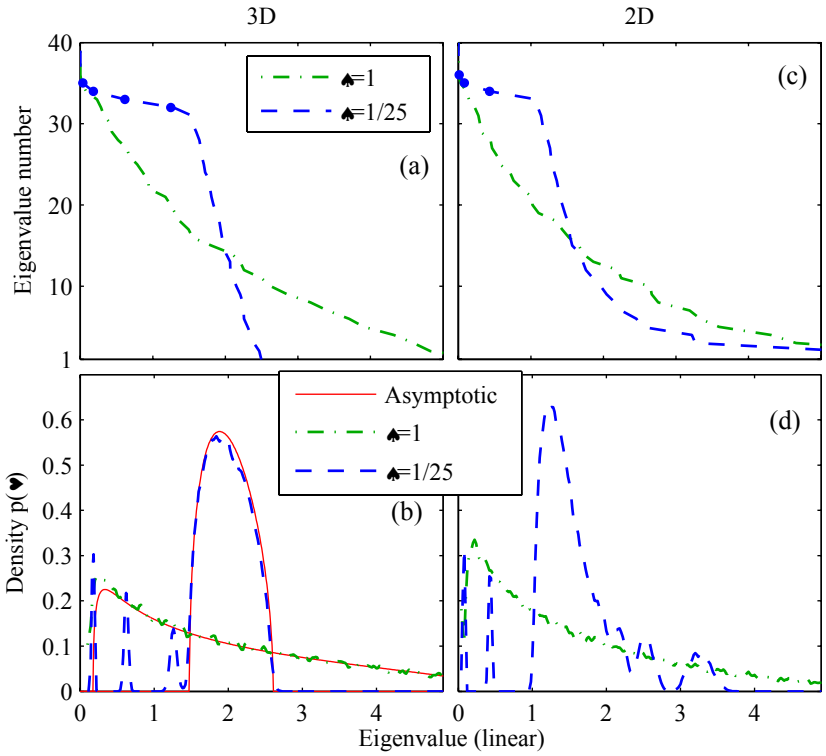

Figure 5.3: (a, c) SCM eigenvalues, and (b, d) SCM eigenvalue densities based on (a, b) 3D and (c, d) 2D isotropic noise for $\nu = N/M = 1, 1/25$. The simulation is performed with $N = 64$, $\beta = 1/4$, the SCM eigenvalues are based on one realization and the densities are obtained from 1000 Monte Carlo samples. In (b) the asymptotic densities [solid, Eq. (5.12)] are shown. In (b) and (d) the probability mass of $1 - 2\beta = 0.5$ at $\lambda = 0$ is not shown.

pronounced for $\nu = 1/25$, mirroring the shapes of their respective asymptotic formulas for the CM eigenvalues [Eqs. (5.11) and (5.16)] as shown in Fig. 5.2. However, for $\nu = 1$ (dot-dashed) the spreading of the eigenvalues looks similar and it is difficult to distinguish between the two noise fields.

The empirical eigenvalue densities are obtained from 1000 Monte Carlo samples [Figs. 5.3(b) and 5.3(d)]. The 3D asymptotic distributions [Eq. (5.12)] for both $\nu = 1$ and $\nu = 1/25$ match well the finite dimension simulated distributions [Fig. 5.3(b)].

For $\nu = 1/25$, the main density is quite sharply centered around $1/2\beta = 2$ for the 3D case as the underlying CM only has equal-valued eigenvalues of value $1/2\beta$ for $\beta \leq 1/2$, whereas the 2D density is more distributed. The localized peaks in the densities for both 3D (3 peaks) and 2D (2 peaks) observed for $\lambda < 1.5$ correspond to the "transition eigenvalues" which occur due to the finite dimension of Σ_c, the density for $\lambda < 0.05$ is suppressed. The transition eigenvalues of a single realization $\widehat{\Sigma}_c$ (•) in Figs. 5.3(a) and 5.3(c) agree well with the peaks in the densities in Figs. 5.3(b) and 5.3(d).

For 2D isotropic noise and $\nu = 1/25$, there are several localized modes at larger eigenvalues ($\lambda > 2$). These corresponds to the eigenvalue pairs 3–4 ($\lambda \approx 3.3$), 5–6 ($\lambda \approx 2.5$), and 7–8 ($\lambda \approx 2.2$) of Σ_c^{2D} in Fig. 5.2(c) (eigenvalues 1–2 have $\lambda > 5$).

5.2.3.4 *Simulation of Coherent Plus Incoherent Noise Eigenvalues*

To demonstrate the decay of the eigenvalues, we are interested in realizations of the noise SCM and their eigenvalues. Since the noise SCM is complex Wishart distributed $M\widehat{\Sigma} \sim \mathcal{W}_N(\sigma_c^2\Sigma_c + \sigma_i^2\mathbf{I}, M)$ we can generate realizations of the SCM from which the eigenvalues are determined.

This is illustrated with simulations for an array with 64 elements with noise-only data. The coherent noise is chosen a factor 200 larger than the incoherent noise, $\sigma_c^2/\sigma_i^2 = 200$. The simulations in Fig. 5.4 show the decay of the eigenvalues for all SCMs. As the number of snapshots is increased (with array size fixed, ν decreasing), the smaller eigenvalues become larger and eventually for an infinite number of snapshots the eigenvalues will approach a step function. The larger eigenvalues are dominated by the coherent noise and the smaller eigenvalues by the incoherent noise.

The location of the jump depends on β, the ratio of array spacing to wavelength.

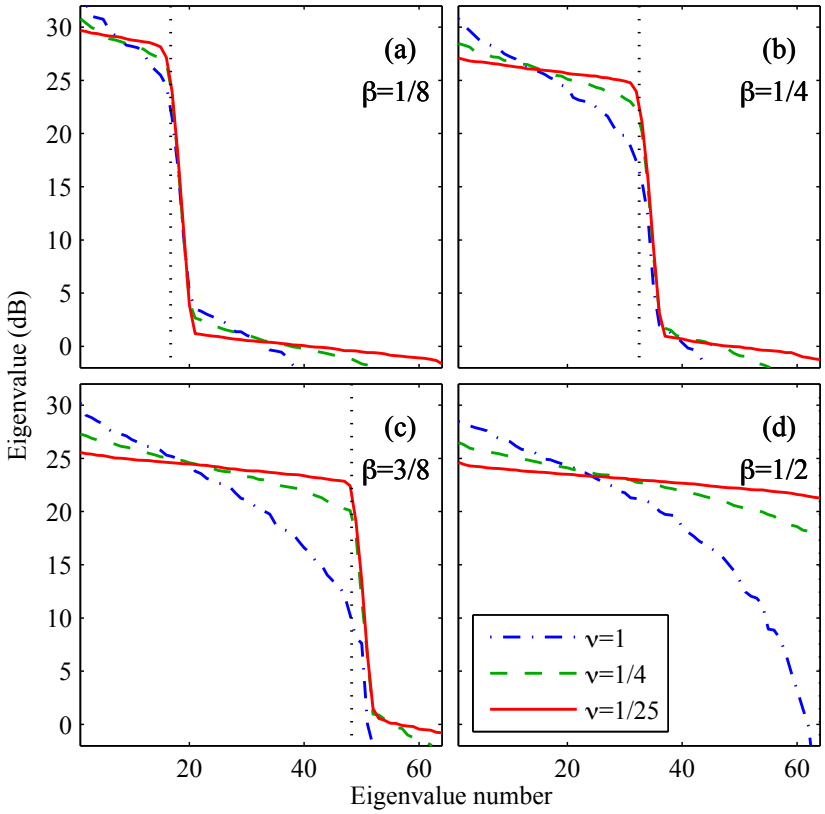

Figure 5.4: Eigenvalues of the SCM for a N =64 element array with $\sigma_c^2/\sigma_i^2 = 200$ for: (a) $\beta = 1/8$, (b) $\beta = 1/4$, (c) $\beta = 3/8$, and (d) $\beta = 1/2$. The eigenvalues are shown for an increasing number of snapshots M, where $\nu = N/M = 1$ (dash-dotted), $\nu = 1/4$ (dashed), $\nu = 1/16$ (solid). The eigenvalues are normalized with σ_i^2 and the vertical dotted line indicates the edge of the visible region.

For $\beta < 1/2$ there is a sharp drop in the vicinity of the eigenvalues corresponding to the edge of the visible region. For fewer snapshots this jump is smeared out. A smaller ratio σ_c^2/σ_i^2 reduces the jump. At $\beta = 1/2$ the coherent noise CM also is diagonal and thus identical to the classical case of only incoherent noise discussed in Sect. 5.2.2.

It is interesting to compare the largest eigenvalues of the SCM for 2D and 3D isotropic noise, see Fig. 5.5. For the same number of snapshots ($\nu = 1/4$), the largest eigenvalues for the 2D case are 4 dB larger than for the 3D case. At $\beta = 1/2$, the 2D noise CM is not diagonal (the Bessel function is not zero at $\beta = 1/2$) and eigenvalues are not similar to the incoherent case, see Fig. 5.1.

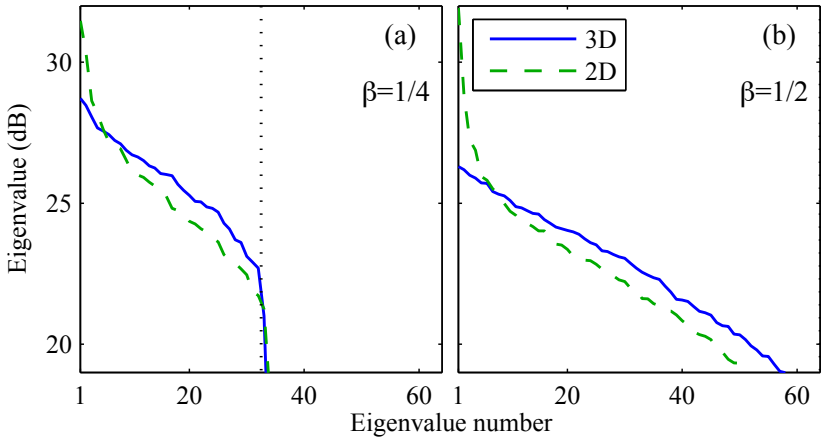

Figure 5.5: Eigenvalues of the 3D (solid) and 2D (dashed) noise SCM for a N =64 element array with $\sigma_c^2/\sigma_i^2 = 200, \nu = 1/4$ for: (a) $\beta = 1/4$ and (b) $\beta = 1/2$. The eigenvalues are normalized with σ_i^2 and the vertical dotted line indicates the edge of the visible region.

5.2.3.5 *Snapshot-deficient Case*

If there are fewer snapshot samples than sensors ($M < N$, i.e., $\nu = N/M > 1$) the SCM has at most M eigenvalues and is said to be snapshot-deficient. This often is the case for large towed arrays or arrays in dynamic environments where the number of snapshots is limited.

For the snapshot-deficient incoherent-noise SCM, i.e. $M < N$, we can apply the MP density Eq. (5.8) with $\nu = N/M$ and adding a point mass of $1 - 1/\nu$ at $\lambda = 0$ corresponding to the $N - M$ zero eigenvalues. This can be derived as follows. All snapshots are collected into an $N \times M$ observation matrix $\mathbf{X} = [\mathbf{x}_1 \dots \mathbf{x}_M]$. This gives the sample covariance matrices:

$$\widehat{\Sigma} = \frac{1}{M}\mathbf{X}\mathbf{X}^{\mathrm{H}} \quad \text{and} \quad \widehat{\Sigma}' = \frac{1}{N}\mathbf{X}^{\mathrm{H}}\mathbf{X}, \tag{5.17}$$

where $M \times M$ matrix $\widehat{\Sigma}'$ is only used in the derivation of the density, it is not a physical quantity. Since $\mathbf{X}$ is complex Gaussian $\mathcal{CN}_M(0, \sigma_i^2\mathbf{I}_N)$ then $\mathbf{X}^{\mathrm{H}}$ also is complex Gaussian $\mathcal{CN}_N(0, \sigma_i^2\mathbf{I}_M)$. Both $\widehat{\Sigma}$ and $\widehat{\Sigma}'$ will be complex Wishart distributed, as $M\widehat{\Sigma} \sim \mathcal{W}_N(\sigma_i^2\mathbf{I}_N, M)$ and $N\widehat{\Sigma}' \sim \mathcal{W}_M(\sigma_i^2\mathbf{I}_M, N)$, respectively. Thus, the snapshot-deficient incoherent-noise SCM is given by the MP density $\widehat{\Sigma}'$ matrix as if there were N "snap-

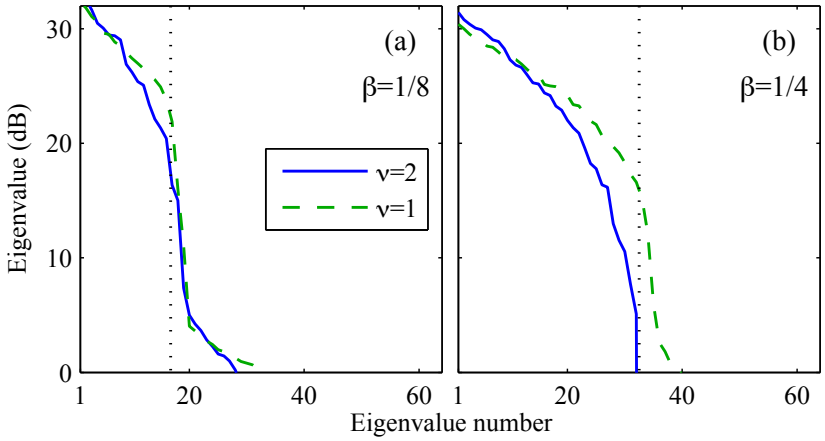

Figure 5.6: Eigenvalues of the snapshot-deficient SCM for a 64-element array for $M = 32$ (solid), i.e. $\nu = 2$, and $\sigma_c^2/\sigma_i^2 = 200$ for: (a) $\beta = 1/8$ and (b) $\beta = 1/4$. For comparison, $M = 64$ (dashed, $\nu = 1$) also is shown. The eigenvalues are normalized with σ_i^2 and the vertical dotted line indicates the edge of the visible region.

shots" and M "elements", provided a mass point of $1 - 1/\nu$ at $\lambda = 0$ is included to account for the zero eigenvalues.

For the snapshot-deficient 3D coherent-noise SCM, a simulation is used to obtain the eigenvalues. The snapshot-deficient SCM is simulated as in Sec. 5.2.3.4, but with just $M = 32$ snapshots, i.e., 32 non-zero eigenvalues, see Fig. 5.6. The eigenvalues decay faster for the snapshot-deficient SCM than when using more snapshots (solid versus dashed in Fig. 5.6). The snapshot-deficient case is further discussed in Sec. 5.3.

5.3 Experiment

The data is from a towed horizontal array during the long range acoustic communications (LRAC) experiment [33] from 10:00–11:00 UTC on 16 September 2010 in the NE Pacific in 5-km water depth. Other data periods yield similar results to those shown here. The array was towed at 3.5 knots at a depth of 200 m. The data were sampled at 2000 Hz using a nested array with each configuration having 64 channels [34]. The high frequency (HF) array had hydrophone spacing 0.375 m (design frequency $f_d = 2000$ Hz), the medium frequency (MF) array had channel spacing 0.75

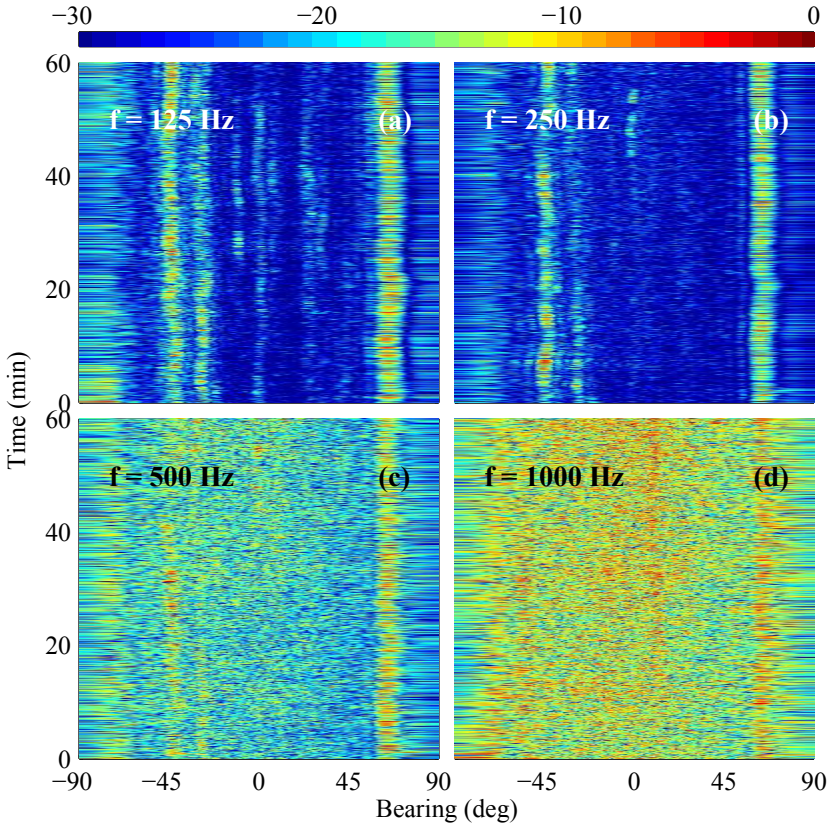

Figure 5.1: Towed array beam time series (dB) at one quarter wavelength element spacing: (a) ULF at 125 Hz, (b) LF at 250 Hz, (c) MF at 500 Hz, and (d) HF at 1000 Hz.

m (f_d = 1000 Hz), the low frequency (LF) array 1.5 m (f_d = 500 Hz), and the ultra low frequency (ULF) array 3 m (f_d = 250 Hz).

The SCMs were constructed using 4 s, 2^{13} long Fourier transforms without overlap and M =64 (ν = 1) or 864 (ν = 1/13) snapshots, with 864 snapshots corresponding to the whole hour. The beamformed time series, Fig. 5.1, is based on single snapshots and performed at one quarter wavelength element spacing. The broad arrival at 60–75° is from the towship (R/V Melville). Apparently, the two arrivals at −45° and −30° come from distant transiting ships, although a log of ships in the area was not kept. Overall, the beam time series shows little change with time.

Figure 5.2 shows the eigenvalues of the SCM at selected values of β for the four arrays. Due to the low sampling frequency (2000 Hz), the HF array only can be used up to β = 1/4 (1000 Hz). All eigenvalues are based on one hour observations, meaning

that for $M = 64$ the eigenvalues are averaged over 13 SCM eigenvalues. The first few eigenvalues for each SCM likely are due to the distant transiting ships and noise from the towship, as seen in the beam time series (Fig. 5.1). The eigenvalues drop sharply above $2\beta(N-1)+1$ (vertical dotted line) as predicted by theory, and indicates that the coherent noise is stronger than the incoherent noise. The eigenvalues of the SCM of the LF and ULF arrays show a similar behavior as the MF and HF arrays though with less strong transition between the two eigenvalue regimes.

Figure 5.2 shows that the eigenvalues depend on β. As β increases, all the eigenvalue spectra become more extended and at $\beta = 0.5$ (half wavelength spacing) the SCM ideally should become diagonal with eigenvalues that approximately are all equal.

Comparing the four arrays at $\beta = 1/8$, first column in Fig. 5.2, shows that the higher eigenvalue numbers (containing mostly incoherent noise) are relatively larger at low frequencies. At half-wavelength spacing ($\beta = 1/2$, last column in Fig. 5.2), all eigenvalues remain large for the three arrays, except when using a relatively small number of snapshots ($M = N$).

The observed and modeled noise eigenvalues are compared in Fig. 5.3. It is important to realize that there is towship radiated noise as well as broadband signatures from several distant ships arriving at the array, especially at low frequencies, see Fig. 5.1. These "signals" are among the largest eigenvalues extracted from the data, see Eq. (5.2). Therefore, we arbitrarily select to only match the noise from eigenvalue 10 and vary the ratio of coherent to incoherent noise σ_c^2/σ_i^2, see Fig. 5.3. For the HF array, the match is quite good and the transition region is also well-determined. For the LF array, the match is less good, likely because not all dominant noise sources are modeled. Before these noise sources are understood, whether the noise field is 2D or 3D cannot be determined.

For large arrays, the SCM often is snapshot-deficient. The snapshot-deficient eigenvalues for the towed array data (Fig. 5.4) compare well with the simulations in Fig. 5.6. How well the coherent noise eigenvalues are estimated depends on β relative to the number of snapshots M. For small values of β there might besufficient snapshots so the coherent noise eigenvalues are relatively well estimated. An important question

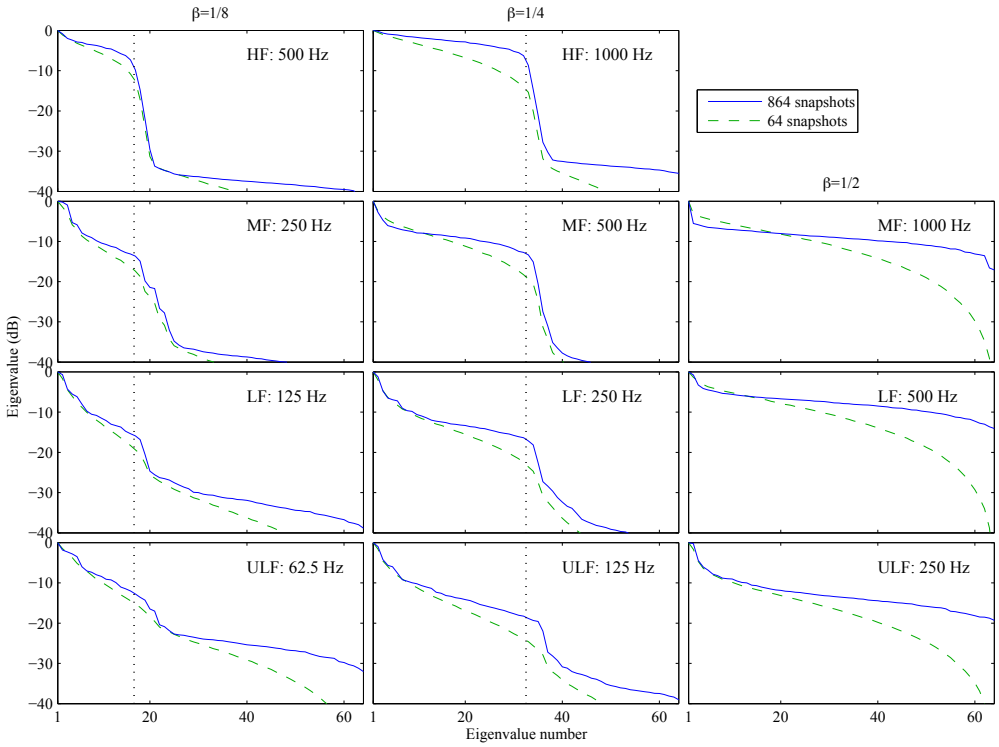

Figure 5.2: Eigenvalues of the towed array SCM for HF array (1st row, $\beta = 1/8, 1/4$), MF array (2nd row, $\beta = 1/8, 1/4, 1/2$), LF array (3rd row, $\beta = 1/8, 1/4, 1/2$), and ULF array (4th row, $\beta = 1/8, 1/4, 1/2$). The eigenvalues are based on 64 ($\nu = 1$, dashed) and 864 ($\nu = 13$, solid) snapshots. The eigenvalues are normalized with the largest eigenvalue and the vertical dotted line indicates the edge of the visible region, β is the element spacing to wavelength ratio.

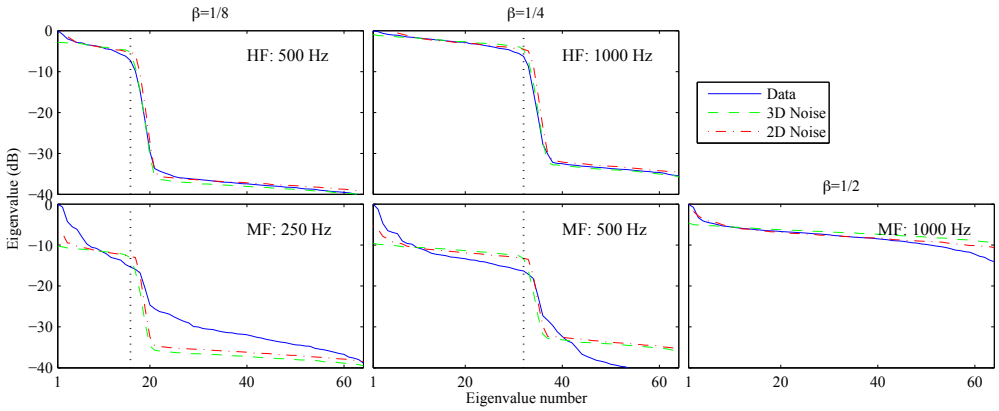

Figure 5.3: Comparison of observed and modeled eigenvalues. Eigenvalues of the towed array SCM (solid) and modeled eigenvalues 3D (dashed) and 2D (dash-dotted) for HF array (1st row, $\beta = 1/8, 1/4$) and LF array (2nd row, $\beta = 1/8, 1/4, 1/2$). The observed eigenvalues are based on 864 ($\nu = 13$, solid) snapshots, the modeled eigenvalues use a ratio $\sigma_c^2/\sigma_i^2 = 700$ for HF array and $\sigma_c^2/\sigma_i^2 = 100$ for LF array. The eigenvalues are normalized with the largest eigenvalue and the vertical dotted line indicates the edge of the visible region, β is element spacing to wavelength ratio.

is how eigenvalue based beamforming performs for this case, but this is beyond the scope of this paper.

From all of the SCM eigenvalue spectra [Fig. 5.5(a) and 5.5(c)] we obtain histograms of the eigenvalues [Fig. 5.5(b) and 5.5(d)] corresponding to the empirical eigenvalue density, Eq. (5.7). Each SCM is normalized by the largest eigenvalue so that in the histograms the largest eigenvalues correspond to "signal" eigenvalues. The histograms are multi-modal corresponding to coherent and incoherent noise, as can also be seen from 2nd row in Fig. 5.2.

5.4 Conclusion

Eigenvalue spectra of the sample covariance matrix (SCM, also called the cross-spectral matrix) have been examined for both synthetic and real data. The ordered eigenvalues decay steadily as predicted using random matrix theory (RMT). Using tools from RMT, we study the asymptotic behavior of the SCM eigenvalues under the assumption that both the sample size and number of sensors tend to infinity while their

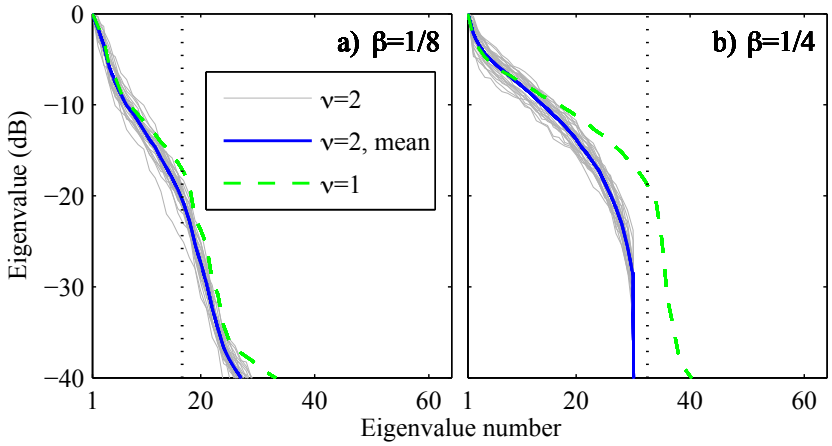

Figure 5.4: Eigenvalues of the MF towed array snapshot-deficient SCM with $M = 32$ ($\nu = 2$) for several realizations (thin lines) for (a) $\beta = 1/8$ and (b) $\beta = 1/4$ (i.e., frequencies 500 and 1000 Hz). Average of these eigenvalues (solid) and eigenvalues of the SCM (dashed) with $M = N = 64(\nu = 1)$ also are shown. The eigenvalues are normalized with the largest eigenvalue and the vertical dotted line indicates the edge of the visible region.

ratio is constant. This is in contrast to taking the mean of the SCM where sample size tends to infinity while number of sensors is constant.

The noise observed by an equally-spaced line array has been modeled as the sum of an incoherent component and a stronger coherent component corresponding to propagating noise. The coherent component is modeled as 3D or 2D isotropic noise corresponding to a sinc or a zeroth-order Bessel covariance matrix. Eigenvalues of these were examined and both matrices were singular for element spacing to wavelength ratios less than 1/2, causing a sharp drop in the eigenvalues which is related to the edge of the visible region. Realizations of synthetic SCMs were drawn from the complex Wishart distribution in numerical simulations from which both eigenvalue spectra and densities were estimated.

Simulated and deep-water towed-array noise data SCMs clearly show the strong jump in power level at the edge of the visible region. Apart from this jump, the SCM eigenvalues decay steadily as predicted by theory. Snapshot deficient and well-estimated SCMs were considered.

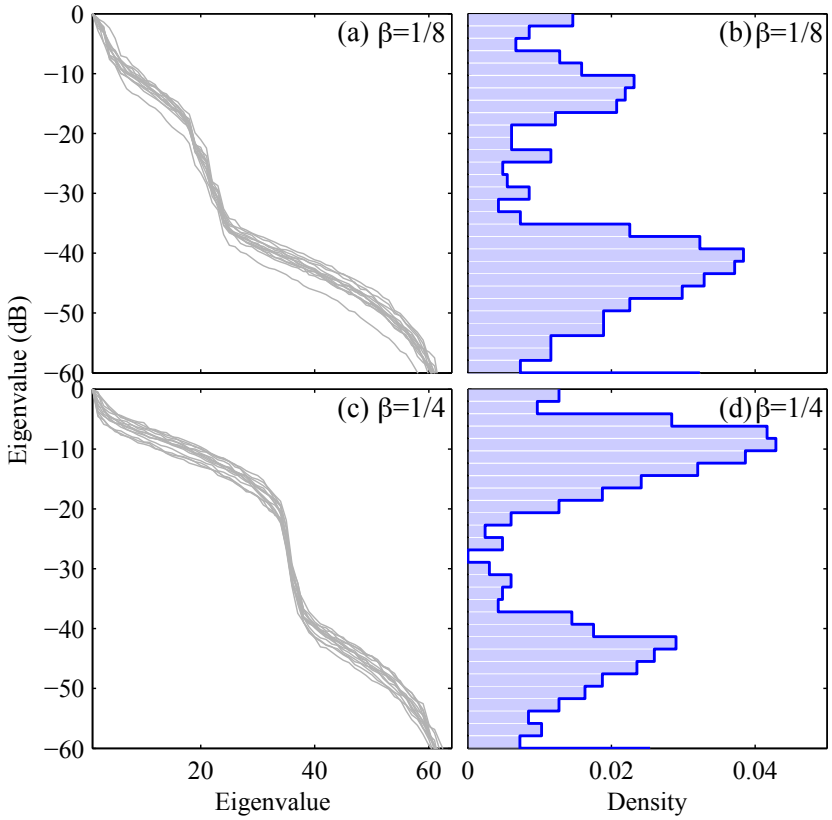

Figure 5.5: (a, c): Eigenvalues of the MF towed array SCM with $M = 64$ ($\nu = 1$) for 13 realizations for (a, b) $\beta = 1/8$ (250 Hz) and (c, d) $\beta = 1/4$ (500 Hz). (b, d): The normalized histograms of all of the eigenvalues.

5.5 Acknowledgment

The Office of Naval Research, Grant Nos. N00014-11-1-0321 and N00014-11-1-0320 supported this work.

Chapter 5, in full, is a reprint of the material as it appears in P. Gerstoft, R. Menon, W. S. Hodgkiss and C. F. Meckelenbräuker, "Eigenvalues of the sample covariance matrix for a towed array", J. Acoust. Soc. Am., **132** (4), 2388-2396 (2012). This paper is based on Chapter 3 and the dissertation author contributed significantly to the research and material that forms the basis of this chapter.

Bibliography

[1] B. D. Carlson, "Covariance matrix estimation errors and diagonal loading in adaptive arrays," IEEE Trans. Aerosp. and Electron. Syst. **24**, 397–401 (1988).

[2] I. S. Reed, J. D. Mallett, and L. E. Brennan, "Rapid convergence rate in adaptive arrays," IEEE Trans. Aerosp. and Electron. Syst. **AES-10**, 853–863 (1974).

[3] D. E. Grant, J. H. Gross, and M. Z. Lawrence, "Cross-spectral matrix estimation effects on adaptive beamforming," J. Acoust. Soc. Am. **98**, 517–524 (1995).

[4] A. B. Baggeroer and H. Cox, "Passive sonar limits upon nulling multiple moving ships with large aperture arrays," in *Asilomar Conf. on Sign., Syst., and Comp.*, volume 1, 103–108 (1999).

[5] H. Song, W. A. Kuperman, W. S. Hodgkiss, P. Gerstoft, and J. Kim, "Null broadening with snapshot-deficient covariance matrices in passive sonar," IEEE J. Oceanic Eng. **28**, 250–261 (2003).

[6] T. C. Yang, "Motion compensation for adaptive horizontal line array processing," J. Acoust. Soc. Am. **113**, 245–260 (2003).

[7] P. Gerstoft, W. S. Hodgkiss, W. A. Kuperman, H. C. Song, M. Siderius, and P. L. Nielsen, "Adaptive beamforming of a towed array during a turn," IEEE J. Oceanic Eng. **28**, 44–54 (2003).

[8] D. Tollefsen, S. E. Dosso, and M. J. Wilmut, "Matched-field geoacoustic inversion with a horizontal array and low-level source," J. Acoust. Soc. Am. **120**, 221–230 (2006).

[9] J. S. Rogers and J. L. Krolik, "Time-varying spatial spectrum estimation with a maneuverable towed array," J. Acoust. Soc. Am. **128**, 3543–3553 (2010).

[10] S. D. Somasundaram and N. H. Parsons, "Evaluation of robust Capon beamforming for passive sonar," IEEE J. Oceanic Eng. **36**, 686–695 (2011).

[11] M. L. Mehta, *Random Matrices*, 3rd edition (Academic Press,) (2004), Chapter 1.

[12] A. Edelman and N. R. Rao, "Random matrix theory," Acta Numerica **14**, 233–297 (2005).

[13] X. Mestre, "On the asymptotic behavior of the sample estimates of eigenvalues and eigenvectors of covariance matrices," IEEE Trans. Signal Proc. **56**, 5353–5368 (2008).

[14] X. Mestre and M. A. Lagunas, "Modified subspace algorithms for DoA estimation with large arrays," IEEE Trans. Signal Proc. **56**, 598–614 (2008).

[15] B. A. Johnson, Y. I. Abramovich, and X. Mestre, "MUSIC, G-MUSIC, and maximum-likelihood performance breakdown," IEEE Trans. Signal Proc. **56**, 3944–3958 (2008).

[16] R. R. Nadakuditi and A. Edelman, "Sample eigenvalue based detection of high-dimensional signals in white noise using relatively few samples," IEEE Trans. Signal Process. **56**, 2625–2638 (2008).

[17] R. R. Nadakuditi and J. W. Silverstein, "Fundamental limit of sample generalized eigenvalue based detection of signals in noise using relatively few signal-bearing and noise-only samples," IEEE J. selected topics in Signal Proc. **4**, 468–480 (2010).

[18] J. R. Buck and K. E. Wage, "Modeling dominant mode rejection beamformer notch depth using random matrix theory," J. Acoust. Soc. Am. **130**, 2377 (2011).

[19] R. Menon, P. Gerstoft, and W. S. Hodgkiss, "Asymptotic eigenvalue density of noise covariance matrices," IEEE Trans. Signal Proc. **60**, 3415–3424 (2012).

[20] R. L. Weaver, "Spectral statistics in elastodynamics," J. Acoust. Soc. Am. **85**, 1005–1013 (1989).

[21] R. R. Müller, "A random matrix model of communication via antenna arrays," IEEE Trans. Info. Theory **48**, 2495–2506 (2002).

[22] A. Aubry and A. Derode, "Multiple scattering of ultrasound in weakly inhomogeneous media: Application to human soft tissues," J. Acoust. Soc. Am. **129**, 225–233 (2011).

[23] S. E. Skipetrov and A. Goetschy, "Eigenvalue distributions of large euclidean random matrices for waves in random media," J. Phys. A: Math. Theor. **44**, 065102 (2011).

[24] R. Menon, P. Gerstoft, and W. S. Hodgkiss, "Passive acoustic monitoring using random matrix theory," in *IEEE Stat. Signal Proc. workshop*, 101–105 (Ann Arbor, Michigan, USA) (2012).

[25] V. A. Marčenko and L. A. Pastur, "Distributions of eigenvalues of some sets of random matrices," Math. Sb. **72**, 507–536 (1967).

[26] T. W. Anderson, *An introduction to multivariate statistical analysis,* Chapter 13 (Wiley Series in Probability and Statistics, 3rd ed. Hoboken, NJ: Wiley-Interscience,) (2003).

[27] C. A. Tracy and H. Widom, "Level-spacing distributions and the Airy kernel," Comm. Math. Phys. **159**, 151–174 (1994).

[28] A. Zanella, M. Chiani, and M. Z. Win, "On the marginal distribution of the eigenvalues of Wishart matrices," IEEE Transactions on Communications **57**, 1050–1060 (2009).

[29] H. Cox, "Spatial correlation in arbitrary noise fields with application to ambient sea noise," J. Acoust. Soc. Am. **54**, 1289–1301 (1973).

[30] R. M. Gray, "Toeplitz and circulant matrices: A review," Found. Trends. Comm. Inf. Theory **2**, 155–239 (2006).

[31] D. Slepian, "Prolate spheroidal wave functions, fourier analysis, and uncertainty — v: The discrete case," The Bell System Technical Journal **57**, 1271–1430 (1978).

[32] B. F. Cron and C. H. Sherman, "Spatial-correlation functions for various noise models," J. Acoust. Soc. Am. **34**, 1732–1736 (1962).

[33] H. C. Song, S. Cho, T. Kang, W. S. Hodgkiss, and J. R. Preston, "Long-range acoustic communication in deep water using a towed array," J. Acoust. Soc. Am. **129**, EL71–EL75 (2011).

[34] K. M. Becker and J. R. Preston, "The ONR five octave research array (FORA) at Penn State," in *OCEANS 2003*, volume 5, 2607–2610 (2003).

6

CROSS-CORRELATIONS OF DIFFUSE NOISE IN AN OCEAN ENVIRONMENT USING EIGENVALUE BASED STATISTICAL INFERENCE

Cross-correlations of diffuse noise fields can be used to extract environmental information. The influence of directional sources (usually ships), often results in a bias of the travel time estimates obtained from the cross-correlations. Using an array of sensors, insights from random matrix theory on the behavior of the eigenvalues of the sample covariance matrix (SCM) in an isotropic noise field are used to isolate the diffuse noise component from the directional sources. A sequential hypothesis testing of the eigenvalues of the SCM reveals eigenvalues dominated by loud sources that are statistical outliers for the assumed diffuse noise model. Travel times obtained from cross-correlations using only the diffuse noise component (i.e., by discarding or attenuating the outliers) converge to the predicted travel times based on the known array sensor spacing and measured soundspeed at the site and are stable temporally (i.e., unbiased estimates). Data from the Shallow Water 2006 experiment demonstrates

the effectiveness of this approach and that the SNR builds up as the square root of time, as predicted by theory.

6.1 Introduction

Over the past decade, there has been significant interest in retrieving information from diffuse, multiply scattered and refracted waves in an environment. It was demonstrated, both theoretically and experimentally [1–5], that temporal cross-correlations of a diffuse noise field recorded on a pair of receivers yielded the Green's function between those two points. It also is possible to image remote areas of the ocean [6–10] and the interior of the earth [11–13] using diffuse noise fields, as opposed to using controlled active sources which are both expensive and limited in resolution.

The ocean noise field has two primary components—a rich and varied background diffuse noise field due to wind, breaking waves, biological activities, distant shipping, and a highly directional (and often stronger) noise field due to ships and other similar anthropogenic activities in the vicinity of the observing sensors. Depending on whether one wishes to monitor the changes in the environment, or the movement of the sources, the two components of the noise field either can be beneficial or a deterrent. A challenge in using ocean noise is separating these two components reliably.

For an N element linear hydrophone array, the sample covariance matrix (SCM) is formed in the frequency domain from M snapshot vectors (i.e., the Fourier coefficients of the data observation vector at a frequency f), $\mathbf{x}_m(f),\ m = 1,\ldots,M$ as

$$\widehat{\mathbf{R}}(f) = \frac{1}{M}\sum_{m=1}^{M} \mathbf{x}_m(f)\mathbf{x}_m^H(f), \tag{6.1}$$

and its eigendecomposition gives the eigenvalues $\hat{\lambda}_1(f) \geq \cdots \geq \hat{\lambda}_N(f)$ and eigenvectors $\hat{\mathbf{v}}_1(f),\ldots,\hat{\mathbf{v}}_N(f)$. The time domain cross-correlation of the data from the ith and jth hydrophones across the entire bandwidth is obtained as:

$$\widehat{C}_{ij}(t) = \mathcal{F}^{-1}\left[\widehat{\mathbf{R}}_{ij}(f)\right] \tag{6.2}$$

where t denotes the correlation time, and $\mathcal{F}^{-1}$ denotes an inverse Fourier transform (henceforth, the dependence on f is dropped unless necessary).

When the noise field is diffuse, the cross-correlation can be used as a proxy for the Green's function of the environment (which is unknown) shaped by the spectrum of the noise field. Hence, the location of the peak of the cross-correlation gives the travel time which typically corresponds to the direct path propagation between the hydrophones.

It was shown experimentally [6] that in order to obtain stable travel times for a ship dominated noise field, the cross-correlations must be averaged over ship tracks which pass through the end-fire region of a pair of hydrophones. Performing the cross-correlations over much shorter time periods introduces biased travel times, because the directional nature of the noise field results in travel times that generally are less than that for the direct path between the hydrophones [14,15]. This results in requiring long observation times to obtain stable estimates of the travel times

In this article, the focus is on obtaining stable cross-correlations from an array of sensors without interference from loud sources, by effectively discarding or attenuating the contributions from the directional noise field (Sec. 6.4). This is achieved by drawing on insights from random matrix theory (RMT) on the behavior of the eigenvalues (Sec. 6.2) of the SCM, which then is used in a statistical hypothesis testing framework (Sec. 6.3).

RMT, which has its roots in nuclear physics [16], is a mathematical tool that allows one to study the eigenvalue densities of random matrices in the asymptotic limit as the matrix size increases. It has diverse applications in a wide variety of fields such as statistics [17,18], signal processing [19–25], ocean acoustics [23,26–29], information theory and wireless communications [30, 31], elastodynamics [32], wave propagation and scattering in random media [33–35].

Recently, the asymptotic eigenvalue densities of the SCM for a 3D isotropic noise field were derived using RMT [23]. Here, we assume the diffuse background noise field in an ocean environment to be isotropic and use these results to distinguish the eigenvalues due to loud, directional sources (e.g. nearby ships) in the data from those of the background noise using hypothesis testing. Prior related work include model order estimation for signals in white noise using RMT combined with an information theoretic criterion [21] and eigenvalue based sequential hypothesis testing

in white and colored noise [17, 22]. The contribution of this article is in adapting the sequential testing to diffuse ocean noise fields, especially when the SCM inherently is rank deficient (see Sec. 6.2.2), and its application in noise processing.

The isotropic noise model primarily is chosen because the known analytical results [23], readily can be related to features observed in data (see Sec. 6.4). In practice, any reasonable physical noise model can be used (see Sec. 6.5 for a brief discussion) and the advantage of using simple analytical noise models is that one can process the data without having to know anything about the environment (e.g. water depth, seafloor characteristics, etc.).

6.1.1 Notations and Definitions

1. The term *eigenvalue density* (probability density of the eigenvalues) is often used, and is defined for any $N \times N$ Hermitian matrix $\mathbf{A}$ with eigenvalues $\{a_1, \ldots, a_N\}$ as
$$\mathrm{p}_{\mathbf{A}}(x) = \frac{1}{N}\sum_{n=1}^{N} \delta(x - a_n) = \frac{d}{dx}\mathrm{P}_{\mathbf{A}}(x), \tag{6.3}$$
where $\mathrm{P}_{\mathbf{A}}(x)$ is the empirical cumulative distribution (ECD) of the eigenvalues, defined as
$$\mathrm{P}_{\mathbf{A}}(x) = \frac{\#\{a_n \leq x\}}{N}, \tag{6.4}$$
and $\#$ denotes the cardinality of the set.

2. As $N \to \infty$, the ECD of the eigenvalues, $\mathrm{P}_{\mathbf{A}}(x)$ converges almost surely to a well defined distribution $\mathrm{P}(x)$ [36] and the corresponding density function, $\mathrm{p}(x)$ is referred to as the *asymptotic eigenvalue density*.

3. The dimensions of any covariance matrix (CM) $\mathbf{A}$, unless made explicit, are taken to be $N \times N$. $\mathbf{A}_\infty$ denotes $\lim_{N\to\infty} \mathbf{A}_N$. Similarly, any SCM $\hat{\mathbf{A}}$, unless otherwise stated, is taken to be such that $M\hat{\mathbf{A}} \sim \mathcal{W}(\mathbf{A}, M)$, i.e., $M\hat{\mathbf{A}}$ is complex Wishart distributed with M degrees of freedom and true CM $\mathbf{A}$. $\hat{\mathbf{A}}_\infty$ denotes $\lim_{N,M\to\infty} \hat{\mathbf{A}}_N$, with $N/M = \nu$.

4. The term *loud source* is used generically to mean discrete sources or interferers in the environment, which in general are louder than the diffuse background

noise field and possibly could bias the cross-correlations because of their spatial compactness (also see Sec. 6.3.1.1).

6.2 Background

6.2.1 Statistical Model for the SCM

The mth snapshot vector, $\mathbf{x}_m$, is modeled as

$$\mathbf{x}_m = \mathbf{s}_m + \mathbf{n}_m, \tag{6.5}$$

where $\mathbf{s}_m \sim \mathcal{CN}(0, \mathbf{S})$ is a circular complex normal distributed directional noise vector from loud sources in the environment with a CM $\mathbf{S}$ and $\mathbf{n}_m \sim \mathcal{CN}(0, \Sigma)$ is a Gaussian diffuse noise vector with a CM Σ. From the independence of $\mathbf{s}_m$ and $\mathbf{n}_m$, the true CM of $\mathbf{x}_m$ then is

$$\mathbf{R} = \mathbf{S} + \Sigma, \tag{6.6}$$

and the SCM in Eq. (6.1) is complex Wishart distributed with M degrees of freedom and true CM $\mathbf{R}$, i.e., $M\widehat{\mathbf{R}} \sim \mathcal{W}(\mathbf{R}, M)$.

For the purposes of this paper, to model the effect of a few loud sources, we assume that the rank of $\mathbf{S}$, say K, is small compared to the rank of Σ i.e.,

$$K = \text{rank}(\mathbf{S}) \ll \text{rank}(\Sigma) \tag{6.7}$$

and that the K non-zero eigenvalues of $\mathbf{S}$ are all larger than the eigenvalues of Σ and manifest in the K largest eigenvalues of the SCM. Note that the effect of a source will be spread across multiple eigenvalues and eigenvectors if the source is moving and the observation time is not short enough to consider it to be stationary [37] or if multiple sources are present and their replica vectors are not orthogonal [38]. Hence, a direct correspondence between a particular eigenvalue and a particular loud source might not be possible.

The objective is to separate the components of the SCM $\widehat{\mathbf{R}}$ based on its eigen-

values and eigenvectors as

$$\begin{aligned}\widehat{\mathbf{R}} &= \sum_{k=1}^{K} \hat{\lambda}_k \hat{\mathbf{v}}_k \hat{\mathbf{v}}_k^H + \sum_{k=K+1}^{N} \hat{\lambda}_k \hat{\mathbf{v}}_k \hat{\mathbf{v}}_k^H \\ &= \widehat{\mathbf{R}}_s + \widehat{\mathbf{R}}_n, \end{aligned} \tag{6.8}$$

where $\widehat{\mathbf{R}}_s$ is the directional noise component and $\widehat{\mathbf{R}}_n$ is the diffuse noise component. The eigenvalues of $\widehat{\mathbf{R}}_s$, namely $\hat{\lambda}_1, \ldots, \hat{\lambda}_K$ (and the eigenvectors), also contain a diffuse noise component in addition to the directional noise component and hence the separation of $\widehat{\mathbf{R}}$ exactly into $\widehat{\mathbf{S}}$ and $\widehat{\Sigma}$ is not possible.

In the following section, we review the case when $\mathbf{R} = \mathbf{R}_n = \Sigma$, and the true noise CM Σ is due to a spatially isotropic noise field.

6.2.2 Relevant Results for Spatially Isotropic Noise Fields

An isotropic noise field consists of random waves propagating towards the array from all directions. The spatial coherence function of the noise recorded on two sensors in a 3D isotropic noise field is [39, 40]

$$\Gamma = \mathrm{sinc}(2\beta), \tag{6.9}$$

where $\mathrm{sinc}(x) = \sin(\pi x)/(\pi x)$ and β is the ratio of the spacing between the sensors to the wavelength under consideration ($\beta = fd/c$, where f is the frequency, d is the spacing between the sensors, and c is the speed of wave propagation in the medium). For a linear array of N equidistant sensors, the elements of the CM of the noise field (normalized to unit power on each sensor) are given by

$$\Sigma_{ij} = \mathrm{sinc}\left(2\beta|i-j|\right), \tag{6.10}$$

which is a symmetric Toeplitz matrix. Thus, the spatial correlations are only dependent on β (or equivalently, on f) and the separation $|i-j|$.

6.2.2.1 *Asymptotic Eigenvalues of the Isotropic Noise CM*

It has been shown that the eigenvalues of an infinite dimensional Toeplitz matrix constructed from sequences in ℓ_1 (absolutely summable), with a Fourier series also

in ℓ_1 (called Wiener class Toeplitz matrices) are related to the said Fourier series [41]. Although the sinc sequence is not absolutely summable, the result still holds [23] and the asymptotic eigenvalues of Σ_∞ from Eq. (6.10) were derived for all β.

In Ref. [23], it is shown that there are at most two distinct eigenvalues (with multiplicities) for all β, given by

$$\Lambda_1 = \frac{q+1}{2\beta} \text{ and } \Lambda_2 = \frac{q}{2\beta}, \tag{6.11}$$

with $q \in \{0, 1, \dots\}$ such that $q < 2\beta \leq q + 1$, and the respective multiplicity ratios are given by

$$\xi_1 = 2\beta - q \text{ and } \xi_2 = q + 1 - 2\beta. \tag{6.12}$$

A key result here is the fact that the CM is rank deficient for $\beta < 1/2$, even when $M > N$ because $\Lambda_2 = 0$. In other words, the rank deficiency is not due to insufficient snapshots, but due to the nature of the noise field.

6.2.2.2 *Asymptotic Eigenvalue Density of the Isotropic Noise SCM*

The isotropic noise SCM $\widehat{\Sigma}$ is modeled as

$$\widehat{\Sigma} = \frac{1}{M}\Sigma\mathbf{X}\mathbf{X}^H, \tag{6.13}$$

where $\mathbf{X}$ is an $N \times M$ random matrix whose entries are zero-mean complex Gaussian random variables drawn from $\mathcal{CN}(0, 1)$ [Eq. (6.13) can be verified by taking an expectation]. The probability density of the eigenvalues of $\widehat{\Sigma}_\infty$ were derived [23] using Stieltjes transforms [36] for $N/M = \nu \leq 1$, i.e. the number of observations (snapshots) is larger than the dimensions of Σ (number of hydrophones).

When the ratio of spacing to wavelength $\beta < 1/2$ or β is a multiple of $1/2$ i.e., $\beta = q/2,\ q \in \mathbb{N}$, the SCM eigenvalue density is given by

$$\mathrm{p}_{\widehat{\Sigma}_\infty}(\lambda) = \begin{cases} \xi_1 \frac{\sqrt{(\lambda_+ - \lambda)(\lambda - \lambda_-)}}{2\pi\nu\lambda} & \lambda_- < \lambda < \lambda_+ \\ \xi_2 \delta(\lambda) & \text{otherwise,} \end{cases} \tag{6.14}$$

where $\lambda_\pm = (\sqrt{\Lambda_1} \pm \sqrt{\nu})^2$ are the upper and lower limits of the "spreading" of the eigenvalues of the SCM around the true eigenvalue which is Λ_1. The density when β

is a multiple of $1/2$ is known as the Marčenko–Pastur density [42]. Regardless of the value of ν, $\widehat{\Sigma}$ is rank deficient for all $\beta < 1/2$, as $\xi_2 \neq 0$.

The eigenvalue density of the SCM and the extent of spreading of the eigenvalues for all other values of β can be found in Ref. [23].

6.3 Sequential Hypothesis Testing of the SCM Eigenvalues

Eigenvalue based sequential testing using RMT was introduced in Ref. [17] for signals in white noise and extended to colored noise in Ref. [22]. If the noise only CM is known exactly (or if a noise only SCM can be estimated) and if it can be inverted, one could perform a "noise whitening" transformation [22] on the data to transform the underlying noise CM to the identity matrix, following which the eigenvalues can be tested using known results from RMT. However, this is not possible here, as the isotropic noise CM and SCM are inherently rank deficient for $\beta < 1/2$ and hence not invertible. In this section, we outline an approach based on Ref. [17] to distinguish those eigenvalues of the data SCM $\widehat{\mathbf{R}}$ that are due to loud sources, from those due to diffuse noise.

Since the number of large eigenvalues K, that are dominated by loud sources is not known *a priori*, at each f (or equivalently β), we test sequentially the eigenvalues of $\widehat{\mathbf{R}}$, $\{\hat{\lambda}_1, \ldots, \hat{\lambda}_N\}$ at each step k (starting with $k = 1$) against the following two hypotheses $\mathcal{H}_0$ (null) and $\mathcal{H}_1$ (alternate) at a significance level α per test,

$$\begin{aligned} \mathcal{H}_0 &: \text{The } k\text{th eigenvalue is due to diffuse noise} \\ \mathcal{H}_1 &: \text{The } k\text{th eigenvalue is dominated by loud sources} \end{aligned} \tag{6.15}$$

until $\mathcal{H}_0$ no longer can be rejected. The termination criterion follows from the fact that the eigenvalues dominated by loud sources are larger than the eigenvalues due to noise only (by definition) and hence once $\mathcal{H}_0$ cannot be rejected for some k, the subsequent $N - k$ eigenvalues must also be due to diffuse noise.

6.3.1 Behavior of the Largest Eigenvalue of the SCM

6.3.1.1 *In a Noise Only Scenario*

If there were no loud sources ($K = 0$) in the environment and the diffuse noise field is isotropic, the eigenvalues of $\widehat{\mathbf{R}} = \widehat{\boldsymbol{\Sigma}}$ in the asymptotic limit are distributed as $\mathrm{P}_{\widehat{\boldsymbol{\Sigma}}_\infty}(\lambda)$. Since no eigenvalues exist [43] outside the support of the density $\mathrm{p}_{\widehat{\boldsymbol{\Sigma}}_\infty}(\lambda)$, the largest eigenvalue of $\widehat{\mathbf{R}}_N$, $\hat{\lambda}_1$, converges almost surely to the upper bound of the density [22], λ_+ as $N \to \infty$.

Typically, the distribution of the largest eigenvalue of complex Wishart matrices is described using the Tracy–Widom (TW) distribution [44]. For the case when $\mathbf{R} = \mathbf{I}$, the identity matrix, it was shown that the statistic [17, 45]

$$M^{2/3} \frac{\hat{\lambda}_1 - m_{TW}}{s_{TW}} \sim TW, \tag{6.16}$$

for some scaling constant s_{TW} and centering constant m_{TW}, both dependent on N and M. While these constants can be computed explicitly in this case, it is not straightforward for arbitrary SCMs [46].

When $\widehat{\mathbf{R}} = \widehat{\boldsymbol{\Sigma}}$ (diffuse noise only), the equivalent of Eq. (6.16) can be written as

$$\hat{\lambda}_1 \sim \mathrm{P}_{1|\widehat{\boldsymbol{\Sigma}}}, \tag{6.17}$$

where $\mathrm{P}_{1|\widehat{\boldsymbol{\Sigma}}}(\lambda)$ is the ECD of the largest eigenvalue of $\widehat{\boldsymbol{\Sigma}}$. $\mathrm{P}_{1|\widehat{\boldsymbol{\Sigma}}}(\lambda)$ can be computed in a straightforward fashion from Monte Carlo simulations, as is done in Sec. 6.3.2.2.

6.3.1.2 *In the Presence of Loud Sources*

The presence of loud sources in the environment which are captured in the $K > 0$ large eigenvalues of $\mathbf{S}$ [Sec. 6.2.1, under Eq. (6.6)] manifests in the K largest eigenvalues of the SCM $\widehat{\mathbf{R}}$ that are now larger than what they would have been had there been no sources. The eigenvalues of $\widehat{\mathbf{R}}$ that are dominated by loud sources are distinguishable from the eigenvalues due to noise when they cross a certain threshold [22, 47] (which depends on the separation between the eigenvalues of $\mathbf{S}$ and $\boldsymbol{\Sigma}$, their distributions, and ν). The exact value of the threshold is not relevant to this discussion

and here, we assume that all the $K \ll \text{rank}(\Sigma)$ largest eigenvalues are distinguishable (although this is not always the case—see the last paragraph of Sec. 6.4.4.1).

The distribution of the K largest eigenvalues in this case is Gaussian [46,47] (i.e., different from the noise only case) and they can be identified in a statistical hypothesis test [Eq. 6.15)]. For example, when $K = 1$, the null hypothesis that $\hat{\lambda}_1$ belongs to $\mathrm{P}_{1|\widehat{\Sigma}}$ [Eq. (6.15) with $k = 1$] will be rejected with a high probability, indicating that $\hat{\lambda}_1$ is an eigenvalue dominated by loud sources.

6.3.2 Inferring the Noise Eigenvalues

More generally, at step k in the hypothesis test (see Sec. 6.3.2.2 for further details), $\hat{\lambda}_k$ (which can be considered to be the largest eigenvalue of an $N - k + 1$ dimensional SCM) is checked to see if it belongs to $\mathrm{P}_{1|\widehat{\Sigma}_{N-k+1}}$, i.e., the ECD of the largest eigenvalue for an $N - k + 1$ dimensional noise SCM.

The choice of $\mathrm{P}_{1|\widehat{\Sigma}_{N-k+1}}$ to test $\hat{\lambda}_k$ instead of the more intuitive $\mathrm{P}_{k|\widehat{\Sigma}}$, i.e. the ECD of the kth eigenvalue of $\widehat{\Sigma}$, can be understood from the interlacing properties of eigenvalues (see Appendix 6.A). As a result of Eq. (6.29), with $r = k - 1,\ i = 1,\ \mathbf{A} = \widehat{\Sigma}$, and $\mathbf{A}' = \widehat{\Sigma}_{N-k+1}$, the corresponding ECD $\mathrm{P}_{k|\widehat{\Sigma}}$ is stochastically smaller than $\mathrm{P}_{1|\widehat{\Sigma}_{N-k+1}}$. Hence, testing $\hat{\lambda}_k$ using $\mathrm{P}_{1|\widehat{\Sigma}_{N-k+1}}$ provides a conservative p-value for $\mathcal{H}_0$ (i.e., the actual probability of observing an outlier when $\mathcal{H}_0$ has not been rejected, is smaller) [17].

6.3.2.1 *Test Statistic*

To test $\hat{\lambda}_k$, the test statistic

$$\tau(k) = \frac{\hat{\lambda}_k}{\widehat{\sigma}_k^2}, \tag{6.18}$$

is used, following Ref. [17], with

$$\widehat{\sigma}_k^2 = \frac{\bar{\Lambda}}{N' - k + 1} \sum_{i=k}^{N'} \hat{\lambda}_i. \tag{6.19}$$

Here N' is the number of eigenvalues that are theoretically non zero and $\bar{\Lambda}$ is the theoretical mean of the N' eigenvalues [see Eq. (6.20)]. Hence, $\widehat{\sigma}^2(k)$ is merely a normalization factor such that the eigenvalues from data can be tested using distributions obtained from simulations.

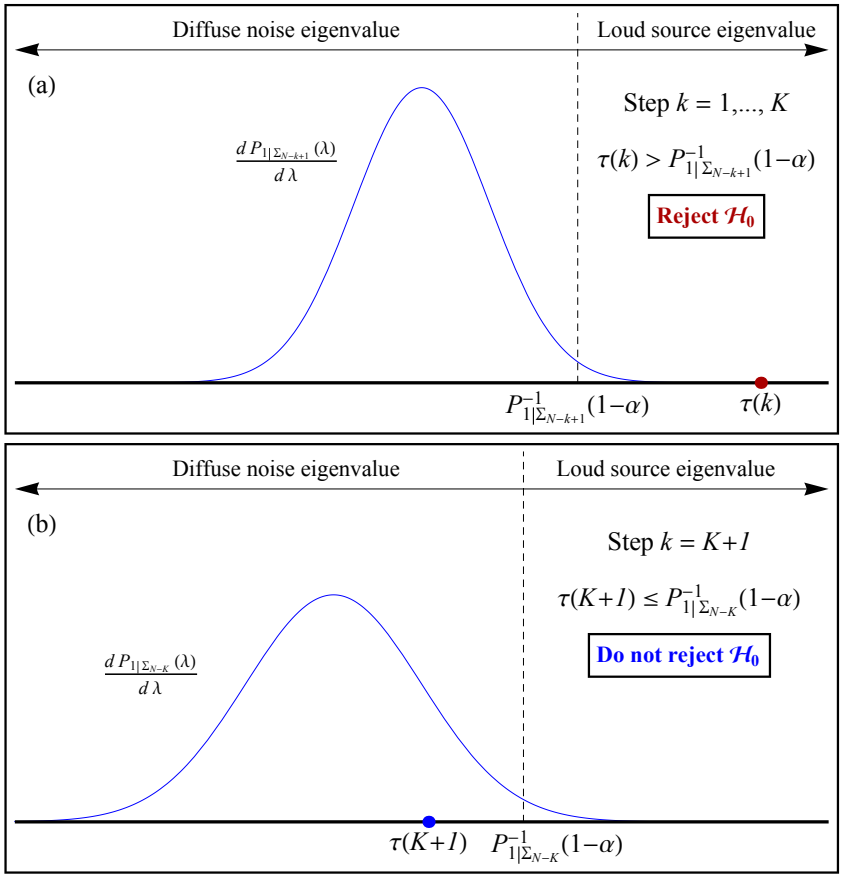

Figure 6.1: Schematic illustrating the hypothesis test to identify eigenvalues dominated by loud sources. (a) In the presence of K loud sources, the test statistic $\tau(k)$ ($k = \{1, \ldots, K\}$ does not belong to the $\mathrm{P}_{1|\widehat{\Sigma}_{N-k}}$ distribution when tested at significance α and $\mathcal{H}_0$ is rejected. (b) The largest eigenvalue from diffuse noise falls inside $\mathrm{P}_{1|\widehat{\Sigma}_{N-K+1}}$ and hence $\mathcal{H}_0$ cannot be rejected.

When $\beta < 1/2$, the noise SCM $\widehat{\Sigma}$ is rank deficient because $\xi_2 > 0$ and the corresponding eigenvalues asymptotically are zero (Sec. 6.2.2.2). However in practice, they are not *exactly* zero, likely due to sensor noise (self-noise due to system electronics that is independent from element to element). It was observed empirically that including these eigenvalues in the sequential testing often resulted in $\mathcal{H}_0$ being rejected with a greater likelihood i.e., eigenvalues that were due to the diffuse noise field were identified incorrectly as being dominated by loud sources (also see Sec. 6.4.2.1).

To avoid this problem, an *ad hoc* correction is made by considering only the largest $N' = \lfloor \xi_1 N \rfloor$ eigenvalues (i.e., only those eigenvalues that theoretically are non-zero) for the sequential testing and accordingly, $\bar{\Lambda} = \Lambda_1$. For all other values of β, $\bar{\Lambda} = 1$ and $N' = N$. In short,

$$\bar{\Lambda}, N' = \begin{cases} \Lambda_1, \lfloor \xi_1 N \rfloor & \beta < 1/2 \\ 1, N & \text{otherwise.} \end{cases} \tag{6.20}$$

6.3.2.2 *Hypothesis Testing*

Starting with $k = 1$, the null hypothesis $\mathcal{H}_0$ in Eq. (6.15) is tested at a significance level α and is rejected if

$$\tau(k) > \mathrm{P}^{-1}_{1|\widehat{\Sigma}_{N-k+1}}(1-\alpha). \tag{6.21}$$

The test in Eq. (6.21) is repeated, incrementing k each time, until $\mathcal{H}_0$ cannot be rejected. From the resulting value of k, the number of eigenvalues K' that *effectively* are identified as the outliers that are dominated by loud sources, is given by $K' = k-1$. The remaining $N - K'$ eigenvalues then are considered to be due to diffuse noise. Note that the α here is per test, and not the overall α for the procedure, which is expected to be higher (this typically is controlled using methods such as the Bonferroni correction).

A pre-computed lookup table is generated for $\mathrm{P}^{-1}_{1|\widehat{\Sigma}_{N-k+1}}(1-\alpha)$ from 1000 Monte Carlo trials for the given array configuration, for all k and β, assuming a sound speed of $c = 1500$ m/s. One could also perform a simple binary test using the asymptotic upper bounds for the eigenvalue density and get equally good results [26].

Table 6.1: Sequential hypothesis testing algorithm

Input

1. Frequency f, significance level α, eigenvalues of $\widehat{\mathbf{R}}(f)$, $\{\hat{\lambda}_1(f), \ldots, \hat{\lambda}_N(f)\}$
2. Pre-computed lookup table of $\mathrm{P}^{-1}_{1|\widehat{\Sigma}_{N-k+1}}(1-\alpha)$ for $k = \{1, \ldots, N\}$ at f

Testing

1. Assume sound speed, $c = 1500$ m/s
2. $\beta \leftarrow d/c$ where d is inter-element spacing
3. Define $\tau(k)$, $\widehat{\sigma}^2_k$ and N' as per Eqs. (6.18)–(6.20).
4. $k \leftarrow 1$
5. While $\tau(k) > \mathrm{P}^{-1}_{1|\widehat{\Sigma}_{N-k+1}}(1-\alpha)$

   Reject $\mathcal{H}_0$ [see Eq. (6.15)]

   If $k \neq N'$

   $k \leftarrow k+1$

   Else Break
6. Return $K' \leftarrow k-1$

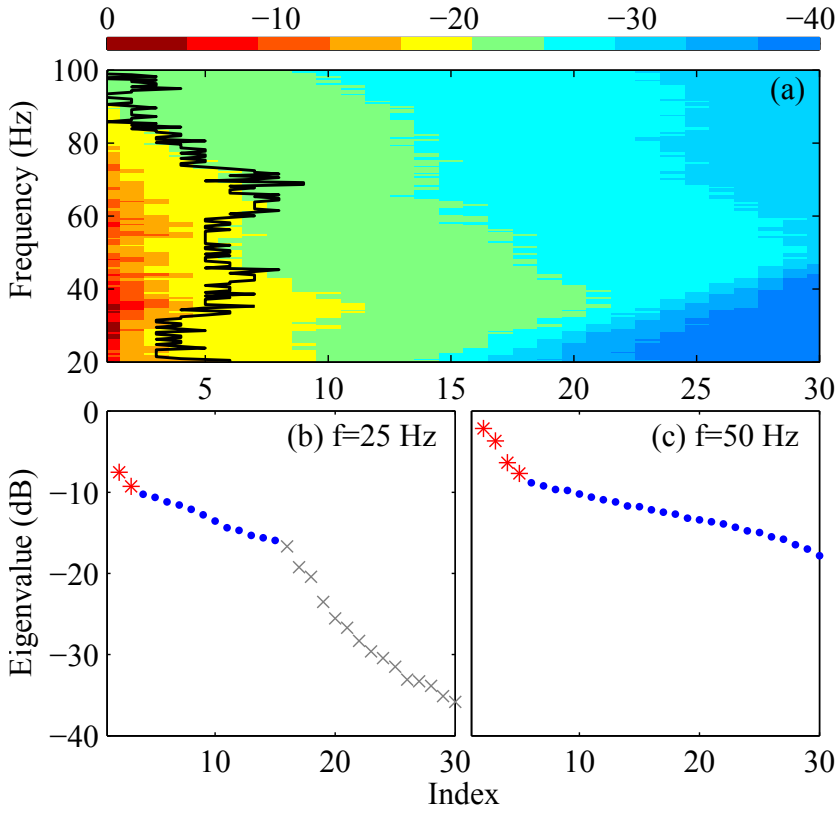

Figure 6.1: (a) Eigenvalues of the data SCM $\widehat{\mathbf{R}}$ (dB) for 20–100 Hz at a single time slice. The solid line shows the threshold separating the directional noise (to the left) from the diffuse noise. (b, c) Individual eigenvalues at 25 and 50 Hz due to loud sources ($*$), diffuse noise ($\bullet$) and eigenvalues not considered [$\times$, only in (b)]. In each panel, the eigenvalues are normalized by the maximum in that panel.

6.4 Experimental Results

6.4.1 Data Processing

Ocean acoustic data from a bottom mounted horizontal line array (Shark array deployed by the Woods Hole Oceanographic Institution), at a water depth of 79 m with an inter-element spacing of $d = 15$ m are used here. The data were recorded from 13:00:00 to 15:14:24 UTC on September 1, 2006 (one day before tropical storm Ernesto) as part of the Office of Naval Research sponsored Shallow Water 2006 (SW06) experiment conducted off the coast of New Jersey [48]. Only the data from the first

$N = 30$ hydrophones of the 32 element array are used because the 31st hydrophone had inconsistencies in the data [9]. This dataset was chosen specifically from a time interval where several ships were present in the environment, in order to highlight the advantage of this approach where conventional methods do not yield good results.

The data from each hydrophone were bandpass filtered to 20–100 Hz and downsampled to a sampling frequency of $f_s = 244.1406$ Hz (500,000 samples every 2048 s). The filtered data were stored in blocks of 128 s each. Each block was further divided into $M = 125$ segments of 1.024 s each and Fourier transformed with a 512 point FFT. At each frequency f, the transformed data are written as a column vector $\mathbf{x} = [x_1, \cdots, x_N]^T$ and the SCM for the block, $\widehat{\mathbf{R}}$ is formed as in Eq. (6.1), with $N = 30$ and $M = 125$.

6.4.2 Eigen-structure of the Ocean Noise Field

6.4.2.1 *Eigenvalues of the SCM* $\widehat{\mathrm{R}}$

The sequential hypothesis testing algorithm (Table. 6.1) with significance level $\alpha = 0.05$ is used to separate $\widehat{\mathbf{R}}$ into $\widehat{\mathbf{R}}_s$ and $\widehat{\mathbf{R}}_n$ for each data block at each frequency bin. Visualizing the eigenvalues at a single time slice (128 s from 14:31:44) reveals a rich variation across frequency [Fig. 6.1(a)] and the algorithm picks out the outlier eigenvalues quite well at all frequencies (solid line).

The dark triangle to the lower right is the region with zero eigenvalues (theoretically) and corresponds to invisible space [49]. This also is observed in Fig. 6.1(b) where the eigenvalues drop past the 16th eigenvalue, which closely corresponds to $\lfloor \xi_1 N \rfloor$ as predicted by theory (6.12).

If the correction in Eq. (6.20) were not applied, it was observed in nearly all the cases that for $\beta < 1/2$ $\mathcal{H}_0$ was rejected up until about the $\lfloor \xi_1 N \rfloor + 1$th eigenvalue. In other words, only those eigenvalues that theoretically are zero [$\times$ in Fig. 6.2(b)] were being retained, which was incorrect. Hence, not considering these small eigenvalues results in a better separation of the loud source dominated eigenvalues from the diffuse noise eigenvalues, as can be verified visually in Fig. 6.2.

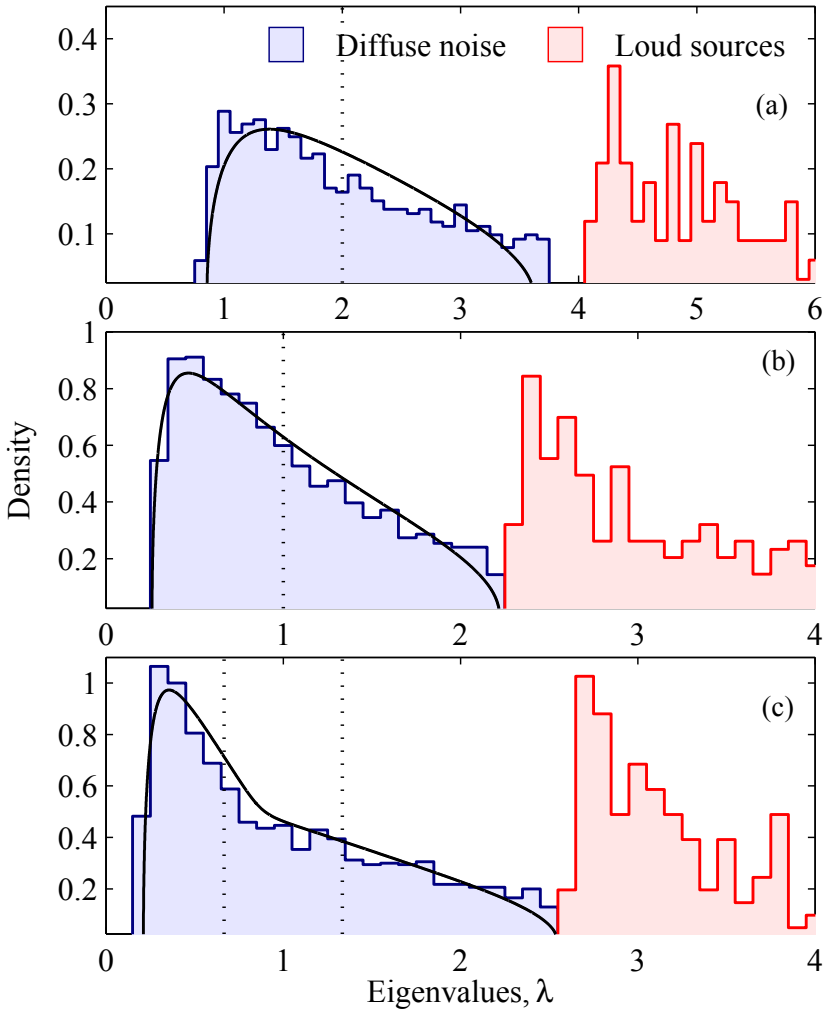

Figure 6.2: Empirical eigenvalue density (histogram) of the eigenvalues of $\widehat{\mathbf{R}}_n$ (under the solid lines) and $\widehat{\mathbf{R}}_s$ (to the right) obtained from ocean acoustic data for f = (a) 25 Hz, (b) 50 Hz and (c) 75 Hz. The solid lines correspond to the asymptotic eigenvalue density. In (a), only the contribution from the largest $\lfloor \xi_1 N \rfloor$ eigenvalues are shown. The dotted line(s) show the location(s) of the non-zero eigenvalue(s) of the isotropic noise CM. The densities for the eigenvalues of $\widehat{\mathbf{R}}_s$ extend beyond the extent of the panels and is truncated for clarity.

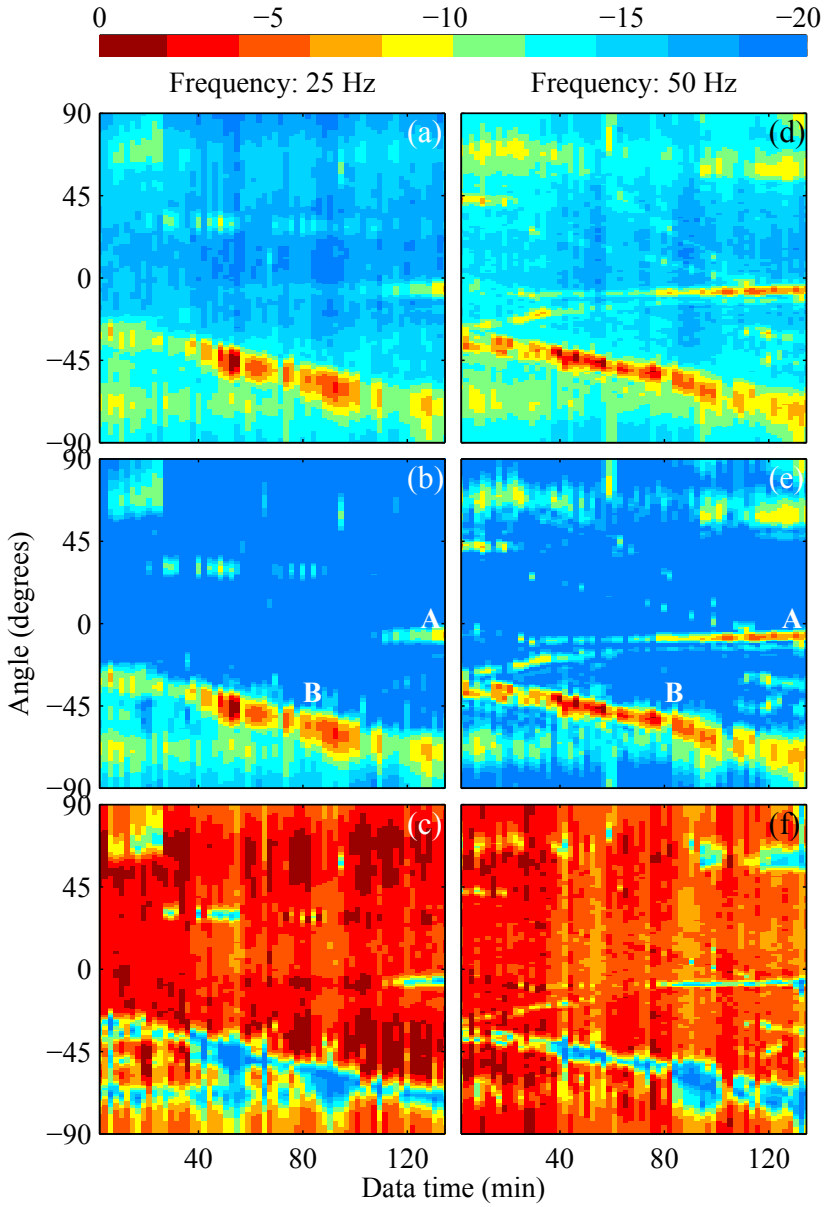

Figure 6.3: Conventional beamformer output (dB) at 25 and 50 Hz using (a, d) $\widehat{\mathbf{R}}$, (b, e) $\widehat{\mathbf{R}}_s$ and (c, f) $\widehat{\mathbf{R}}_n$. The beamformer output in each panel is normalized by the maximum in that figure. "A" and "B" mark the tracks from loud sources.

6.4.2.2 *Empirical Eigenvalue Density*

The histogram of the non-zero eigenvalues of $\widehat{\mathbf{R}}_n$ from each 128 s realization for the entire 136.5 min duration (normalized to unit mean at each time slice) is shown in Fig. 6.2 (a–c) for $f = 25, 50$ and 75 Hz respectively. Note that since the ensemble of eigenvalues forming the histogram was obtained by discarding a different number of loud source dominated eigenvalues at each realization [on average, 3–6 eigenvalues are identified as loud source related for the frequencies shown here; see Fig. 6.1(a)], the densities shown are not the true densities and Fig. 6.2 should only be interpreted qualitatively.

Nevertheless, the eigenvalue densities from the data resemble the asymptotic densities (thick solid line) in Section 6.2.2 remarkably well. The histograms of the directional source eigenvalues (from $\widehat{\mathbf{R}}_s$ with the same normalization as for $\widehat{\mathbf{R}}_n$) are displayed to the right of the corresponding noise eigenvalue densities.

6.4.3 Beamformer Output

Conventional beamforming with Hamming spatial shading was performed for each block for $\widehat{\mathbf{R}}_s$ and $\widehat{\mathbf{R}}_n$ at 25 and 50 Hz as:

$$B_{(\cdot)}(\theta) = \mathbf{w}^H(\theta)\widehat{\mathbf{R}}_{(\cdot)}\mathbf{w}(\theta), \tag{6.22}$$

where $\mathbf{w}(\theta)$ is the shaded steering vector, with the phase of the nth element given by $w_n(\theta) = \exp\left[\imath 2\pi f n d/c \, \sin(\theta)\right], \; n = \{0, 1, \ldots, N-1\}$.

The dataset shows the presence of a few loud sources in the environment, with two prominent ones being an almost stationary source at about -6° and a source moving from -30° to -80° over the entire duration ["A" and "B" respectively in Fig. 6.3(b, e)]. The biasing effect of these loud sources in the medium is demonstrated in Sec. 6.4.4.1.

Beamforming on the diffuse noise component demonstrates the isotropic nature of the noise field with nulls only at directions corresponding to the large eigenvalues that were removed [Fig. 6.3(c, f)]. The nature of the noise field when the large eigenvalues are re-weighted instead of being removed is discussed in Section. 6.4.5.

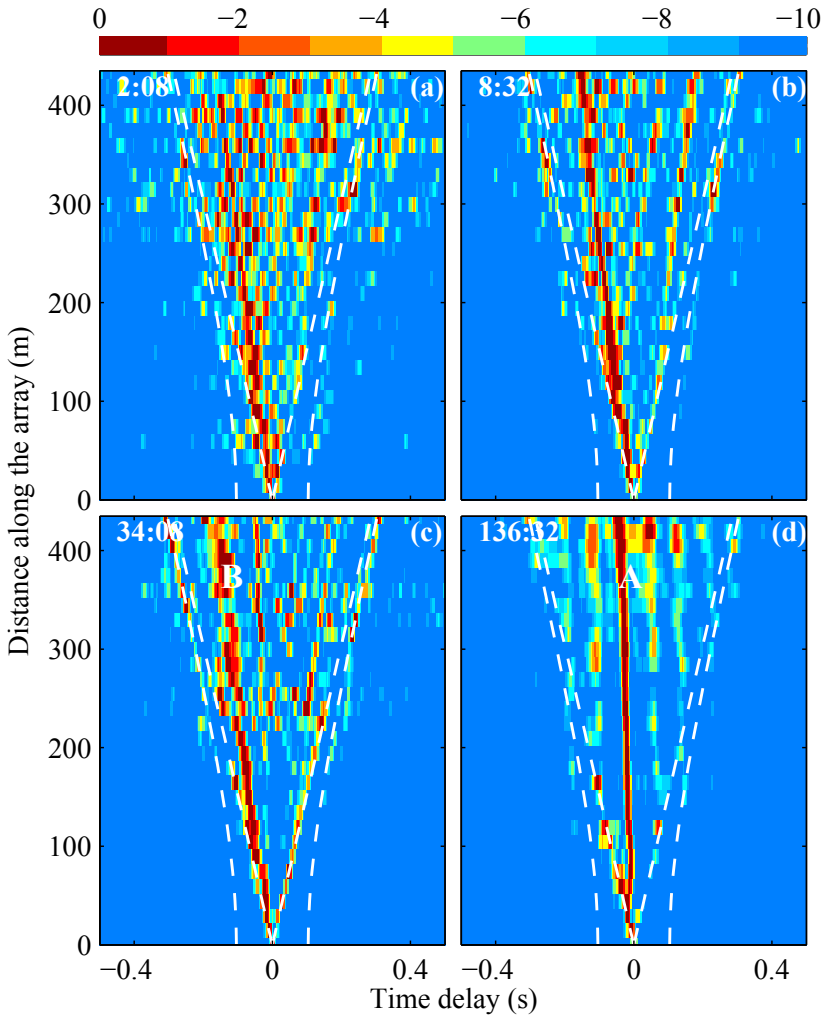

Figure 6.4: Noise cross-correlations (dB) using $\widehat{\mathbf{R}}$. The dashed lines indicate the predicted travel times for the direct (inner) and the surface reflected (outer) paths. Panels (a–d) show the evolution of the cross-correlation function with successive quadrupling of averaging time, starting with 2 minutes in (a). Travel times marked "A" in (d) and "B" in (c) correspond to the respective loud sources indicated in Fig. 6.3(b, e).

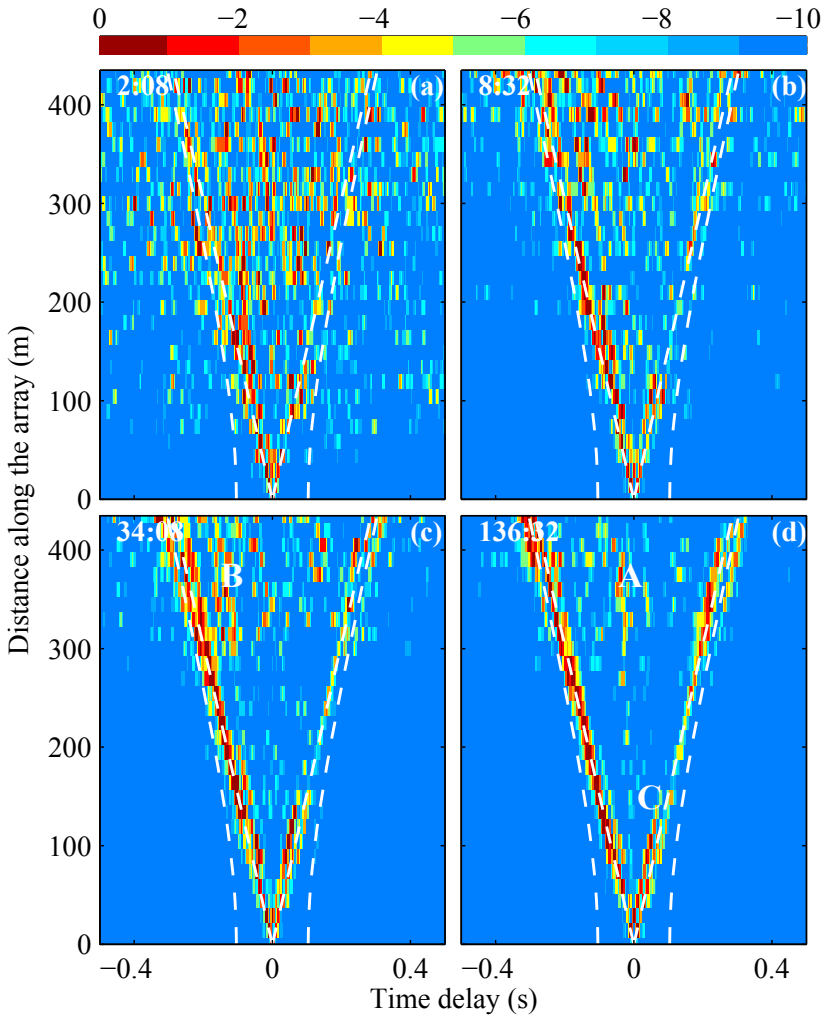

Figure 6.5: Noise cross-correlations (dB) using $\widehat{\mathbf{R}}_n$ The dashed lines indicate the predicted travel times for the direct (inner) and the surface reflected (outer) paths. Panels (a–d) show the evolution of the cross-correlation function with successive quadrupling of averaging time, starting with 2 minutes in (a). Travel time marked "A" in (d) and "B" in (c) correspond to the respective loud sources indicated in Fig. 6.3(b, e). "C" marks an arrival (which has a symmetric component) that could possibly correspond to a propagation path through the bottom layer.

6.4.4 Cross-correlations of Diffuse Noise

6.4.4.1 *Convergence of the Cross-correlations*

The SCM from each subsequent data block is added to the previous, and the resulting averaged cross-correlation is obtained using Eq. (6.2) as

$$\langle \widehat{C}_{1j}(t) \rangle_T = \mathcal{F}^{-1} \left[\langle \widehat{\mathbf{R}}_{1j}(f) \rangle_T \right], \tag{6.23}$$

where T denotes the total averaging time. The array configuration (number of hydrophones N and inter-element spacing d), bandwidth and the choice of observation time M influence the duration of a single block (here 128 s).

Fig. 6.4(d) shows the noise cross-correlations obtained by averaging 64 consecutive instances of $\widehat{\mathbf{R}}$ (128 s each) or a total of 136.5 mins [evolution of the cross-correlation with successive quadrupling of averaging time in Fig. 6.4(a–d)]. The dashed lines indicate the predicted travel times for the direct and surface reflected paths, predicted assuming a straight line propagation path, using sound speed measurements in the vicinity of the site (CTD Knorr185–36). The travel times observed can be linked to the location of the directional sources in Fig. 6.3(b, e). As the direction of the moving source changes from -30° at the start to -80° at the end of the data window ["B" in Fig. 6.3(b, e)], the corresponding travel time also changes accordingly ["B" in Fig. 6.4(c)]. Slowly moving sources build up correlation peaks steadily and dominate the observed travel times ["A" in Fig. 6.4(d)]. These figures illustrate the effect of directional noise sources in the medium, which results in several spurious arrivals that are visible at correlation times less than the predicted times and reduce the reliability of the travel time estimates.

In contrast, the noise cross-correlations obtained using $\widehat{\mathbf{R}}_n$ instead of $\widehat{\mathbf{R}}$ (as before, averages of 64 consecutive instances) in Eq. (6.2) have a two-sided (symmetric) structure (Fig. 6.5). A two-sided cross-correlation is typical for a diffuse noise field, and the negative time delays correspond to a propagation direction opposite to that of the positive time delays. The observed travel times also correspond well to the predicted travel times (see Fig. 6.6). A faster arrival with a symmetric component is observed ["C" in Fig. 6.5(d)], which could possibly correspond to a propagation path through the sediment layer.

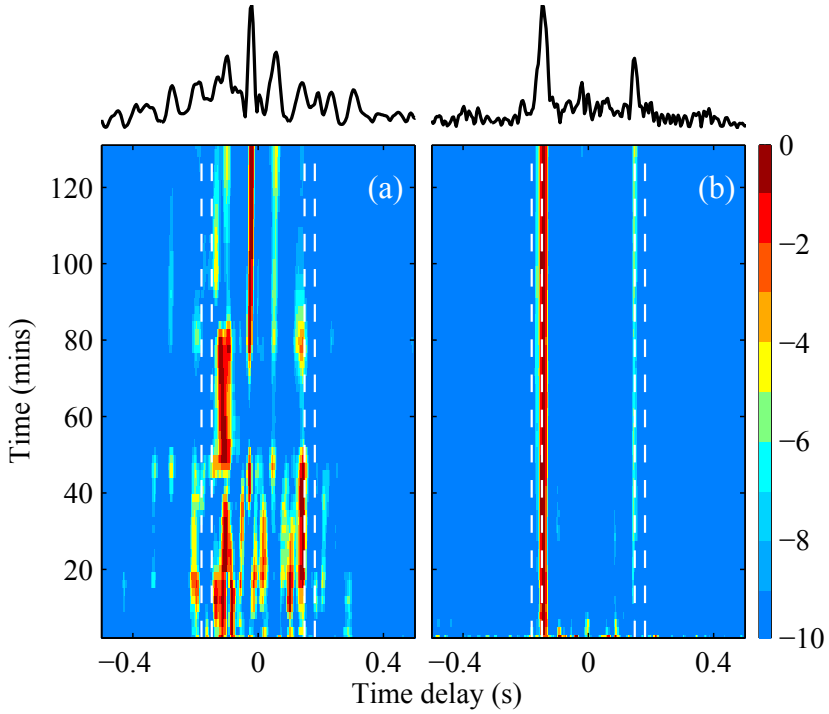

Figure 6.6: Averaged cross-correlations between sensors 1 and 16 (spaced 240 m apart) obtained using (a) $\widehat{\mathbf{R}}$ and (b) $\widehat{\mathbf{R}}_n$ with increasing averaging time. The maximum in each trace has been normalized to 1 for plotting purposes in order to highlight the peaks. The result after averaging or 136.5 min (solid) is shown above the respective plots. Dashed lines indicate the predicted travel times for the direct (inner) and the surface reflected (outer) paths.

One also sees a weak arrival close to zero lag ["A" in Fig. 6.5(d)], which is due to residual components from the loud source at −6° ["A" in Fig. 6.3(b, e)] that the eigenvalue processing failed to remove. A likely reason is that this source was not loud enough to be detected by the algorithm (see discussion in Sec. 6.3.1.2). Yet, it built up a correlation peak because it was moving slowly.

6.4.4.2 *Signal-to-Noise Ratio*

The signal-to-noise ratio (SNR) of the cross-correlation build up also is studied as a function of averaging time for the data considered here. Here, SNR is defined as the ratio of the maximum of the cross-correlation in a 0.025 s window around the predicted travel time to the standard deviation of the fluctuations at large correlation

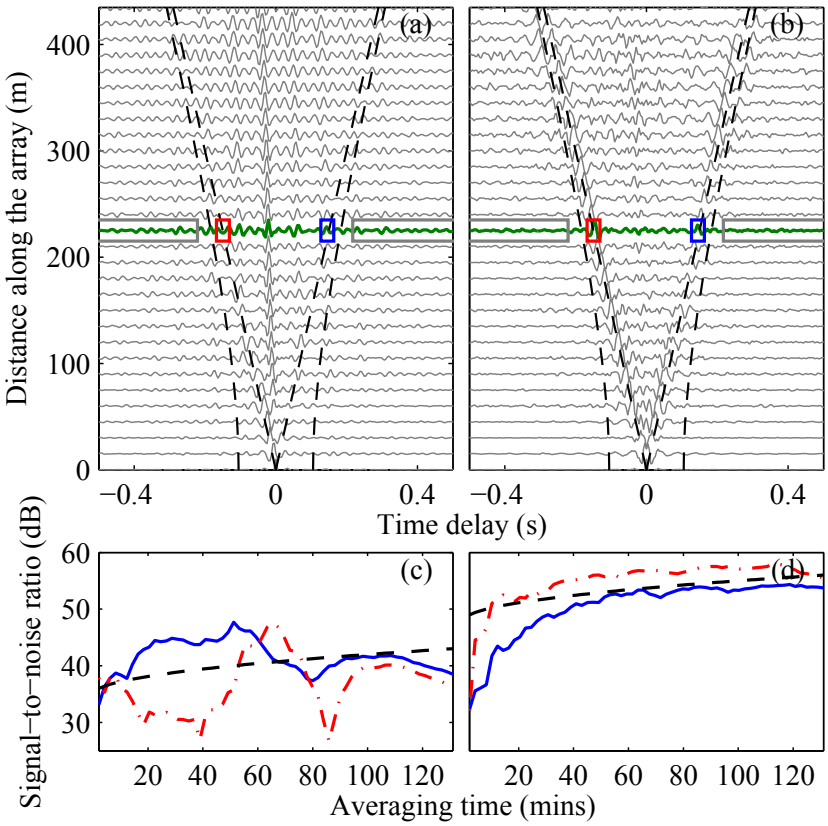

Figure 6.7: (a, b) Noise cross correlations using the data SCM $\widehat{\mathbf{R}}$ and the diffuse noise SCM $\widehat{\mathbf{R}}_n$ respectively after 136.5 min of averaging. (c, d) Signal-to-noise ratio (SNR) for the positive (solid) and negative (dot-dashed) time delay of the noise cross-correlation function between sensors 1 and 16 [highlighted in (a) and (b)] with increasing averaging time using $\widehat{\mathbf{R}}$ and $\widehat{\mathbf{R}}_n$ respectively. The dashed line shows the square root of time curve, which is the SNR build up predicted by theory.

times [see trace at 240 m in Fig. 6.7(a,b), same trace also shown on top of Fig. 6.6.] [7]. This definition helps track the build up of the SNR at the predicted time, and avoids skewing of the result due to the peak in the data being shifted due to directional sources.

When there are loud sources in the environment that are in motion, the location of the correlation peaks vary with the direction of the source and hence the SNR does not build up steadily and fluctuates with time [see Fig. 6.7(c)]. On the other hand, when the loud sources are removed, the peaks build up along the travel times corresponding to propagation along the end-fire direction and the SNR shows a steady increase, proceeding as the square-root of averaging time T as predicted by theory (dashed line) [7].

6.4.5 Cross-correlations From Re-weighted Eigenvalues

Although the cross-correlations obtained using $\widehat{\mathbf{R}}_n$, provide reliable results (Sec. 6.4.4), it does not utilize the entire diffuse noise field because the separated diffuse noise component has spatial voids in directions corresponding to the large eigenvalues that were removed [Fig. 6.3(c, f)]. This is because the eigenvalues and eigenvectors of $\widehat{\mathbf{R}}_s$ also include contributions from the diffuse noise field (Sec. 6.2.1), which cannot be separated. Since the biasing effect in cross-correlations is caused by the non-zero eigenvalues of $\widehat{\mathbf{R}}_s$, it also is possible to mitigate their effect by re-weighting the large eigenvalues instead of removing them entirely.

Consider a re-synthesized SCM $\widetilde{\mathbf{R}}$ obtained as

$$\widetilde{\mathbf{R}} = \sum_{k=1}^{K'} \tilde{\lambda}_k \hat{\mathbf{v}}_k \hat{\mathbf{v}}_k^H + \widehat{\mathbf{R}}_n \tag{6.24}$$

where $\tilde{\lambda}_k$ are the re-weighted eigenvalues ($\tilde{\lambda} = 0$ in Sec. 6.4.4). There are several ways in which the weights can be assigned, and two straightforward weightings are considered here:

1. $\tilde{\lambda}_i$ = Mean of the noise eigenvalues, i.e.

$$\tilde{\lambda}_i = \frac{1}{N' - K'} \sum_{k=K'+1}^{N'} \hat{\lambda}_k, \; i = 1, \ldots, K' \tag{6.25}$$

2. $\tilde{\lambda}_i$ = Largest noise eigenvalue, i.e.

$$\tilde{\lambda}_i = \hat{\lambda}_{K'+1}, \; i = 1, \ldots, K' \tag{6.26}$$

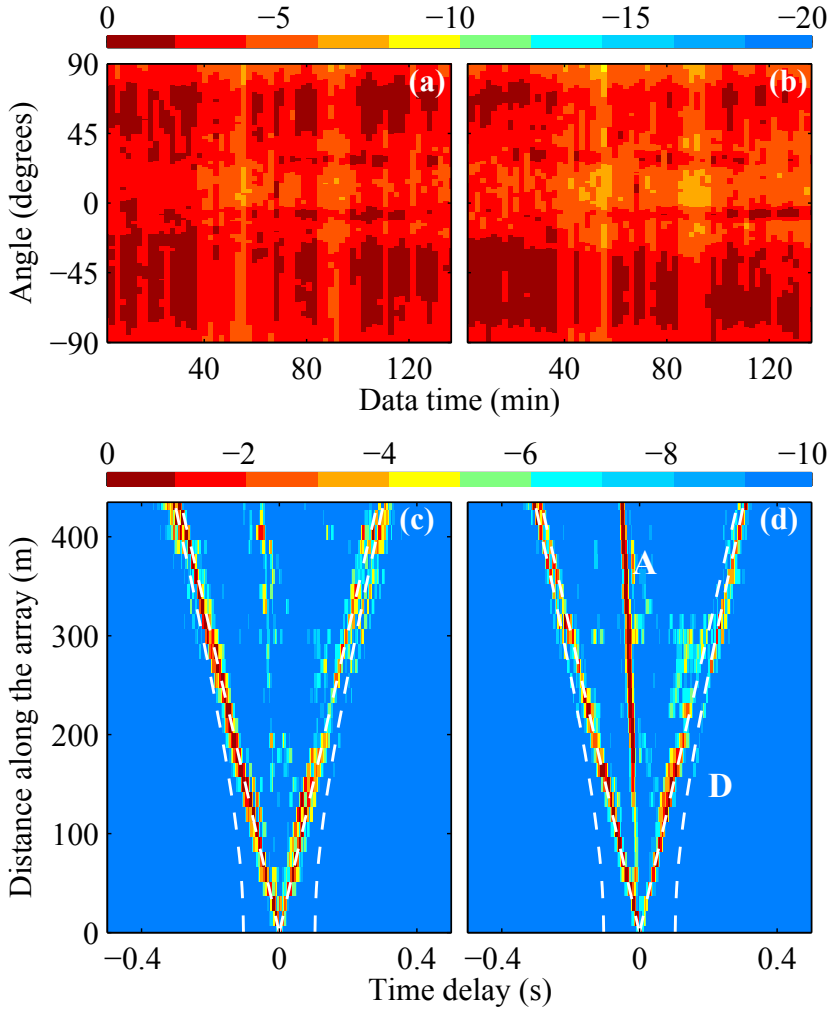

Figure 6.8: Beamformer outputs (dB) at 25 Hz (a, b) and cross-correlations (dB) from 136.5 min of averaging (c, d) obtained by re-weighting the large eigenvalues using Eq. (6.25) in (a, c) and Eq. (6.26) in (b, d).

In both cases, the resulting noise field [Fig. 6.8(a, b)] does not exhibit the spatial voids observed when using only $\widehat{\mathbf{R}}_n$ [Fig. 6.3(c, f)]. The 136.5 min averaged cross-correlations using $\widetilde{\mathbf{R}}$ with the weights in Eq. (6.25) [Fig. 6.8(c)], are very similar to that obtained using $\widehat{\mathbf{R}}_n$ [Fig. 6.5(d)]. However, using the weights in Eq. (6.26) gives a cross-correlation structure that has both, the arrivals at the predicted travel times, and a spurious arrival ["A" in Fig. 6.8(d)] corresponding to the slowly moving source at $-6°$ ["A" in Fig. 6.3(b, e)]. This spurious arrival can easily be discarded by time-gating. The surface-reflected arrival also is visible from 150 m in range onwards ["D" in Fig. 6.8(d)], whereas it is only visible from 300 m onwards in Fig. 6.5(d) and Fig. 6.8(c). As seen from the two examples, changing the weights can lead to different results and each approach can be advantageous in different scenarios.

6.5 Impact of Alternative Ocean Diffuse Noise Models

Here we compare qualitatively the impact of using three alternative ocean noise models for the hypothesis testing in addition to the 3D isotropic model (ISO) already considered in this article — surface noise in a fluid half-space (Cron–Sherman model [50]) with omnidirectional sources (CS0) and cosine directional sources (CS1), and surface noise in a waveguide with a sediment layer (Kuperman–Ingenito model [51], KI). The KI is a more complicated noise model that incorporates waveguide physics and is representative of ocean noise in shallow water environments. It is used here primarily to show the similarities between the simpler models (which don't require any knowledge of the environment) and a model based on the local environment.

The CMs for the noise models using the array configuration in Sec. 6.4.1 and a medium sound speed of 1500 m/s are obtained using Eq. 6.10 for Σ^{ISO} and

$$\Sigma_{ij}^{\mathrm{CS0}} = \mathrm{J}_0(2\pi\beta|i-j|) \tag{6.27}$$

$$\Sigma_{ij}^{\mathrm{CS1}} = \frac{2\,\mathrm{J}_1(2\pi\beta|i-j|)}{2\pi\beta|i-j|} \tag{6.28}$$

where J_0 and J_1 are the Bessel functions of the first kind and zeroth and first orders respectively. The KI model, Σ^{KI}, is generated by a wavenumber integration approach using OASES [52] assuming a 79 m deep stratified waveguide (using a sound speed

profile from CTD measurements at the site) and a seabed with soundspeed [9] 1650 m/s and density 1.69 g/cm^3.

Fig. 6.1 shows the eigenvalues of the CM for the different noise models for $\beta = 0.25$ (a) and $\beta = 0.5$ (b). The eigenvalues of Σ^{ISO} are very close to that of Σ^{KI} (assumed to be true), and those of Σ^{CS1}, while similar in general structure to the KI, show more deviation. The CS0 model least resembles the KI and shows a large deviation. The small differences between the eigen-structure of Σ^{KI} and those of Σ^{ISO} and Σ^{CS1} are further reduced in their respective SCMs as observed by the similarity in the eigenvalue density (obtained from 1000 Monte Carlo trials) of $\widehat{\Sigma}^{\mathrm{KI}}$ to that of $\widehat{\Sigma}^{\mathrm{ISO}}$ [Fig. 6.1(c,d)]. This is related to the general spreading of eigenvalues observed in SCMs. The similarity in the density holds when the observations $M \sim N$ and decrease as $M \to \infty$. In contrast, the eigenvalue density of $\widehat{\Sigma}^{\mathrm{CS0}}$ remains different from the rest in shape and the upper edge of the density.

Intuitively, one would expect a density with a larger value of $\mathrm{P}^{-1}_{1|\widehat{\Sigma}^{(\cdot)}_{N-k+1}}(1-\alpha)$ such as that for $\widehat{\Sigma}^{\mathrm{CS0}}$ to reject $\mathcal{H}_0$ less often, i.e. rejecting it only in cases where the loud source eigenvalue is very large (compared to the other models). This is indeed the case, as seen from Fig. 6.2, where the thresholds separating the loud source subspace and the diffuse noise subspace are shown for the different models. As expected from the similarities in the density, the thresholds obtained using ISO (solid) are nearly identical to that from KI (dot-dashed), differing by at most one or two. CS1 (dotted) also follows the general pattern for the KI and 3D thresholds. CS0 (dashed), which showed the most deviation, identifies only the very largest of the loud source eigenvalues.

The effect of a shifted threshold arising from a poorly chosen model is seen clearly in the beamformer output in Fig. 6.3 using the CS0 model (results for KI and CS1 are very similar to those of ISO shown earlier in Sec. 6.4 and hence are not shown here). Several ship tracks are identifiable in the "diffuse noise" subspace that is obtained using the CS0 model ["A" and "B" in Fig. 6.3(b,d); compare with Fig. 6.3(c,f)] and the resulting noise cross-correlations are still contaminated by spurious arrivals from loud sources [Fig. 6.4(a)].

In summary, simple analytical noise models which do not require any additional knowledge of the environment, can be used as a reasonable approximation to

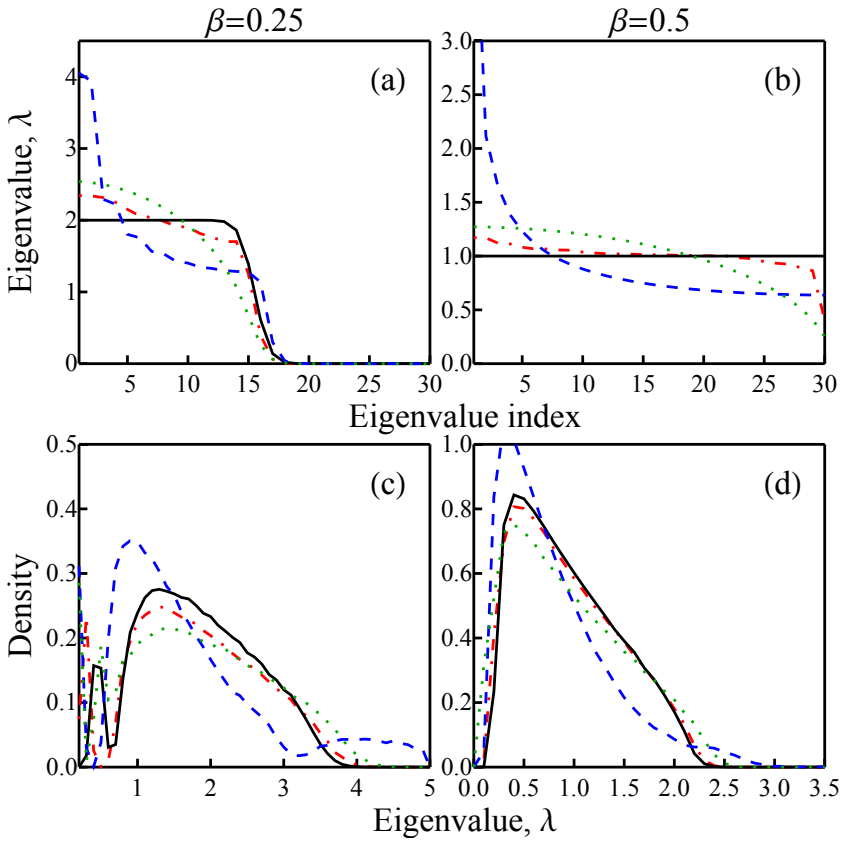

Figure 6.1: Eigenvalues of the CM for the 3D isotropic noise model (ISO, solid), the Cron–Sherman model for surface noise in a fluid half-space with omnidirectional sources (CS0, dashed) and sources with cosine directionality (CS1, dotted), and the Kuperman–Ingenito model for surface noise in a waveguide with a sediment layer (KI using measured environment parameters, dot-dashed) with $N = 30$ hydrophones and $\beta = 0.25$ (a) and $\beta = 0.5$ (b). (c,d) Empirical eigenvalue density of the SCMs ($\nu = 30/125$) corresponding to the CMs in (a,b) obtained from 1000 Monte Carlo trials.

more sophisticated models that incorporate waveguide physics and environmental information for the purposes of eigenvalue based statistical inference.

6.6 Conclusions

In this paper, we have demonstrated an eigenvalue based approach to separate ocean noise into directional and diffuse components. By approximating the diffuse noise recorded on a hydrophone array to be isotropic in nature, the eigenvalues of the data sample covariance (SCM) are analyzed. Insights from random matrix theory are

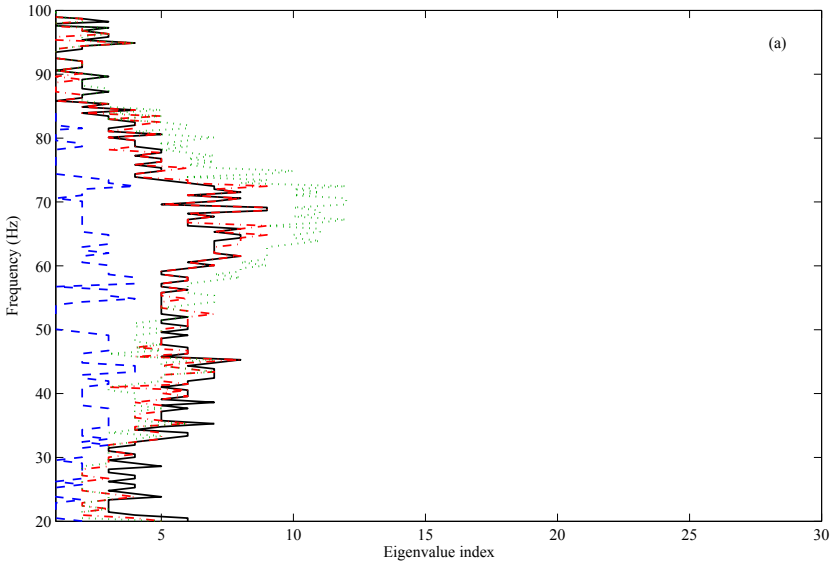

Figure 6.2: Threshold separating the directional noise (to the left) from the diffuse noise is shown at a single time slice for the 3D isotropic noise model (ISO, solid), the Cron–Sherman model for surface noise in a fluid half-space due to omnidirectional sources (CS0, dashed) and cosine directional sources (CS1, dotted), and the Kuperman–Ingenito model for surface noise in a waveguide with a sediment layer (KI, dot-dashed).

then used to explain the nature of the noise eigenvalues and a sequential hypothesis testing is performed to identify, and isolate or attenuate the loud, directional sources.

The resulting cross-correlations were shown to converge quickly and remain stable with increasing averaging time. The structure of the resulting cross-correlations are two-sided (positive and negative time delays), which reduces the ambiguity in the estimates of the travel time. The signal-to-noise ratio (SNR) of the cross-correlations was also shown to increase as the square root of time, which is consistent with theoretical predictions.

Finally, the impact of the chosen noise model on the identification of loud sources and cross-correlations were analyzed and it was shown that simple analytical noise models provide similar results as more sophisticated noise models that mimic the environment.

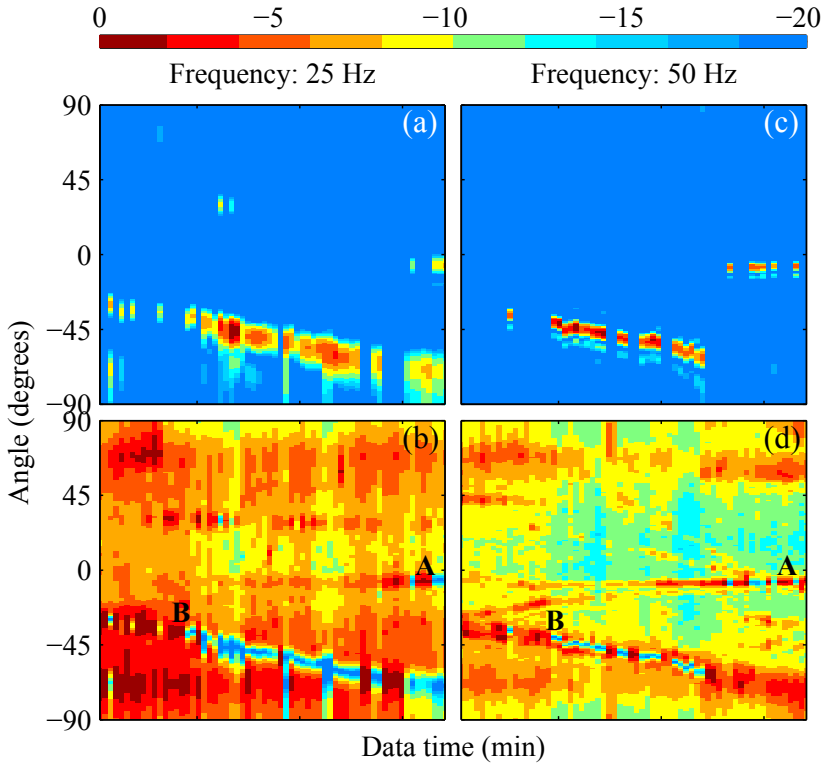

Figure 6.3: Conventional beamformer output (dB) at 25 and 50 Hz using (a,c) $\widehat{\mathbf{R}}_s$ and (b,d) $\widehat{\mathbf{R}}_n$ obtained by using the Cron–Sherman model for surface noise in a fluid half-space due to omnidirectional sources (CS0) for the hypothesis testing. The beamformer output in each panel is normalized by the maximum in that panel.

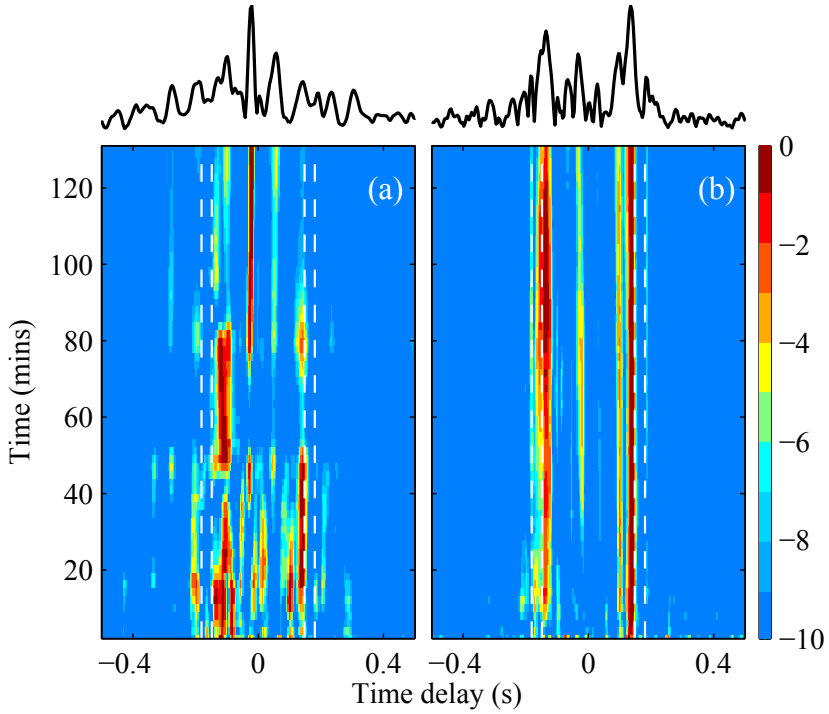

Figure 6.4: Averaged cross-correlations between sensors 1 and 16 (spaced 240 m apart) obtained using (a) $\widehat{\mathbf{R}}$ [same as Fig. 6.6 (a)] and (b) $\widehat{\mathbf{R}}_n$ with the hypothesis test performed using the Cron–Sherman model for surface noise in a fluid half-space due to omnidirectional sources (CS0).

6.7 Acknowledgments

This work was supported by the Office of Naval Research, Grant Nos. N00014-11-1-0320 and N00014-11-1-0321.

Chapter 6, in full, is a reprint of the material as it appears in R. Menon, P. Gerstoft and W. S. Hodgkiss, "Cross-correlations of diffuse noise in an ocean environment using eigenvalue based statistical inference", J. Acoust. Soc. Am. **132** (5), 3213-3224 (2012). The dissertation author was the primary researcher and author of this paper.

6.A Interlacing of Eigenvalues

Let $\mathbf{A}$ be any $N \times N$ Hermitian matrix, with eigenvalues $a_1 \geq a_2 \geq \cdots \geq a_N$ and $\mathbf{A}'$ be the $N-r \times N-r$ Hermitian matrix obtained by removing r rows and the corresponding r columns, with eigenvalues $a'_1 \geq a'_2 \geq \cdots \geq a'_{N-r}$. Then, the eigenvalues of $\mathbf{A}$ and $\mathbf{A}'$ interlace as,

$$a_i \geq a'_i \geq a_{i+r} \tag{6.29}$$

for $i \in \{1, \ldots, N-r\}$ Proof of Eq. (6.29) can be found in Ref. [53] (Theorem 4.3.15).

Bibliography

[1] O. I. Lobkis and R. L. Weaver, "On the emergence of the Green's function in the correlations of a diffuse field," *J. Acoust. Soc. Am.*, vol. 110, pp. 3011–3017, December 2001.

[2] R. L. Weaver and O. I. Lobkis, "Ultrasonics without a source: Thermal fluctuation correlations at MHz frequencies," *Phys. Rev. Lett.*, vol. 87, p. 134301, 2001.

[3] R. Snieder, "Extracting the Green's function from the correlation of coda waves: A derivation based on stationary phase," *Phy. Rev. E.*, vol. 69, p. 046610, 2004.

[4] K. Wapenaar, "Retrieving the elastodynamic Green's function of an arbitrary inhomogeneous medium by cross-correlation," *Phys. Rev. Lett.*, vol. 93, p. 254301, 2004.

[5] O. A. Godin, "Recovering the Acoustic Green's Function from Ambient Noise Cross Correlation in an Inhomogeneous Moving Medium," *Phys. Rev. Lett.*, vol. 97, p. 054301, Aug 2006.

[6] P. Roux, W. A. Kuperman, and the NPAL group, "Extracting coherent wave fronts from acoustic ambient noise in the ocean," *J. Acoust. Soc. Am.*, vol. 116, pp. 1995–2003, 2004.

[7] K. G. Sabra, P. Roux, and W. A. Kuperman, "Emergence rate of the time-domain Green's function from the ambient noise cross-correlation," *J. Acoust. Soc. Am.*, vol. 118, pp. 3524–3531, 2005.

[8] M. Siderius, C. H. Harrison, and M. B. Porter, "A passive fathometer technique for imaging seabed layering using ambient noise," *J. Acoust. Soc. Am.*, vol. 120, pp. 1315–1323, 2006.

[9] L. A. Brooks and P. Gerstoft, "Green's function approximation from cross-correlations of 20–100 Hz noise during a tropical storm," *J. Acoust. Soc. Am.*, vol. 125, pp. 723–734, Jan 2009.

[10] J. Traer, P. Gerstoft, and W. S. Hodgkiss, "Ocean bottom profiling with ambient noise: A model for the passive fathometer," *J. Acoust. Soc. Am.*, vol. 129, no. 4, pp. 1825–1836, 2011.

[11] N. M. Shapiro, M. Campillo, L. Stehly, and M. H. Ritzwoller, "High-resolution surface-wave tomography from ambient seismic noise," *Science*, vol. 307, pp. 1615–1618, 2005.

[12] P. Gerstoft, K. G. Sabra, P. Roux, W. A. Kuperman, and M. C. Fehler, "Green's functions extraction and surface-wave tomography from microseisms in southern California," *Geophysics*, vol. 71, pp. SI23–SI31, 2006.

[13] P. Gouédard, L. Stehly, F. Brenguier, M. Campillo, Y. C. de Verdière, E. Larose, L. Margerin, P. Roux, F. J. Sánchez-Sesma, N. M. Shapiro, and R. L. Weaver, "Cross-correlation of random fields: mathematical approach and applications," *Geophysical Prospecting*, vol. 56, pp. 375–393, 2008.

[14] S. C. Walker and M. J. Buckingham, "Spatial coherence and cross-correlation of three-dimensional ambient noise fields in the ocean," *J. Acoust. Soc. Am.*, vol. 131, no. 2, pp. 1079–1086, 2012.

[15] V. C. Tsai, "On establishing the accuracy of noise tomography travel-time measurements in a realistic medium," *Geophys. J. Int.*, vol. 178, pp. 1555–1564, 2009.

[16] M. L. Mehta, *Random Matrices.* Academic Press, 3rd ed., 2004. Chapter 1.

[17] I. M. Johnstone, "On the distribution of the largest eigenvalue in principal components analysis," *Ann. Statist.*, vol. 29, no. 2, pp. 295–327, 2001.

[18] N. E. Karoui, "Spectrum estimation for large dimensional covariance matrices using random matrix theory," *Ann. Statist.*, vol. 36, no. 36, pp. 2757–2790, 2008.

[19] X. Mestre and M. A. Lagunas, "Finite sample size effect on minimum variance beamformers: Optimum diagonal loading factor for large arrays," *IEEE Trans. Signal Proc.*, vol. 54, no. 1, pp. 69–82, 2006.

[20] X. Mestre, "On the asymptotic behaviour of the sample estimates of eigenvalues and eigenvectors of covariance matrices," *IEEE Trans. Signal Proc.*, vol. 56, no. 11, pp. 5353–5368, 2008.

[21] R. R. Nadakuditi and A. Edelman, "Sample eigenvalue based detection of high-dimensional signals in white noise using relatively few samples," *IEEE Trans. Signal Proc.*, vol. 56, no. 7, pp. 2625–2638, 2008.

[22] R. R. Nadakuditi and J. W. Silverstein, "Fundamental limit of sample generalized eigenvalue based detection of signals in noise using relatively few signal-bearing and noise-only samples," *IEEE J. Sel. Top. Signal Proc.*, vol. 4, no. 3, pp. 468–480, 2010.

[23] R. Menon, P. Gerstoft, and W. S. Hodgkiss, "Asymptotic eigenvalue density of noise covariance matrices," *IEEE Trans. Signal Proc.*, vol. 60, no. 7, pp. 3415–3424, 2012.

[24] M. Pajovic, J. Preisig, and A. Baggeroer, "Analytical characterization of the mpdr-based power estimators in snapshot scarce regime," *IEEE Stat. Signal Proc. Workshop (Ann Arbor, Michigan,)*, pp. 812–815, 2012.

[25] J. R. Buck and K. Wage, "A random matrix theory model for the dominant mode rejection beamformer notch depth," *IEEE Stat. Signal Proc. Workshop (Ann Arbor, Michigan)*, pp. 824–827, 2012.

[26] R. Menon, P. Gerstoft, and W. S. Hodgkiss, "Passive acousting monitoring using random matrix theory," *IEEE Stat. Signal Proc. Workshop (Ann Arbor, Michigan,)*, pp. 808–811, 2012.

[27] P. Gerstoft, R. Menon, W. S. Hodgkiss, and C. F. Mecklenbräuker, "Eigenvalues of the sample covariance matrix for a towed array," *J. Acoust. Soc. Am.*, vol. 132, no. 4, pp. 2388–2396, 2012.

[28] K. Wage, J. Buck, M. Dzieciuch, and P. Worcester, "Experimental validation of a random matrix theory model for dominant mode rejection beamformer notch depth," *IEEE Stat. Signal Proc. Workshop (Ann Arbor, Michigan)*, pp. 820–823, 2012.

[29] S. R. Tuladhar, J. R. Buck, and K. E. Wage, "Approximate eigenvalue distribution of a cylindrically isotropic noise sample covariance matrix," *IEEE Stat. Signal Proc. Workshop (Ann Arbor, Michigan)*, pp. 828–831, 2012.

[30] R. R. Müller, "A random matrix model of communication via antenna arrays," *IEEE Trans. Info. Theory*, vol. 48, no. 9, pp. 2495–2506, 2002.

[31] A. M. Tulino and S. Verdú, "Random matrix theory and wireless communications," *Foundations and Trends in Communications and Information Theory*, vol. 1, no. 1, pp. 1–182, 2004.

[32] R. L. Weaver, "Spectral statistics in elastodynamics," *J. Acoust. Soc. Am.*, vol. 85, pp. 1005–1013, 1989.

[33] A. Aubry and A. Derode, "Random matrix theory applied to acoustic backscattering and imaging in complex media," *Phys. Rev. Lett.*, vol. 102, p. 084301, 2009.

[34] A. Aubry and A. Derode, "Detection and imaging in a random medium: A matrix method to overcome multiple scattering and aberration," *J. Appl. Phys.*, vol. 106, p. 044903, 2009.

[35] S. E. Skipetrov and A. Goetschy, "Eigenvalue distributions of large Euclidean random matrices for waves in random media," *J. Phys. A: Math. Theor.*, vol. 44, p. 065102, 2011.

[36] J. W. Silverstein, "Strong convergence of the empirical distribution of eigenvalues of large dimensional random matrices," *J. Multivar. Anal.*, vol. 54, pp. 175–192, 1995.

[37] A. B. Baggeroer and H. Cox, "Passive sonar limits upon nulling multiple moving ships with large aperture arrays," *Asilomar Conf. on Sign., Syst., and Comp.*, vol. 1, pp. 103–108, 1999.

[38] D. H. Johnson and D. E. Dudgeon, *Array processing: Concepts and techniques*. Prentice Hall, 1993. Chapter 7.3.

[39] C. H. Eckart, "The theory of noise in continuous media," *J. Acoust. Soc. Am.*, vol. 25, no. 2, pp. 195–199, 1953.

[40] H. Cox, "Spatial correlation in arbitrary noise fields with application to ambient sea noise," *J. Acoust. Soc. Am.*, vol. 54, no. 5, pp. 1289–1301, 1973.

[41] R. M. Gray, "Toeplitz and circulant matrices: A review," *Found. Trends. Comm. Inf. Theory*, vol. 2, no. 3, pp. 155–239, 2006.

[42] V. A. Marčenko and L. A. Pastur, "Distributions of eigenvalues of some sets of random matrices," *Math. Sb.*, vol. 72, pp. 507–536, 1967.

[43] Z. Bai and J. W. Silverstein, "No eigenvalues outside the support of the limiting spectral distribution of large dimensional sample covariance matrices," *Ann. Prob.*, vol. 26, no. 11, pp. 316–345, 1998.

[44] C. A. Tracy and H. Widom, "Level-spacing distributions and the Airy kernel," *Comm. Math. Phys.*, vol. 159, pp. 151–174, 1994.

[45] K. Johansson, "Shape fluctuations and random matrices," *Comm. Math. Phys.*, vol. 209, pp. 437–476, 2000.

[46] N. E. Karoui, "Tracy–Widom limit for the largest eigenvalue of a large class of complex sample covariance matrices," *Ann. Probab.*, vol. 35, no. 2, pp. 663–714, 2007.

[47] J. Baik, G. B. Arous, and S. Péché, "Phase transition of the largest eigenvalue for nonnull complex sample covariance matrices," *Ann. Prob.*, vol. 33, no. 5, pp. 1643–1697, 2005.

[48] D. J. Tang, J. Moum, J. Lynch, P. Abbot, R. Chapman, P. Dahl, T. Duda, G. Gawarkiewicz, S. Glenn, J. Goff, H. Graber, J. Kemp, A. Maffei, J. Nash, and A. Newhall, "ShallowWater 2006: a joint acoustic propagation/nonlinear internal wave physics experiment," *Oceanography*, vol. 20, no. 4, pp. 156–167, 2007.

[49] D. H. Johnson and D. E. Dudgeon, *Array processing: Concepts and techniques.* Prentice Hall, 1993. Chapter 3.

[50] B. F. Cron and C. H. Sherman, "Spatial-correlation functions for various noise models," *J. Acoust. Soc. Am.*, vol. 34, pp. 1732–1736, 1962.

[51] W. A. Kuperman and F. Ingenito, "Spatial correlation of surface generated noise in a stratified ocean," *J. Acoust. Soc. Am.*, vol. 67, pp. 1988–1996, 1980.

[52] H. Schmidt, *OASES Version 3.1 User Guide and Reference Manual.* MIT, Cambridge MA, USA, 2004.

[53] R. A. Horn and C. R. Johnson, *Matrix analysis.* Cambridge Univ. Press, 1985. Chapter 4.

7

CONCLUSIONS AND FUTURE WORK

This dissertation has focused on developing approaches to address the challenges faced in ambient noise processing as described in Section 1.1. The following conclusions are drawn from this work:

1. Analysis of seismic noise using the Southern California Seismic Network (SCSN) shows a clear presence of fundamental and first mode surface rayleigh waves and body waves in the microseism band (0.05–0.2 hz). The higher mode Rayleigh waves are persistent and seen year round primarily from the west and occasionally from other azimuths when accompanied by large storms. The underlying spatial coherence function (SCF) is modeled as a linear combination of the above waves with the ratios estimated from data. The interactions between the different wavenumbers in the SCF leads to beating and phase cancellation effects which could be interpreted as being due to attenuation or the focusing and defocusing effects of velocity anisotropy. This data driven model for the SCF describes the observed coherence better than a simple zeroth order Bessel function model which corresponds to only the fundamental mode.

2. Adopting a matrix based processing for uniform line arrays, the true spatial covariance matrix (CM) is modeled as a Toeplitz Hermitian matrix with the SCF being the generating function for the matrix entries. Asymptotically, the CM

has at most two distinct eigenvalues for all values of the inter-element spacing to wavelength ratio. For less than half-wavelength spacing, the CM is rank deficient and the zeros of the eigenvalue spectrum correspond to the invisible region where propagating waves do not exist.

3. Using concepts from random matrix theory (RMT), the asymptotic eigenvalue density is derived for the sample covariance matrix (SCM) which is formed from independent observations of the noise field. It is shown that for spacings of less than half a wavelength, the SCM is always singular no matter how many snapshots are used. This rank deficiency has implications in signal processing algorithms that require the inverse of the SCM. For spacings of more than half a wavelength apart, the SCM is full rank if sufficient snapshots are used but the eigenvalue density can split into two distinct densities. If not taken into consideration, this can be misinterpreted as being due to a discrete source rather than just the noise field. The asymptotic results are shown to hold good even for arrays with as low as 20 sensors.

4. The presence of attenuation decreases the value of the large eigenvalues when compared to the attenuation free case and also raises the smaller eigenvalues due to the broadening of the bandwidth of the spatial coherence function. The shape of the eigenvalue density of the finite SCM varies with attenuation and this potentially could be used to retrieve medium attenuation properties. An approximation to the asymptotic eigenvalue density can be obtained using the polynomial method for random matrices.

5. Using the insights from random matrix theory in Chapter 3, we explain the nature of the noise eigenvalues observed in data. For a towed array in deep water, the eigenvalues are shown to agree well with theory. A sequential hypothesis testing framework is used to identify and isolate or attenuate the loud, directional sources in shallow water acoustic data. The resulting cross-correlations were shown to converge quickly and remain stable with increasing averaging time. The structure of the resulting cross-correlations are two-sided (positive and negative time delays) which reduces the ambiguity in the estimates of the

travel time. The signal-to-noise ratio (SNR) of the cross-correlations was also shown to increase as the square root of time which is consistent with theoretical predictions.

The publications that resulted from the work described in this dissertation are among the earliest uses of random matrix theory in ocean acoustics and the first in ambient noise processing. There are several possible directions of research that can be taken:

1. The azimuthal averaging performed in estimating the spatial coherence reduces the bias but potentially could increase the variance in the estimate for that distance bin. While conventional wisdom indicates that a lower azimuthal bias (closer to isotropic) is preferable, it is hard to quantify by how much the variance changes. This also depends on the geometry of the array and the statistics of the coherence which is unknown. A detailed analysis of the tradeoff involved and incorporating the statistics of the coherence would improve the approach.

2. Analytical results for the eigenvalues also could be obtained for common array configurations where the symmetry of the array can be exploited. Such results will have applications not only in noise processing but also in other aspects of array processing such as beamforming in Section 6.4.3 (truncating the eigenvalues of the CSDM) and spatial filtering (truncating the eigenvalues of the steering matrix) [1]

3. The CSDMs considered in this dissertation were all obtained from azimuthally uniform noise fields, which is a reasonable assumption for a horizontal line array. This assumption does not hold for the vertical line array in shallow water since the noise field has a vertical directionality due to the effects of the bottom. Understanding the behavior of the eigenvalues with changing bottom parameters would be beneficial in passive fathometer processing. This potentially is a hard problem since the wave number integration technique to obtain the coherence due to surface noise in a stratified ocean [2] is not convenient for analytical manipulations as in Chapter 3. It would be interesting to see if simpler analytical

models for the vertical coherence [3] can provide a good approximation to the upperbounds for the eigenvalues due to vertical noise.

Bibliography

[1] O. Carriere, P. Gerstoft, and W. Hodgkiss, "Spatial filtering in ambient noise crosscorrelation," in *Proceedings of Meetings on Acoustics*, vol. 19, p. 070043, 2013.

[2] W. A. Kuperman and F. Ingenito, "Spatial correlation of surface generated noise in a stratified ocean," *J. Acoust. Soc. Am.*, vol. 67, pp. 1988–1996, 1980.

[3] M. J. Buckingham, "A theoretical model of ambient noise in a low-loss shallow water channel," *J. Acoust. Soc. Am.*, vol. 67, pp. 1186–1192, 1979.